AUTOMATED DETECTION OF CRACKED RAILWAY AXLE JOURNALS USING AN ULTRASONIC PHASED ARRAY TECHNIQUE

A Dissertation

by

JAE YONG BAIK

Submitted to the Office of Graduate and Professional Studies of
Texas A&M University
in partial fulfillment of the requirements for the degree of

DOCTOR OF PHILOSOPHY

Chair of Committee,	Stefan Hurlebaus
Committee Members,	Gary T. Fry
	Jose M. Roesset
	Gwo-Ping (Alex) Fang
Head of Department,	Robin Autenrieth

August 2014

Major Subject: Civil Engineering

ABSTRACT

Railway vehicle axles experience fatigue behavior. This has become a critical issue considering both the increased loads and speeds of railway vehicles. The failure of one axle has the potential to cause derailment of the entire train. Train derailment can cause danger to the public, threaten lives, and cost thousands of dollars in repair and rehabilitation. A critical area is the axle journal. Inspecting axle journals is difficult due to limited accessibility, as the journal and nearby areas are covered by the bearing, bearing cap, and wheel. The main challenge of this research is to overcome the limited accessibility using ultrasonic techniques.

Three main railway axle journal inspection concepts have been developed in this research: 1) automated detection system of a cracked axle journal using the ultrasonic phased array technique, 2) detection of a cracked axle journal using a chain scanner, and 3) cracked axle journal detection using surface waves. An ultrasonic phased array system has a much higher probability of detection (POD) and will provide a much more rapid inspection when compared to conventional ultrasonic transducers. Surface wave inspection proves that it can propagate along the complex geometry of the railway axle journal. Support vector machine (SVM) and the developed algorithm successfully distinguished between a cracked axle and an uncracked axle. Signal processing with a threshold classifier was developed to provide a faster computation time.

Three different air-coupled experiments are demonstrated: 1) the line-source air-coupled ultrasonic array sensors in through-transmission mode, 2) the point-source air-

coupled ultrasonic generation using Rayleigh waves, and 3) the laser array detector on a steel plate. A complete air-coupled ultrasonic system is achieved with the air-coupled 20-array ultrasonic line source and point source with microphone sensor as receiver. The best results can be obtained with an excitation frequency range of 50 to 100 kHz. The generated ultrasonic waves successfully penetrated the aluminum sheet, the low-density polyethylene (LDPE) plate, and the concrete mortar using the through-transmission technique. The one-side non-contact crack detection is demonstrated using a Rayleigh wave. It successfully distinguishes between cracked and uncracked regions using the time-of-flight technique. A complete air-coupled ultrasonic system is developed for various materials in this research.

DEDICATION

To my daughter, Bailey Baik

To my wife, Youri Choi

To my parents

ACKNOWLEDGEMENTS

I would like to thank my committee chair, Dr. Hurlebaus, and my committee members, Dr. Fry, Dr. Fang, and Dr. Roesset, for their guidance and support throughout the course of this research.

I appreciate to my friends and the department faculty and staff for making my time at Texas A&M University a great experience. I also want to extend my gratitude to the Association of American Railroads, which provided the necessary funding. I would like to thank Union Pacific for donating a cracked axle.

Finally, thanks to my mother and father for their encouragement, to my daughter, and to my wife for her patience and love.

TABLE OF CONTENTS

Page

LIST OF FIGURES

Page

LIST OF TABLES

Page

CHAPTER I

INTRODUCTION

1.1 Research Motivation

Railway vehicle axles experience increased fatigue behavior due to increasing loads and speeds. Traditionally, the design for gross rail service load has been 263,000 lb. (80-ton service), but it increased to 286,000 lb. (100-ton service) in 1995. Because axles are made of steel, they are designed for a service life of 40 to 50 years; however, axles can fail before they reach their designed lifespan due to fatigue. Failure of one axle has the potential to cause the derailment of an entire train, resulting in a high risk to public safety. Fortunately, railway axles do not fail instantly. Statistically, a railway axle will fail if the surface has more than 30% cracked area, approximately 2.5 to 3 in. (63.5 to 76.2 mm) in depth. The best way to prevent disaster is to inspect the railway cars continuously. Unfortunately, this is impossible due to inspection cost and the time involved.

Derailment can occur due to failures within the axles, wheels, and rails. Previous studies have discovered various inspection methods for rails, wheels, and axles in laboratory conditions. Many non-contact ultrasonic methods have been proposed for rail inspection, and successful results have been obtained (Coccia et al. 2010, Djayaputra 2010, and Lanza di Scalea et al. 2005)**.** Researchers employ crack detection using multiple ultrasonic transducers or ultrasonic phased array techniques for wheel inspection (Garcia-Ares et al. 2006, and Marty 2012). Several methods have been proposed to inspect railway axles; however, not many studies have proposed crack detection in the inaccessible axle

journal region. The shortcoming of previous research is that the train axles must be disassembled for accurate inspection, making the process quite costly and time consuming. In the most recent cases, every part has to be disassembled, and the axle is tested separately. A better method would be to disassemble only the journal box and to test the overall area of axles from their end faces (Garcia-Ares et al. 2006, Liaptsis, Cooper, Boyle, & Nicholson 2011, and Marty 2012). This proposed research focuses on the detection of axle journal cracks using advanced ultrasonic techniques that do not require costly disassembly.

Figure 1.1 shows the number of axle-related accidents broken down by failure location for the last 16 years. According to the Federal Railroad Administration (Federal Railroad Administration [FRA] 2012), 23.5% of axle-related accidents during this time period were due to cracks in the journal region. It has shown that axles fail more often at the axle body than other parts. It is important to prevent all possible accidents, and it is clear that there are more axle-related accidents in the past decade as opposed to the 1990s.

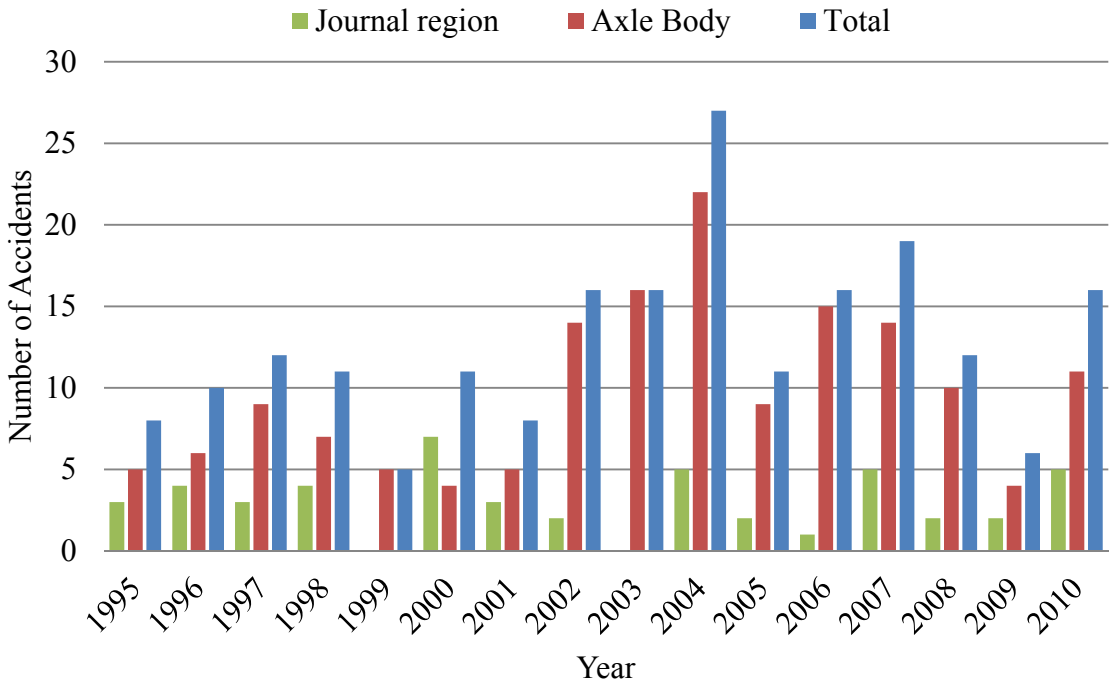

Figure 1.1. Statistic of axle-related accidents (FRA 2012)

1.2 Research Needs

Most current railway axle inspection technologies utilize the conventional ultrasonic technique or magnetic particle testing. Conventional ultrasonic provides a low POD and inconsistency due to the coupling medium. The ultrasonic phased array technique gives a high POD and allows for high-speed scanning from a single position. A significant contribution in detecting cracked railway axles using a contact ultrasonic phased array was provided by Hansen and Hintze (2005). Despite the limited access for inspection, they successfully detected cracks using an ultrasonic phased array technique that could be steered and focused at multiple angles. However, while they proved the experiment to be successful, consistent coupling of the probes will be a critical issue for

future use. In addition, axles had to be disassembled from the bogie cars, making the inspection both time-intensive and expensive. Establishing a method to inspect the railway axle on moving trains is one of the major needs in this field of study. A portable axle inspection system, which can easily go underneath railway cars, is also needed. An air-coupled ultrasonic system will eliminate the need for a coupling medium, allowing for the future development of a non-contact inspection method.

1.3 Research Objectives

The main objectives of this research project are to:

1- verify that an ultrasonic phased array system can be used to detect discontinuities on an axle journal area using computer simulation.

2- develop an automated inspection system using ultrasonic phased array in a laboratory environment.

3- use a chain scanner to detect flaws on the railway axle with an ultrasonic phased array in a laboratory environment.

4- investigate the difference in ultrasonic signal between the axle itself and the axle with a wheel and bearing.

5- utilize air-coupled ultrasonic to find the limitations and feasibility of non-contact ultrasonic testing.

6- develop a signal processing method and pattern recognition algorithm to minimize human involvement during the inspection procedure.

1.4 Research Approach

In terms of fracture mechanics, there are three concepts: safe-life, fail-safe, and damage tolerance (Zerbst, Madler, & Hintze 2005 and Zerbst, Vormwald, Andersch, Madler, & Pfuff 2005). This research uses the damage tolerance concept, which allows for some fatigue crack propagation based on imperfections in the population, applied stress, and material properties, as shown in Figure 1.2. Given any two parameters, the third must be controlled or provide assurance that the system in question is safe. It is important to know the probability of undetected imperfections. The growth rate of these undiscovered imperfections is critical in determining the inspection interval. The proposed research focuses on discovering small imperfections.

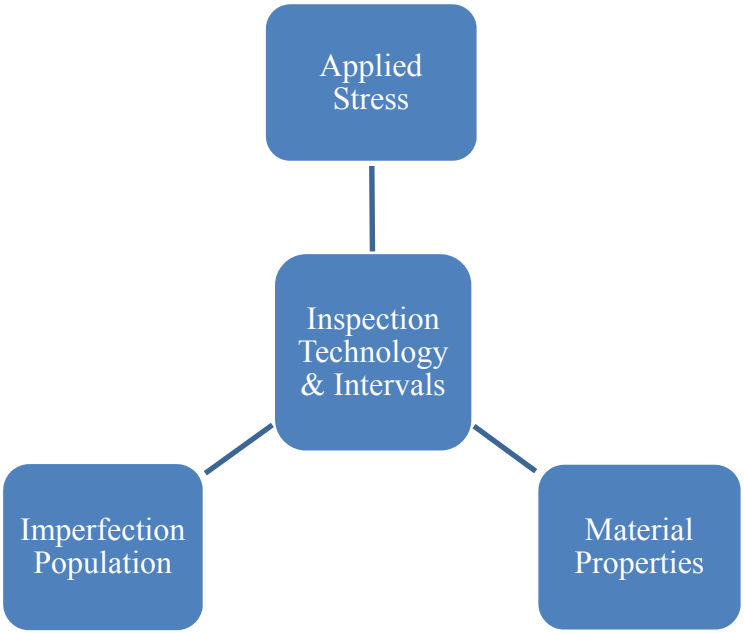

Figure 1.2. Damage tolerance concepts

Experimental examinations are heavily involved in this research project. Union Pacific Railroad donated an axle with several induced cracks to Texas A&M University. Based on Association of American Railroads (Association of American Railroads [AAR] 1984) and Australian Rail Track Corporation Ltd. (Australian Rail Track Corporation Ltd. [ARTC] 2005) engineering standards, an axle with defects needs to be replaced or repaired. Any axle that has a defect greater than 0.12 in. (3 mm) needs to be removed from service. Therefore, the ultrasonic device is calibrated to detect defects less than 0.12 in. (3 mm). To increase the inspection interval time, the size of detectable cracks needs to be smaller. The cracked axle is tested in laboratory conditions with the contact ultrasonic phased array technique. In using this method, it is important to keep the axle rotation and the coupling constant. A chain scanner is also applied to the axle as a different inspection system. The goal of these experiments is to inspect a train axle without requiring disassembly. The railway axle journal is also tested using a Rayleigh wave with conventional ultrasonic transducers. An automated detection algorithm is developed for the Rayleigh wave using a signal processing technique.

Additionally, an air-coupled ultrasonic technique is demonstrated on concrete, aluminum and LDPE plates. The goal of these experiments is to perform the inspection of axles in a non-contact manner in the near future. To make a complete non-contact system, the contact ultrasonic phased array system has to be replaced with air-coupled ultrasonic phased array transducers. Given the state of current technology, there are various air-coupled ultrasonic transducers, but they only work well with non-metallic materials or thin metal plates using a through-transmission technique because of the high impedance

mismatch between air and metal. The findings of this research will contribute to the field of railway axle inspection and ultrasonic non-destructive testing (NDT).

CHAPTER II

LITERATURE REVIEW

2.1 Introduction

Within current railway axle inspection technologies, ultrasonic phased array is the best method to identify defects on axles (Hansen & Hintze 2005, Liaptsis et al. 2011). The air-coupled ultrasonic approach is also investigated as an efficient railway inspection method. Finally, pattern recognition algorithms are examined to make an automated inspection system for this research.

The following sections summarize the previous research works. The area of previous research includes 1) advantages of ultrasonic phased array over conventional ultrasonic testing, 2) air-coupled ultrasonic system, 3) air-coupled ultrasonic phased array system, 4) railway axle inspection technique, and 5) pattern recognition algorithm.

2.2 Ultrasonic Phased Array

Ultrasonic phased array has been developed in the past decade. The technique is fairly new and is not part of the ultrasonic standards, such as International Organization for Standardization (ISO) or European Committee for Standardization (CEN). Moles, Dube, Labbe, and Ginzel (2005) and Frederick, Porter, and Zimmerman (2010) showed not only the advantages of the ultrasonic phased array technique over conventional ultrasound, but also showed that it worked well on complicated specimen geometries. Moles et al. (2005) performed weld inspection using ultrasonic phased array and explained

the advantages of ultrasonic phased array over radiography and conventional ultrasound. Frederick et al. (2010) provided an example of complex geometry inspection.

High-density polyethylene (HDPE) piping does not allow ultrasonic waves to penetrate well. The material has high attenuation compared to other materials. Current American Society of Mechanical Engineers (ASME) code requires visual inspections of the weld bead formation but does not require a volumetric examination of welds. The ultrasonic phased array technique can replace the ASME code requirements with more precise and convenient results. Frederick el al. (2010) proved that ultrasonic phased array can detect a 1/32-in. (0.8-mm)-diameter hole through the fusion line of a weld; thereby showing that ultrasonic phased array had great potential for NDT.

Ciorau (2004) compared defect sizing accuracy between conventional and phased array ultrasonic techniques. Many probes were used for both conventional and phased array ultrasound. Ciorau (2004) chose to use the frequency of conventional transducers ranging from 5 to 10 MHz and of ultrasonic phased array transducers ranging from, 4 to 12 MHz. Crack size accuracy was within 0.06 in. (1.5 mm) when using conventional ultrasonic with a tip-echo diffraction technique. Ultrasonic phased array gave more accurate results with an error of only 0.02 in. (0.5 mm). Not only does ultrasonic phased array provide more accurate defect sizing, but it is also faster and more convenient because it generates multiple A-scans simultaneously. Ciorau (2004) found that the ultrasonic phased array technique provided more accurate results when using both longitudinal waves and shear waves (P- and S-waves) than the conventional ultrasonic technique. In

addition, crack tips were easier to identify, and crack branches could be measured well with the focused beam.

2.3 Air-coupled Ultrasonic System

Contact ultrasonic techniques cause problems because a coupling medium must be applied consistently to obtain quality results, and the surfaces of specimens need to be prepared prior to inspection. The air-coupled ultrasonic technique for non-metals has been done by several researchers, including Stoessel (2004), Stoessel, Krohn, Pfleiderer, and Busse (2002), Zhu and Popovics (2005), Sukmana and Ihara (2005), Blum, Jarzynski, and Jacobs (2005), Kazys, Demcenko, Zukauskas, and Mazeika (2006), Solodov, Doring, and Busse (2009), and Hilbers et al. (2012). They discovered that air-coupled transducers work with aerospace composites, concrete, and fiber-reinforced plastics which are water- or oil-sensitive materials.

Zhu and Popovics (2005) detected concrete defects using surface wave with air-coupled sensors. The surface wave is more practical than the body waves because it usually has a larger amplitude than a body wave. A surface wave is generated by the impact of a hammer and is detected by an air-coupled sensor and accelerometer for comparison. The microphone had a frequency range from 0 to 20 kHz. They found that the signals must be reliable and consistent to use leaky surface wave detection. The leaky surface wave is the acoustic wave front from which an air-coupled ultrasonic sensor can receive a signal. Frequencies used for concrete varied from 5 to 25 kHz. Kazys et al. (2006)

used the Lamb wave A_0 mode for single-side access. For the composite and plastic materials, they used a frequency range of 200 to 500 kHz.

Sukmana and Ihara (2005) observed the roughness of nine sheets of sandpaper with different grit sizes using air-coupled ultrasonic transducers. A polished stainless-steel plate was used as a baseline. They performed two experiments with pitch-catch and pulse-echo modes. Broadband transducers were used with 500 kHz of central frequency. The distance between the transducers and the specimen was 35 mm. The pitch-catch mode tested five different incident angles, while the pulse-echo mode was performed only with a 0° incident angle. They concluded that the amplitude decreases as the roughness increases, and the incident angle is not a crucial factor for the amplitude. In addition, an increase of roughness causes the loss of higher-frequency waves.

Blum et al. (2005) successfully observed an LDPE plate using an air-coupled array transducer. A focused two-dimensional (2D) air-coupled ultrasonic array system was developed. The array system had 20 electrostatic transducers and an operating frequency ranging from 50 to 100 kHz, which is optimum for civil infrastructure. Their transducer array could generate sound pressure level (SPL) of up to 150 dB to overcome energy loss in air. A microphone was used to detect the generated signal in a through-transmission manner. The test specimen of the experiment was LDPE, with dimensions of 23.9 × 12.0 × 1.6 in. (608 × 305.5 × 41.4 mm). The bulk wave speeds of P-waves and S-waves was 82,480 and 27,840 in/s (2,095 and 707.1 m/s), respectively, and the distance between the specimen and the array system was 8.01 in. (205 mm).

Solodov et al. (2009) efficiently used a mode conversion to generate transversal bulk waves such as plate acoustic wave (PAW), Lamb wave, surface acoustic wave (SAW), and Rayleigh wave. Their methods significantly reduced energy losses in air. Three different applications were performed using PAW and SAW: focused slanted transmission mode (FSTM), focused slanted reflection mode (FSRM), and air-coupled differential time-of-flight (DTOF). They tested several different materials with air-coupled piezo-composite transducers. For excitation, high-voltage (200-V) square wave bursts were used with a frequency range of 200 to 450 kHz. From FSTM at a frequency of 450 kHz, it was proved that using slanted-configuration reduced-mode conversion losses. From FSRM at 390 kHz with 2.36 in. (60 mm) of Rayleigh wave propagation distance, it was observed that a good correlation between conversion losses and acoustic impedance existed, except in concrete. This is because concrete is a non-homogeneous material that causes higher energy losses due to scattering. In DTOF methodology, the SAW anisotropy was observed as a function of wave direction to the fibers. The specimens used in this experiment were wood and carbon-fiber-reinforced polymer (CFRP), which had a high elastic anisotropy. Hilbers et al. (2012) proposed detecting panel delamination in wood using air-coupled ultrasonic transducers. Three different types of wood were tested: medium-density fiberboard, particleboard, and oriented strandboard. The thicknesses of wood test specimens were 1.57 and 2.36 in. (40 and 60 mm). A central frequency of 50 kHz and through-transmission mode was used to test the specimens. The technique successfully identified the characteristics of the wood, and it contributed to characterizing different wood panels using an air-coupled ultrasonic method. Therefore,

air-coupled transducers have been observed to be effective on non-metallic materials in laboratory conditions.

A constant problem when using the air-coupled ultrasonic technique is the acoustic impedance mismatch between the air and the material. This is especially true when used with metal because metal has a much higher acoustic impedance when compared to air. Non-contact metal specimen inspection has been developed by several researchers: Blomme, Bulcaen, and Declercq (2002), Gaal, Doring, Brekow, and Kreutzbruck (2009), Delrue, Abeele, Blomme, Deveugele, and Lust (2010), Nishino, Asano, Taniquchi, Yoshida, and Ogawa (2011), Chakrapani, Dayal, Barnard, Eldal, and Krafka (2012), Dhital and Lee (2012), Penny (1976), Green (2004), and Djayaputra (2010).

Blomme et al. (2002) measured discontinuities and non-homogeneities in metal plates and welds. An air-coupled ultrasound system with a central frequency of 1 MHz and bandwidth of 600 kHz was used. Through-transmission mode was used in the experiment. They examined four different materials: low-acoustic-impedance material, textile, high-acoustic-impedance material, and steel. Blomme et al. (2002) have successfully identified discontinuities in material with a through-transmission air-coupled ultrasound. Gaal et al. (2009) used two ULTRAN probes, which have a central frequency of 330 kHz and a bandwidth of 50 to 100 kHz. An inspection of thin aluminum plates was performed using ultrasonic Lamb waves. The distance between the probes was 2.76 in. (70 mm), and the transducers were 2.17 in. (55 mm) apart from the specimen. They used the pitch-catch mode in the experiment to make a single-side inspection. Three different lengths of notches were investigated: 0.24, 0.79, and 2.36 in. (6, 20, and 60 mm). The

depth of each notch remained a constant 0.04 in. (1 mm). The signals resulting from 0.79- and 2.36-in. (20- and 60-mm) notches were clearly noticeable, but the signal from the 0.24-in. (6-mm) notch was close to the noise level. They also mentioned that the detectability depended on the number of averaged measurements. The results of this research averaged 16 measurements.

Other non-contact ultrasonic single-side inspection methods were developed by Delrue et al. (2010) on aluminum samples with artificial defects. The methods included 1) a ray tracing (shadow) approach and 2) a spectral solution implemented within COMSOL. The shadow method reduced the strength of the resulting signals if the transmitted signal was obscured by a small discontinuity. The geometry of COMSOL was a one-side inspection with pitch-catch mode using an absorptive material placed between the transducers to minimize noise. The COMSOL simulation was performed using a finite element model (FEM). The test sample of the project was an aluminum rectangular bar with dimensions of 17.32 × 2.36 × 0.79 in. (440 × 60 × 20 mm). The defect had a diameter of 0.08 in. (2 mm). A central frequency of 750 kHz and a bandwidth of 250 kHz were used. The qualitative agreement between experimental and FEM simulation results was good, and the research contributed to the field of air-coupled ultrasonic testing.

Nishino et al. (2011) accurately measured a pipe wall thickness using a circumferential Lamb wave. They placed the air-coupled ultrasonic transducers on each side of a pipe in through-transmission mode. The test specimen was an aluminum pipe with a 4.49-in. (114.1-mm) outer diameter and 0.12-in. (3-mm) thickness. The central frequency of the non-contact transducers was 340 kHz. Ten different wall thicknesses

ranging from 0 to 0.04 in. (0 to 1 mm) were prepared. The wall thicknesses of all specimens were estimated using amplitude peak position changes.

Chakrapani et al. (2012) investigated the waviness in wind turbine blades. They developed a two-step method to accomplish the project: 1) detect ultrasonic waves using air-coupled ultrasonic transducers and 2) obtain B-scan results to determine the aspect ratio. Several composite samples with different aspect ratios and depths were made. A central frequency of 200 kHz was used to generate Rayleigh waves using single-side inspection. The distance between the transducers was 3.94 in. (100 mm). The damage index number was calculated using the difference in time-of-flight between healthy and defective regions. Based on B-scan results, they concluded that as the aspect ratio increased, the damage index number also increased.

A hybrid system of an air-coupled transducer and laser was proposed by Dhital and Lee (2012). A laser was used for ultrasonic generation, and an air-coupled transducer was used as a receiver. A 0.08-in. (2-mm)-thick aluminum plate was inspected with an artificial crack having dimensions of 0.39 × 0.04 × 0.04 in. (10 × 1 × 1 mm) and a real fatigue crack on an aluminum compact tension (CT) specimen. The frequency employed in the experiment was 210 kHz. The crack was clearly identified after applying wavelet transform. On the other hand, the real fatigue crack was hard to detect, as the average crack width was 0.001 in. (0.02 mm). They adjusted the scanning interval using widths of 0.04, 0.02, and 0.002 in. (1, 0.5, and 0.05 mm). When the scanning interval was 0.002 in. (0.05 mm), the real fatigue crack was detected. They concluded that non-contact single-

side inspection (pitch-catch mode) was feasible at a high frequency range from 200 kHz to 1 MHz, as well as in through-transmission mode.

Penny (1976) introduced a laser-generated non-contact NDT method. The main idea of the research was to generate a laser pulse to the non-contact medium that generated ultrasonic acoustic waves on the surface of the specimen. The intensity of the laser pulse was kept low enough so as not to damage the specimen. The most reliable results were obtained at the highest frequency levels (or shortest wavelengths). The generated acoustic wave was the result of an impulsive expansion of the material surface caused by the absorption of the optical energy.

Green (2004) reviewed non-contact ultrasonic techniques. Because coupling mediums caused transit time errors and attenuation measurement errors, non-contact technology was proposed. This included laser generation, optic interferometric detection, electromagnetic acoustic transducers (EMATs), an air-coupled ultrasonic system, and hybrid combinations mentioned above. EMAT was good for both generators and detectors, but the test specimen had to be an electrical conductor. Air-coupled systems were limited in their frequency range, but they were better detectors than generators. Based on these studies, it was determined that conventional piezoelectric transducers with water-coupled contact could detect surface and internal horizontal cracks but not transverse, vertical, or inclined cracks. A laser Doppler vibrometer (LDV) was one of the methods that could be used as a hybrid system with another non-contact ultrasonic method. As a result of this research, LDV was shown to be a powerful method to measure ultrasonic waves that can be easily combined with other ultrasonic techniques.

Djayaputra (2010) determined the longitudinal stress in rails by using polarization of Rayleigh waves using a LDV. Polarization of Rayleigh waves was used to determine the applied stress on the rail. The ultrasonic contact transducer with a center frequency of 1 MHz was used to generate Rayleigh waves, and the LDV received the ultrasonic signal. For LDV signals, surface preparation was needed to obtain the rail surface measurement. To get the best signal, reflective tape was used on steel plates.

2.4 Air-coupled Ultrasonic Phased Array System

The air-coupled ultrasonic phased array system has been studied and developed by researchers, including Montero de Espinosa et al. (2004) and Ealo, Camacho, and Fritsch (2009). An air-coupled piezoelectric array transducer was developed by Montero de Espinosa et al. (2004). The transducer had a central frequency of 800 kHz with 39% bandwidth. It had a concave geometry with a 1.38-in. (35-mm) radius and 32 elements. Pitch-catch mode was used for paper inspection using Lamb waves. Time delay was programmed so that the beam could be focused and defocused. The transducer could steer the beam between –15 and 15°. The system successfully examined a plate-shaped material.

A ferroelectric-based multi-element array transducer was designed and fabricated by Ealo et al. (2009). Two 32-linear-element ultrasonic phased array transducers with 0.14-in. (3.43-mm) pitch and a frequency range of 30 to 300 kHz were built and tested. They examined a cylindrical reflector using pulse-echo mode using the ultrasonic phased array transducer. A microphone and LDV were used to observe the directivity and surface

velocity of their transducers. It was successfully carried out with the best result produced when the frequency was below 50 kHz.

2.5 Railway Axle Inspection Techniques

Morgan, Gonzales, Smith, and Smith (2006) monitored a railway axle body using a high-energy laser and air-coupled receivers. Transportation Technology Center, Inc. (TTCI) had two stages to develop the cracked axle detection system. The first step was to monitor a railway axle in the laboratory using the laser ultrasonic principle. Secondly, they monitored axles using the same principle in the field environment. The axles that were tested in this project were identified using a conventional NDT technique. Visual inspection, dye penetrant testing, magnetic particle testing, and conventional ultrasonic testing were used for characterization. Three 2-in. (50.8-mm) artificial cracks were made on the calibration axle. Six axles were tested: two intact axles, one calibration axle with artificial cracks along the axle body, and three axles with service defects ranging from 0.5 to 1.8 in. (12.7 to 45.72 mm) in length. The ultrasonic transducers were located 16 in. (406.4 mm) from the axle body surface, and a cylindrical lens was placed 8 in. (203.2 mm) from the surface of the axle body. The results obtained from the air-coupled transducers were processed using developmental MATLAB algorithms. A majority of defects (88%) was detected with one false crack indication. This research demonstrated that laser-based ultrasonic inspection can detect cracks both statically and dynamically. In addition, the inspection was found feasible for a semi-industrial environment.

Garcia-Ares et al. (2006) developed an automatic in-service train axle inspection system for both solid and hollow axles without the need for disassembly of the wheel sets. The system could detect all critical crack formation areas from limited access points. Therefore, minimal disassembly was required. Removal of the bearing cap was necessary for minimum inspection preparation time. For the solid axle, the probe was located on the end face. For the hollow axle, 45° angled beam transducers with a 2-MHz frequency and 70° angled beam transducers with a 4-MHz frequency were inserted into the axle bore. Standard transducers with 2.25 MHz and a 1-in. (25-mm) diameter were used for the solid axle in a contact, nondestructive manner. The solid reference axle had three cracks with dimensions of 0.5 × 0.04 in. (12 × 1 mm), 0.6 × 0.04 in. (16 × 1 mm), and 1.1 × 0.08 in. (28 × 2 mm). The hollow reference axle had two cracks with sizes of 1.2 × 0.08 in. (30 × 2 mm) and 0.8 × 0.04 in. (20 × 1 mm). All cracks were artificial cracks. The project successfully developed the inspection system for both solid and hollow axles requiring minimal disassembly. A similar method was proposed by Liaptsis et al. (2011), who demonstrated flaw detection from the end face of a railway axle using a combination of pulse-echo and pitch-catch ultrasonic phased array techniques. The research project focused on the axle journal region and the transition region between wheelseat and axle body. Used in this experiment were a 128-channel array controller, 64-element probe for the pulse-echo mode, and two 32-element probes for the pitch-catch mode. The ultrasonic phased array probes had a central frequency of 5 MHz and a sweep angle range of 0 to 60°. The axles used for calibration had artificial cracks with 0.2-, 0.1-, and 0.04-in. (5-, 3-, and 1-mm) depthss which were made by electrical discharge machining (EDM). Both

pulse-echo and pitch-catch modes were used because the threaded holes for the bearing cap created blind spots. The sizing accuracy of the EDM notches could not be measured because the P-wave used in this experiment had a large beam spread and long wavelength. The advantage of this research was that only the bearing cap disassembly was required to inspect the axle journal region.

Uchanin, Lutcenko, Dshaganjan, and Opanasenko (2010) performed railway axle inspection using the eddy current (EC) method. They used high resolution EC probes to have adequate sensitivity to substitute for magnetic particle testing. Half the axle was divided into eight sections so that a total of 32 EC probes could inspect the whole axle surface. To calibrate the system, reference standards were mounted on a part of a special tuning axle. The automated system SANK-3 with 32 EC probes increased the inspection productivity. The researchers found that the EC method had enough sensitivity to substitute for magnetic particle testing.

Hansen and Hintze (2005) tested a railway axle using the ultrasonic phased array technique. The railway axle was inspected with only four ultrasonic phased array probes, which could steer the beam angle from 25 to 75°. One rotation of the axle could map all test data along the axle. The ultrasonic phased array probe used in this experiment had 14 elements and a frequency of 2.7 MHz. The COMPAS system, which has 64-channels, was used for data acquisition (DAQ) and image processing. For calibrating the ultrasonic phased array system, 0.08-in. (2-mm)-deep artificial defects were used in the critical areas. After inspection, images of the intact and cracked axles were used to classify

serviceability. Their research provided a time-efficient way to perform mechanical inspection on each axle.

Ultrasonic phased array offers flexibility because it may be applied to many axle types and is currently the most powerful nondestructive testing technique to inspect axle journals.

2.6 Pattern Recognition Algorithms

Pattern recognition algorithms are widely used to label or classify an input value in machine learning. It helps make an inspection or manufacturing process automatic (Terzic, Nagarajah, & Alamgir 2010). Wolff and Tschope (2009) provided a summary of pattern recognition for sensor signals. There are four main processes in acoustic pattern recognizers: primary analyzer, secondary analyzer, classifier, and decision fusion. The function of the primary analyzer is to extract useful information from the original signal. Common examples of the analyzer are the auto-power spectrum or the wavelet transform. The secondary analyzer typically reduces or compresses the data from the primary analyzer. Examples include principal component analysis (PCA) and linear discriminative analysis (LDA). The classifier is the main function for acoustic pattern recognizers. It has two tasks: assessment and classification. There have been numerous classifiers used in recent studies. The simple examples include SVM, gaussian mixture model (GMM), and hidden markov model (HMM) classifiers. The final step is decision fusion. When using multiple sensors, each sensor may have distinct characteristics and therefore must be

modeled separately. Acoustic pattern recognizers have been successfully used in applications ranging from musical instruments to CFRPs.

Coccia et al. (2010) used non-contact guided wave testing of rail and detected defects using real-time statistical pattern recognition. They tested the non-contact guided wave in the field with a speed of up to 10 mph (16 km/h) and obtained good results based on the damage index. Their developed software first identified discontinuities and then classified the discontinuities as joint, internal defect, surface defect, or unclassified defect. A real-time statistical pattern recognition algorithm increased the POD. A success rate of 75 to 100% was achieved over 24 test runs with varying environmental conditions.

Cau, Fanni, Montisci, Testoni, and Usai (2006) used a neural network (NN) as their classifier tool. They developed a diagnostic system using a multi-layer perceptron (MLP) NN. As mentioned in Wolff and Tschope (2009), the original signal was processed with fast fourier transform (FFT) and principal component analysis (PCA) techniques to make an appropriate input for NN. For their defect detection phase, they developed a FEM to generate enough training datasets for MLP NN. The MLP NN had multiple layers, which included an input layer, a hidden layer, and an output layer of neurons. Using FEM, 300 defect cases were generated and used as the training dataset with a no-defect case. The classifier's mean error was 1.8%, with 96% of the cases having less than 10% error. Even though the classifier performed well, they mentioned that the neural classifier requires too much computation time to generate a sufficient training dataset.

CHAPTER III

THEORETICAL BACKGROUND

3.1 Introduction

This chapter describes the subject of wave propagation, wave interaction, attenuation, ultrasonic frequency selection, acoustic impedance, and pattern recognition algorithm. This background helps in understanding the experiments and signal processing algorithms in the following chapters.

3.2 Wave Propagation

3.2.1 Coordinate System

The coordinate system used in this chapter is defined in Figure 3.1.

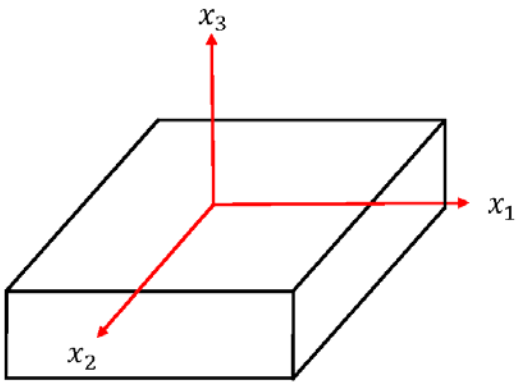

Figure 3.1. Coordinate system

3.2.2 P-Waves and S-Waves

The equation of motion of a homogenous, isotropic, and linear elastic body can be expressed using the strain-displacement relationship, generalized Hooke's law, and the stress equation of motion in terms of displacement

$$\varepsilon_{ij} = \frac{1}{2}\left(u_{i,j} + u_{j,i}\right) = \varepsilon_{ji}, \tag{3.1}$$

$$\sigma_{ij} = 2\mu\varepsilon_{ij} + \lambda\delta_{ij}\varepsilon_{kk}, \tag{3.2}$$

$$\sigma_{ji,j} + \rho f_i - \rho\ddot{u}_i = 0, \tag{3.3}$$

where ε_{ij} is the small strain tensor, $u_{i,j}$ is the displacement gradient, σ_{ij} is the stress tensor, δ_{ij} is the Kronecker delta, f_i is the body force, and ρ is the mass density. Lame's constants, μ and λ, can be defined in terms of modulus of elasticity, E and shear modulus, G

$$\mu = G = \frac{E}{2(1+\nu)}, \tag{3.4}$$

$$\lambda = \frac{E\nu}{(1+\nu)(1-2\nu)}, \tag{3.5}$$

where ν is Poisson's ratio.

Equation (3.1) is substituted into Equation (3.2) and subsequently into Equation (3.3). This derivation results in Lame-Navier equation, which is the governing equation of an elastic solid

$$\mu u_{j,ii} + (\lambda + \mu) u_{i,ij} + \rho f_i = \rho \ddot{u}_j. \tag{3.6}$$

The Lame-Navier equation is a coupled hyperbolic partial differential equation. The body force can be neglected to make the equation uncoupled. In addition, the displacement components can be expressed in terms of potentials using the Helmholtz decomposition

$$u_i = \Phi_{,i} + \epsilon_{ijk} H_{k,j}, \tag{3.7}$$

where Φ is the scalar potential, which represents an irrotational field, and H_i are the components of a vector potential indicating a solenoidal field. The displacement components are denoted using the four functions Φ, H_1, H_2, H_3. An additional constraint is required to finalize the uncoupled equation,

$$H_{i,i} = 0. \tag{3.8}$$

The uncoupled equation can be finalized by substituting Equation (3.7) into Equation (3.6). The uncoupled equations are

$$C_P^2 \nabla^2 \Phi = \frac{\partial^2 \Phi}{\partial t^2}, \tag{3.9}$$

$$C_S^2 \nabla^2 H = \frac{\partial^2 H}{\partial t^2}, \tag{3.10}$$

where C_P and C_S are the P- and S-wave speeds, respectively. They can be expressed as

$$C_P = \sqrt{\frac{\lambda + 2\mu}{\rho}} = \sqrt{\frac{E(1-v)}{\rho(1+v)(1-2v)}}, \tag{3.11}$$

$$C_S = \sqrt{\frac{\mu}{\rho}} = \sqrt{\frac{E}{2\rho(1+v)}}. \tag{3.12}$$

There are two types of elastic waves in an infinite elastic solid: P-waves and S-waves. P-waves generate only normal (compression) stresses in the solid. When an elastic wave propagates in S-wave mode, only shear stresses are generated in the solid. More detailed derivation of equations can be found in Hurlebaus (2005) on wave propagation.

3.2.3 Stress Functions in 2D In-Plane Problem

The basic solutions from Equation (3.9) and (3.10) when the direction of wave propagation in the x_1 direction is

$$\Phi = F(x_3)\mathrm{e}^{ik(x_1 - Ct)}, \tag{3.13}$$

$$H_2 = G(x_3)\mathrm{e}^{ik(x_1 - Ct)}, \tag{3.14}$$

where k is the wavenumber, and F and G are functions of x_3.

The wave potentials described in Equations (3.13) and (3.14) can be rewritten for a simple case when the wave propagates in one plane. The wave propagation on the x_1x_3 – plane is

$$\Phi(x,t) = \Phi\big(n \cdot x - C_p t\big) \tag{3.15}$$

$$= \Phi\big(n_1x_1 + n_3x_3 - C_p t\big) = \Phi\big(x_1\cos\theta + x_3\sin\theta - C_p t\big),$$

$$H(x,t) = H(n \cdot x - C_s t) \tag{3.16}$$

$$= H(n_1x_1 + n_3x_3 - C_s t) = H(x_1\cos\theta + x_3\sin\theta - C_s t).$$

The displacement and stress components are identical in any plane normal to the wave propagation direction, *n*. These planes are called wavefronts, and plane waves are defined as the propagating P-waves and S-waves with plane wavefronts.

The derivation of stress functions can be made using the general Hooke's law with Lame's constants. Using these equations, stress functions can be derived in a 2D in-plane problem (in this case, x_1 and x_3 are in-plane)

$$\sigma_{11} = \mu \cdot \big[k^2\nabla^2\Phi + 2\big(H_{,13} - \Phi_{,33}\big)\big], \tag{3.17}$$

$$\sigma_{33} = \mu \cdot \big[k^2\nabla^2\Phi - 2\big(H_{,13} + \Phi_{,33}\big)\big], \tag{3.18}$$

$$\sigma_{13} = \mu \cdot \big[2\Phi_{,13} + H_{,33} - H_{,11}\big], \tag{3.19}$$

where $k^2 = \frac{\lambda+2\mu}{\mu} = (\frac{C_p}{C_s})^2$.

3.2.4 Rayleigh Waves

The P- and S-waves are types of body waves in infinite media. The Rayleigh wave can be defined in semi-infinite media. Rayleigh waves are surface waves that propagate with boundaries in one of three directions. It is a non-dispersive wave, which means the velocity of wave is independent from the frequency. The major energy of the Rayleigh wave exists in the depth of one wavelength from the surface. It attenuates exponentially in the direction of depth.

The basic solutions, Equations (3.13) and (3.14), can be substituted into Equations (3.9) and (3.10), and the wave motions are expressed by

$$\Phi = A\mathrm{e}^{-\sqrt{k^2-k_P^2}x_3}\mathrm{e}^{ik(x_1-Ct)}, \tag{3.20}$$

$$H_2 = B\mathrm{e}^{-\sqrt{k^2-k_S^2}x_3}\mathrm{e}^{ik(x_1-Ct)}, \tag{3.21}$$

where A and B are constants and k_P and k_S are the wavenumbers of the P- and S-waves, respectively. The stresses σ_{13} and σ_{33} are zero based on the boundary condition of the half-space, $x_3 = 0$. The Rayleigh wave equation can be derived by substituting the boundary conditions into Equations (3.20) and (3.21) for the unknown wave speed C

$$\left(2 - \frac{C^2}{C_S^2}\right)^4 - 16\left(1 - \frac{C^2}{C_P^2}\right)\left(1 - \frac{C^2}{C_P^2}\right) = 0. \tag{3.22}$$

Equation (3.22) has six roots that depend on Poisson's ratio ν for a given elastic media. Because Poisson's ratio of a real medium ranges from 0 to 0.5, Graff (1991) provided an approximate expression of the Rayleigh wave C_R

$$\frac{C_R}{C_S} = \frac{0.87 + 1.12\,\nu}{1 + \nu}. \tag{3.23}$$

3.3 Wave Interaction

Mode conversion is the most common false signal in ultrasonic testing because when a wave interacts with a boundary, it splits in two types of waves. When a P-wave hits an interface at an angle, some energy can be changed to a transverse wave. The phenomenon occurs because materials have different acoustic impedances. If a wave approaches perpendicular to an interface, mode conversion will not occur. More detailed derivation of equations can be found in Kundu's (2004) work on wave interaction.

3.3.1 Snell's Law

The principal concept of wave interaction is Snell's law as shown in Figure 3.2, which describes the wave interaction between two different media, including angles of incidence and refraction

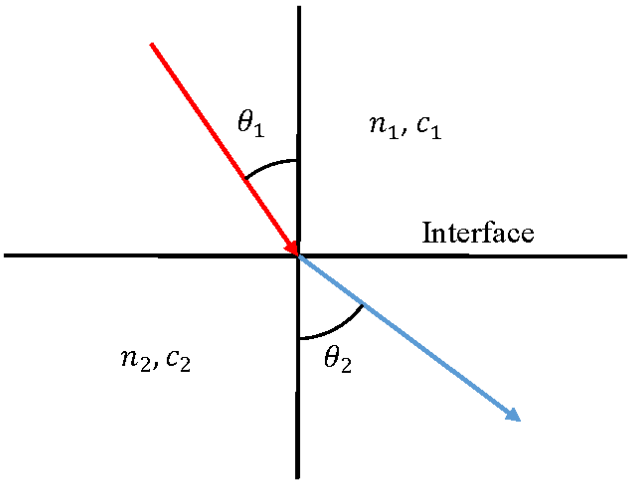

Figure 3.2. Snell's law

$$\frac{\sin\theta_1}{\sin\theta_2} = \frac{c_1}{c_2} = \frac{n_2}{n_1}, \tag{3.24}$$

where c is the wave velocity and n is the refractive index.

Using Equation (3.24), the refracted angle is adjustable from 0 to 90°.

3.3.2 P-Wave Reflection on a Stress-Free Plane Boundary

Whenever a P-wave hits a stress-free plane boundary, the wave reflects in two wave forms: the P-wave component and the S-wave component, as shown in Figure 3.3.

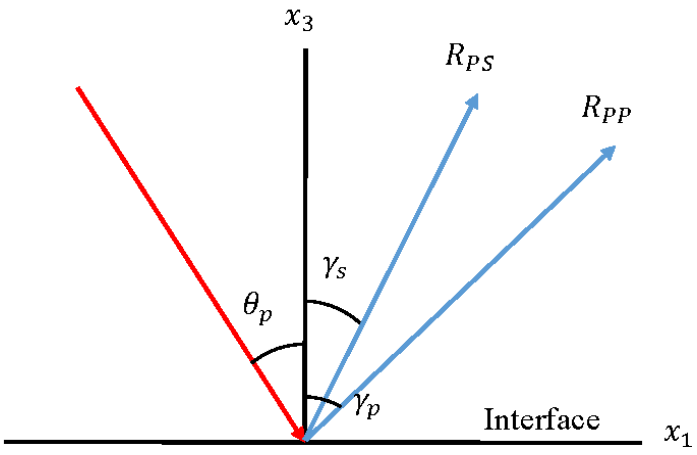

Figure 3.3. Reflection of the plane P-wave on a stress-free plane boundary

For the incident P-wave, the wave potential is

$$\Phi = e^{(ik_p x_1 \sin\theta_p - ik_p x_3 \cos\theta_p - iwt)} = e^{(ikx_1 - i\eta x_3 - iwt)}, \tag{3.25}$$

where $k = k_p \sin\theta_p$ and $\eta = k_p \cos\theta_p$.

It is assumed that the amplitude is 1. The normal and shear components at the interface are not equal to zero when $x_3 = 0$. The reflected waves, R_{PP} and R_{PS}, need to be included in wave potential to satisfy the stress-free boundary conditions at $x_3 = 0$. Both R_{PP} and R_{PS} waves are reflected waves, R. So the total potential field is

$$\Phi = \Phi_I + \Phi_R \tag{3.26}$$

$$= e^{(ik_p x_1 \sin\theta_p - ik_p x_3 \cos\theta_p - iwt)} + R_{PP} e^{(ik_p x_1 \sin\gamma_p + ik_p x_3 \cos\gamma_p - iwt)},$$

$$H = H_R = R_{PS} e^{(ik_s x_1 \sin\gamma_s + ik_s x_3 \cos\gamma_s - iwt)}, \tag{3.27}$$

where the subscript *I* indicates 'incident' and *R* indicates 'reflected.'

When the amplitude-of-incident P-waves is 1, the amplitudes of reflected P-waves and S-waves are R_{PP} and R_{PS}, respectively. Substituting wave potentials into the stress function and calculating the amplitude of reflected waves yields

$$R_{PP} = \frac{4k^2\eta\beta - (2k^2 - {k_s}^2)^2}{4k^2\eta\beta + (2k^2 - {k_s}^2)^2}, \tag{3.28}$$

$$R_{PS} = \frac{-4k\eta(2k^2 - {k_s}^2)}{4k^2\eta\beta + (2k^2 - {k_s}^2)^2}, \tag{3.29}$$

where

$$k = \frac{C_p}{C_s} = \frac{k_s}{k_p}, \text{or } k = k_p \sin\theta_p = k_s \sin\gamma_s,$$

$$\eta = k_p \cos\theta_p = \sqrt{{k_p}^2 - k^2},$$

$$\beta = k_s \cos\gamma_s = \sqrt{{k_s}^2 - k^2}.$$

3.3.3 S-Wave Reflection on a Stress-Free Plane Boundary

The amplitude of reflected S-waves can be derived in the same manner as P-waves but using different wave potentials

$$H_S = H_I = \mathrm{e}^{(ik_s x_1 \sin\theta_S - ik_s x_3 \cos\theta_S)} = \mathrm{e}^{(ikx_1 - ikx_3)}, \tag{3.30}$$

$$\Phi_{SP} = \Phi_R = R_{SP}\, \mathrm{e}^{(ikx_1 + i\eta x_3)}, \tag{3.31}$$

$$H_{SS} = H_R = R_{SS}\, e^{(ikx_1 + i\beta x_3)}. \tag{3.32}$$

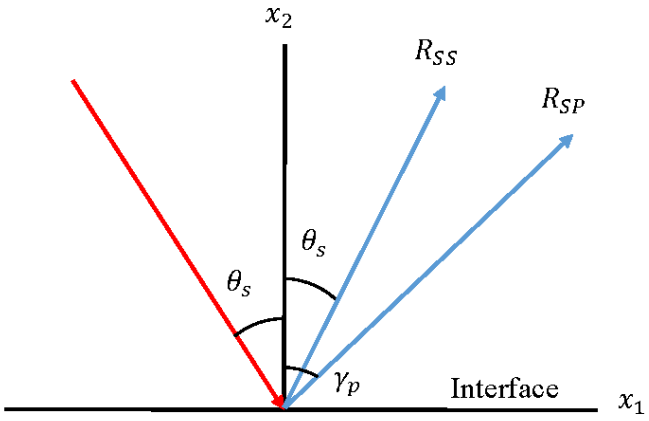

Figure 3.4. Reflection of the plane S-wave on a stress-free plane boundary

Figure 3.4 describes the S-wave reflection on a stress-free plane boundary. When the amplitude of incident S-waves is 1, the amplitudes of reflected P-waves and S-waves are R_{SP} and R_{SS}, respectively. The wave potentials are substituted into the stress function, and the amplitude of reflected waves are calculated, resulting in

$$R_{SP} = \frac{4k\beta(2k^2 - {k_s}^2)}{4k^2\eta\beta + (2k^2 - {k_s}^2)^2}, \tag{3.33}$$

$$R_{SS} = \frac{4k^2\eta\beta - (2k^2 - {k_s}^2)^2}{4k^2\eta\beta + (2k^2 - {k_s}^2)^2}, \tag{3.34}$$

where

$$k = k_S \sin\theta_S = k_P \sin\gamma_P,$$

$$\eta = k_p \cos\gamma_P = \sqrt{{k_p}^2 - k^2},$$

$$\beta = k_S \cos\theta_S = \sqrt{{k_S}^2 - k^2}.$$

3.4 Attenuation

In general, the air-coupled ultrasonic technique is challenging because of high impedance mismatch and the absorption of sound energy by air. The absorption can be expressed as

$$p(x) = p_0 \mathrm{e}^{-\alpha x}, \tag{3.35}$$

where p_0 is the pressure without energy absorption, x is the propagation distance, and α is the coefficient of absorption (dB/m). Equation (3.36) was developed by Bass, Sutherland, and Zuckerwar (1990) and Bass, Sutherland, Zuckerwar, Blaxkstock, and Hester (1995) to compute the coefficient of absorption

$$\frac{\alpha}{p_s} = \frac{F^2}{p_{s0}}\left\{1.84\times10^{-11}\left(\frac{T}{T_0}\right)^{\frac{1}{2}}\right. \tag{3.36}$$

$$+\left(\frac{T}{T_0}\right)^{-\frac{5}{2}}\left[0.01278\frac{\mathrm{e}^{-\frac{2239.1}{T}}}{F_{r,o}+\frac{F^2}{F_{r,o}}}\right.$$

$$\left.\left.+\,0.1068\frac{\mathrm{e}^{-\frac{3352}{T}}}{F_{r,N}+\frac{F^2}{F_{r,N}}}\right]\right\}\left(\frac{\text{nepers}}{\text{m}-\text{atm}}\right),$$

where

p_s is atmospheric pressure (atm),

p_{s0} is the reference value of atmospheric pressure (atm),

f is the frequency of the sound (50 to 10,000 Hz/atm),

F is f/p_s frequency scaled by atmospheric pressure (Hz),

T is air temperature (K),

T_0 is normal air temperature (T_0= 293.15 K),

$f_{r,o}$ is the absorption frequency of O_2 (Hz),

$F_{r,o}$ is $f_{r,o}/p_s$ frequency scaled by atmospheric pressure (Hz),

$$F_{r,o} = \frac{1}{p_{s0}}\left(24+4.04\times10^4 h\frac{0.02+h}{0.391+h}\right), \tag{3.37}$$

$f_{r,N}$ is the absorption frequency of N_2 (Hz),

$F_{r,N}$ is $f_{r,N}/p_s$ frequency scaled by atmospheric pressure (Hz),

$$F_{r,N} = \frac{1}{p_{s0}}\left(\frac{T_0}{T}\right)^{\frac{1}{2}}\left(9 + 280h \times \exp\left\{-4.17\left[\left(\frac{T_0}{T}\right)^{\frac{1}{3}} - 1\right]\right\}\right), \tag{3.38}$$

h is the humidity and h_r is the relative humidity (%),

$$h = h_r \frac{p_{sat}p_{s0}}{p_s p_{s0}} = p_{s0}\left(\frac{h_r}{p_s}\right)\left(\frac{p_{sat}}{p_{so}}\right)\%. \tag{3.39}$$

Based on Equation (3.36), it is clear that the energy loss increases as the frequency increases.

3.5 Ultrasonic Frequency Selection

Selecting the central frequency of the ultrasonic probe is determined by the crack inspection rule of thumb. The minimum detectable crack size can be calculated as

$$\lambda \geq 2 \times \text{flaw size}, \tag{3.40}$$

$$V = f \times \lambda. \tag{3.41}$$

For example, given the P-wave speed of steel, V = 230,000 in/s (5,842 m/s) and the central frequency f = 5 MHz. The wavelength can be calculated as λ = 0.046 in. (1.17 mm). Therefore, the theoretical minimum detectable crack size is 0.023 in. (0.584 mm). This is only a theoretical value; it typically depends on the consistency of coupling, attenuation, and other environmental factors.

3.6 Acoustic Impedance of Materials

Acoustic impedance is defined as the product of the density and velocity of a material

$$Z = \rho \cdot C_P. \tag{3.42}$$

Table 3.1 shows commonly used acoustic impedance for ultrasonic testing.

Table 3.1. Acoustic impedance in metric units

Materials	Acoustic Impedance (Z) (kg/m^{2}s)
Air	0.0004
Water	1.48
Polymethyl methacrylate (PMMA)	3.26
Steel	46.7

Most of the energy is reflected onto any interface between the air and solid material because the acoustic impedance of air is only 5.69×10^{-7} lb/in.^{2}s (0.0004 kg/m^{2}s), which is extremely small compared to that of other materials. The percentage of reflected energy can be calculated as

$$\text{Reflected Energy (\%)} = \left(\frac{Z_1 - Z_2}{Z_1 + Z_2}\right)^2 \times 100\%. \tag{3.43}$$

Based on the theoretical results, the percentage of transmitted energy between air and steel is 0.004%. It is for this reason that most ultrasonic techniques use a coupling medium to reduce the acoustic impedance mismatch. Inevitably, higher power generation is required to overcome the high acoustic impedance mismatch between steel and air.

3.7 Pattern Recognition Algorithms

3.7.1 SVM

A supervised learning algorithm, SVM, was introduced by Vapnik (1995). A hyperplane can be constructed using the training data

$$(x_1, y_1), \cdots, (x_l, y_l), x_i \in R^n, y_i \in \{1, -1\}, \tag{3.44}$$

where x_i is the feature vector and y_i is the corresponding class of x_i. The training data are plotted on 2D plane. SVM classifies the data of one class from another class using a hyperplane. A hyperplane can be described as

$$w \cdot x - b = 0, \tag{3.45}$$

where w is a normal vector perpendicular to the hyperplane and b is the bias value of the hyperplane. The main goal of SVM is to create an optimum margin so that two classes of data can be separated as far as possible. The margin of a hyperplane can be defined as

$$(w \cdot x_i) - b \geq 1, \qquad if\ y_i = 1, \tag{3.46}$$

$$(w \cdot x_i) - b \leq -1, \qquad if\ y_i = -1. \tag{3.47}$$

The maximum margin hyperplane is when

$$(w \cdot x_i) - b = 1, \qquad if\ y_i = 1, \tag{3.48}$$

$$(w \cdot x_i) - b = -1, \qquad if\ y_i = -1. \tag{3.49}$$

A compact notation for the above inequalities is expressed as

$$y_i[(w \cdot x_i) - b] \geq 1, i = 1, \cdots, l. \tag{3.50}$$

The optimum hyperplane satisfies Equation (3.50) and minimizes

$$\Phi(w) = \|w\|^2 = \frac{1}{2}(w \cdot w). \tag{3.51}$$

The Lagrangian is used to solve this optimization problem

$$L(w, b, \alpha) = \|w\|^2 - \sum_{i=1}^{l} \alpha_i \{[(w \cdot x_i) - b] y_i - 1\}, \tag{3.52}$$

where α_i are Lagrange multipliers. At the saddle point of the Lagrangian, the solutions should satisfy the conditions

$$\frac{\partial L(w_0, b_0, \alpha^0)}{\partial b} = 0, \tag{3.53}$$

$$\frac{\partial L(w_0, b_0, \alpha^0)}{\partial w} = 0, \tag{3.54}$$

because the Lagrangian must be minimized with respect to w and b. The Lagrange multipliers can be computed with the constraints

$$\sum_{i=1}^{l} \alpha_i^0 \, y_i = 0, \qquad \alpha_i^0 \geq 0, \qquad i = 1, \ldots, l. \tag{3.55}$$

The solution of w and b can be defined as

$$w_0 = \sum_{i=1}^{l} y_i \alpha_i^0 x_i = 0, \qquad \alpha_i^0 \geq 0, \qquad i = 1, \ldots, l, \tag{3.56}$$

$$b_0 = \frac{1}{2}\left[\left(w_0 \cdot \, x^*(1)\right) + \left(w_0 \cdot \, x^*(-1)\right)\right]. \tag{3.57}$$

It is denoted that $x^*(1)$ belongs to the first class and $x^*(-1)$ belongs to the second class. The theoretical detail and derivation are explained in Vapnik (1995).

3.7.2 Signal Processing with Threshold Classifier

An image contains red, green, and blue (RGB) data. The main color of images that are obtained from the DAQ system is blue. Only blue data are used in this case. An image has a matrix of 400 × 615. The root-mean-square values can be computed as

$$x_{\text{rms}} = \sqrt{\frac{(x_1^2 + \cdots + x_n^2)}{n}}. \tag{3.58}$$

Absolute difference between the raw blue data and root-mean-square can be computed by

$$x_{\text{difference}} = |x_{\text{blue}} - x_{\text{rms}}|. \tag{3.59}$$

The difference ratio values are calculated with the following equation

$$x_{\text{ratio}} = \frac{x_{\text{difference}}}{x_{\text{blue}}}. \tag{3.60}$$

To avoid singularity, the shifted difference ratio values are computed as

$$x_{\text{shift}} = \frac{x_{\text{difference}} + 1}{x_{\text{blue}} + 1}. \tag{3.61}$$

These values are used as a feature vector. The shifted difference ratio values are classified based on the threshold value of a 1-mm crack depth.

CHAPTER IV

PRELIMINARY STUDIES

4.1 Introduction

This chapter covers FEM, investigation of axle, wedge selection, and ultrasonic wave detection with LDV. The feasibility of ultrasonic phased array is checked with the simulation of wave propagation in an axle. The unknown crack sizes are found in the axle specimen. A transducer wedge is carefully selected to obtain an optimum result. The different ultrasonic wave types are compared using LDV. This provides a background to the experiments in the following chapters.

4.2 FEM

The purpose of FEM in this research is to validate flaw detection on a train axle using the ultrasonic phased array technique. Commercially available software, ABAQUS, is used in this modeling procedure. ABAQUS/Explicit analysis is used in this research because it is particularly well-matched to simulate transient dynamic problems.

4.2.1 Parameters

Table 4.1 contains the elastic material properties used in the simulation, including Young's modulus, E, weight density, ρ, and Poisson's ratio, ν.

Table 4.1. Material properties of ABAQUS simulation

	Material Properties	
E	200	GPa
ρ	7,860	kg/m^3
ν	0.3	-

The total length of an ultrasonic phased array probe is set to 1 in. (25.4 mm). The simulation employs 11 elements, and the pitch is set to 0.1 in. (2.5 mm). Table 4.2 shows the case studies for mesh sensitivity.

Table 4.2. Parameters of different case studies

	Number of Segments	Sampling Time (ns)	Element Length (mm)
Case 1	2	500	3
Case 2	4	250	1.5
Case 3	8	125	0.73
Case 4	16	62.5	0.36
Case 5	32	31.25	0.18

The theoretical wave speed of steel is 230,433.01 in/s (5,853 m/s), and arrival time is 0.141 ms. A wave frequency of 1 MHz is used for high-frequency validation. A wavelength of 0.023 in. (0.585 mm) is calculated based on frequency and wave speed.

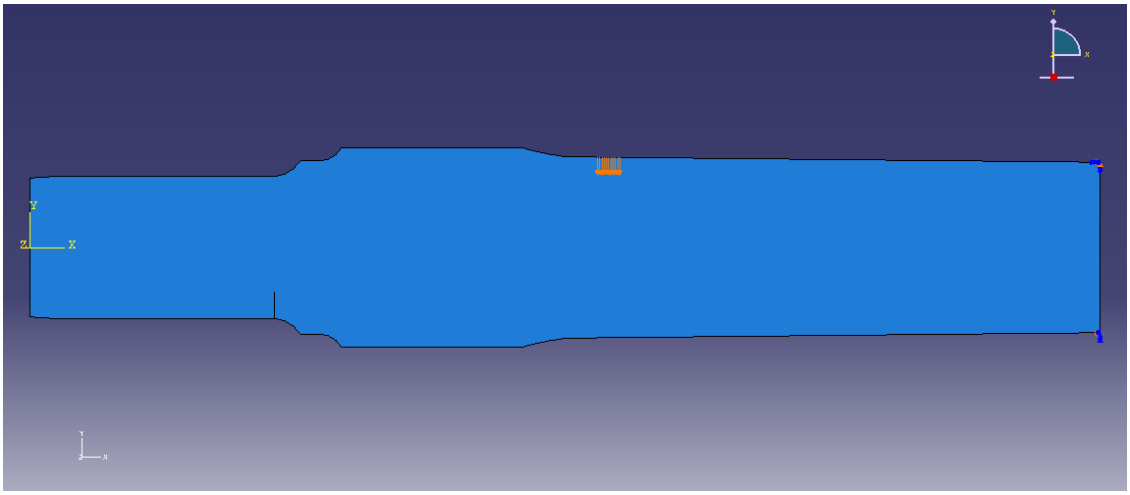

Figure 4.1. Ultrasonic phased array model on axle

Figure 4.1 shows the FEM model of an ultrasonic phased array signal and the location of a crack at the axle journal region. It is modeled with a 2D plane strain model, and only half the axle is modeled to reduce computation time.

4.2.2 Element Selection

A plane strain element, CPE4R, and a 2D quadrilateral element are used. CPE4R indicates a four-node, bilinear, reduced integration with hourglass control. When the first-order and reduced integration elements are used in stress/displacement analyses, the hourglass is a main issue. Hourglass-control minimizes the distortion of elements. Reduced integration is essential on ABAQUS/Explicit due to the computation time and cost.

4.2.3 Results and Discussions

Multiple simulation results are obtained with different parameters. Based on Table 4.2, the mesh sensitivity study is done, as shown in Figure 4.2. With 32 segments per wavelength, the error is reduced to 0.3%.

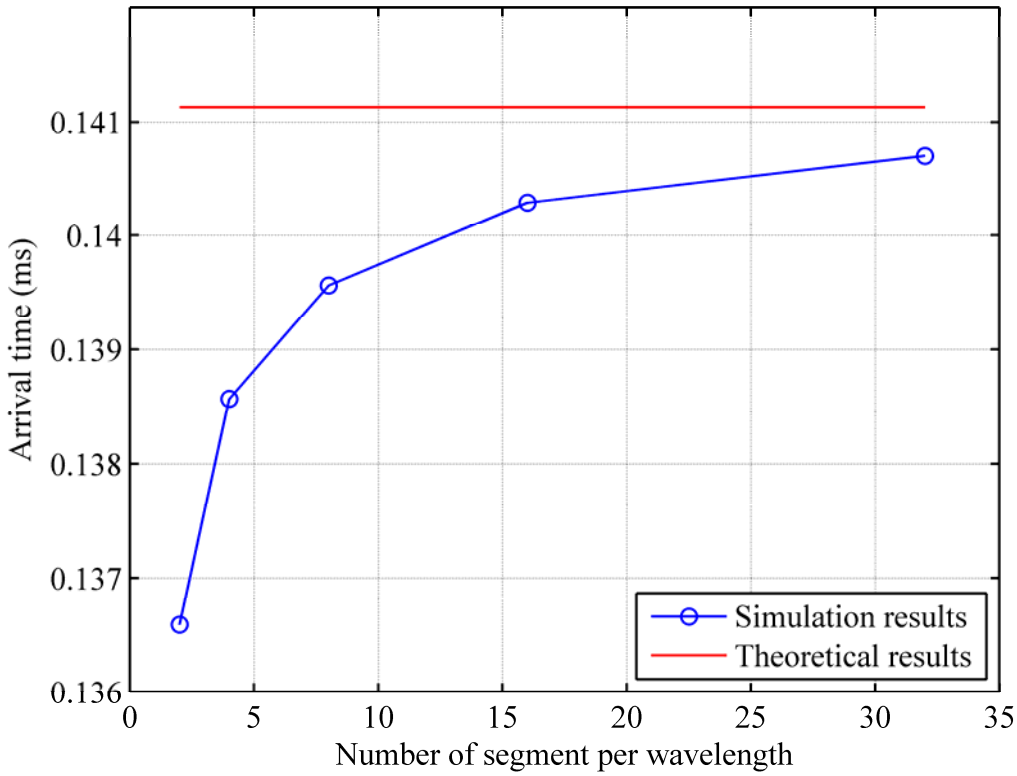

Figure 4.2. Mesh sensitivity study

Finally, cracked axle signal and intact axle signal are compared. Figure 4.3 gives the case when 32 segments per wavelength, 32.25-ns sampling time, and 0.0071-in. (0.18-mm) element size are used. The displacement is in atto-meters (1 am = 10^{-18} m).

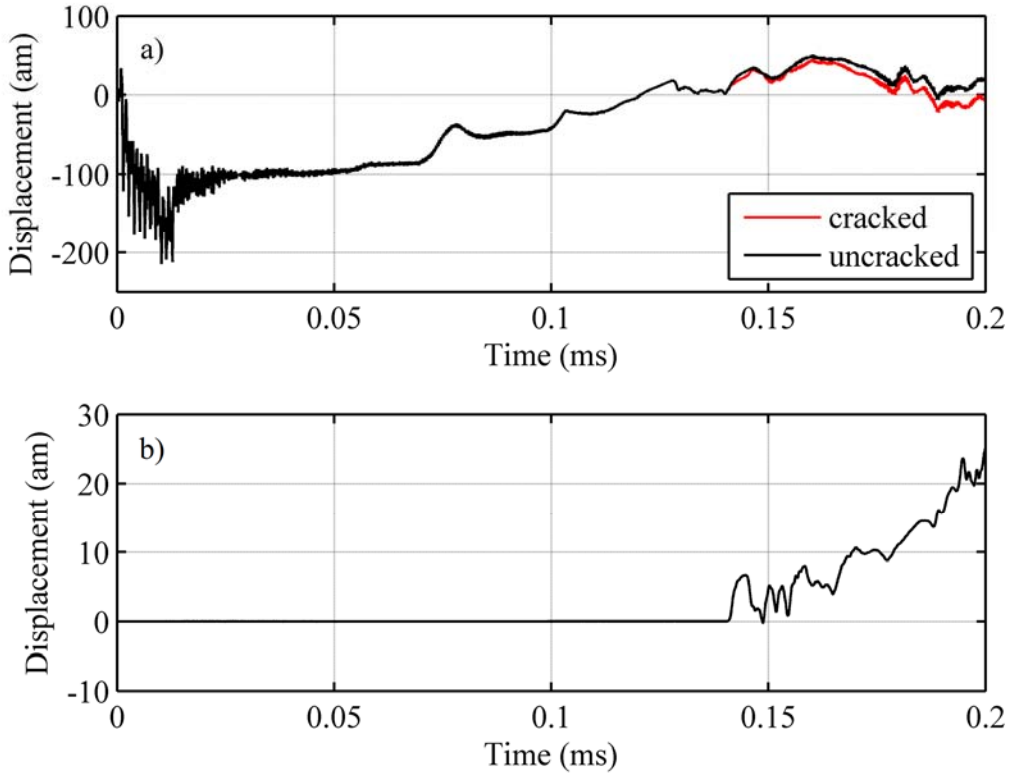

Figure 4.3. Comparison of cracked and uncracked signal: a) 11 array excitations with n = 32 and b) difference of the signals

It is shown that the ultrasonic phased array system detects the cracks on railway axle journals. The central frequency of the transducer and input voltage need to be adjusted based on research needs.

4.3 Axle Investigation

Union Pacific Railroad Co. donated a cracked axle to Texas A&M University. There are a total of 14-laser made cracks in several locations, including the journal, wheelseat, and axle body. All cracks have a 1-in. (25.4-mm) length on the surface. The

depth of cracks can be determined using ultrasonic techniques such as the tip-echo diffraction technique**.** The tip-echo diffraction technique separates the backscattering signal from a crack tip and base. A crack size can be estimated by taking the difference between the tip and base signals. Jacques, Moreau, and Ginzel (2003) recommended using a refracted angle of 45˚ for weld sizing using the tip diffraction technique. The same principle is used for the axle crack sizing. However, it is found that a refracted angle of 60 to 65˚ works best for the railway axle. This difference can be attributed to the material's thickness. The weld inspection is normally performed for a material thickness less than 1.97 in. (50 mm), whereas the railway axle has an approximate diameter of 7.87 in. (200 mm).

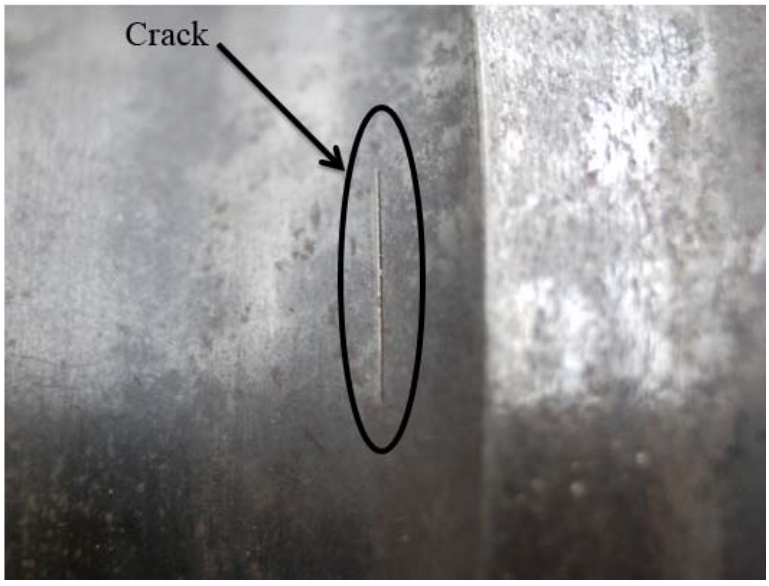

Figure 4.4. Crack shape

Figure 4.4 shows an image of the crack shape. Figure 4.5 provides an example of crack sizing using the tip diffraction technique.

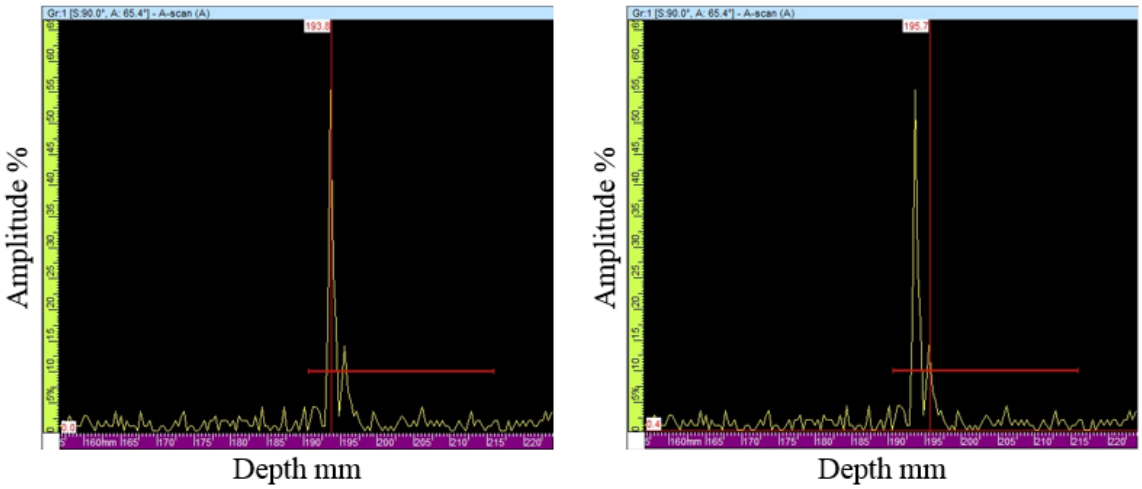

Figure 4.5. Example of crack sizing using tip diffraction technique

Crack sizing can be done using direct and diffracted signals of crack base and tip, respectively. Taking the difference of the two depths gives a crack size. Figure 4.6 shows the location of cracks, and Table 4.3 lists the depths estimated using the tip diffraction technique. All cracks have the length of 1 in. (25.4 mm).

Figure 4.6. Location of cracks

Table 4.3. Estimated crack depth

Number	Depth (mm)	Number	Depth (mm)	Number	Depth (mm)
1	1	6	2	11	3
2	1	7	2	12	2
3	2	8	1	13	1
4	1	9	3	14	2
5	1	10	4		

There is a possible error in this experiment due to a difference between the geometry of the axle and that recognized by the ultrasonic phased array device. The system only allows the input of the specimen thickness, essentially requiring a rectangular profile. Furthermore, the axle has a different diameter on journal sections, and the mid-region has a tapered section. Figure 4.7 represents the difference between the actual geometry of the axle and the device's geometry recognition. These can lead to miscalculations of the defect location and depth.

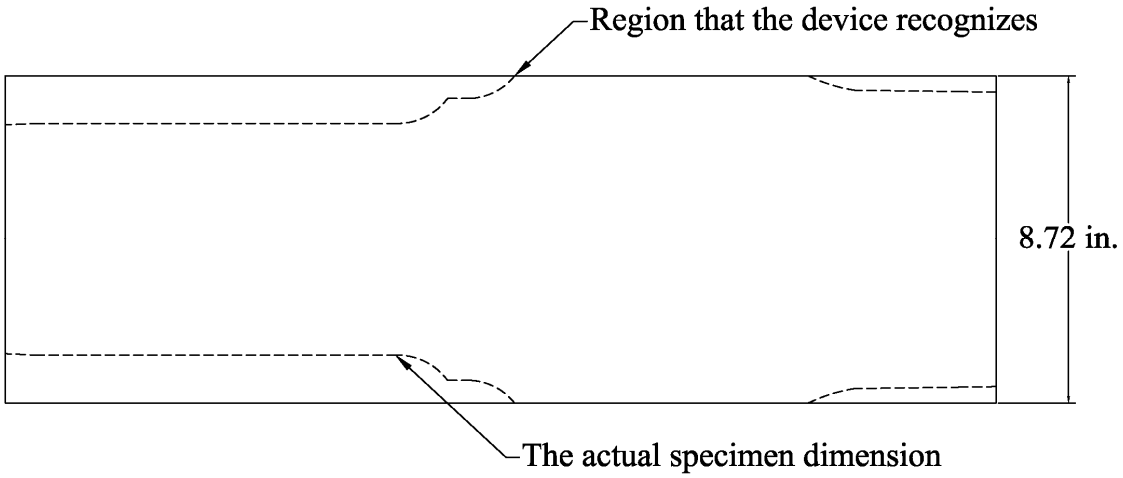

Figure 4.7. Difference between actual geometry and the ultrasonic phased array system's geometry recognition

4.4 Wedge Selection

A commercially available wedge has a flat contact surface and therefore is not designed to examine a specimen with a contoured surface. As shown in Figure 4.8 below, there is a varied gap between the probe and the specimen. Ginzel and Thompson (2011) state that the European code (EN 1714) requires that if gaps greater than 0.0197 in. (0.5 mm) exist, a contoured probe wedge has to be used. Because the gap in this case is 0.0203 in. (0.516 mm), which is over 0.0197 in. (0.5 mm), it is recommended to use a contoured probe wedge for better accuracy of results.

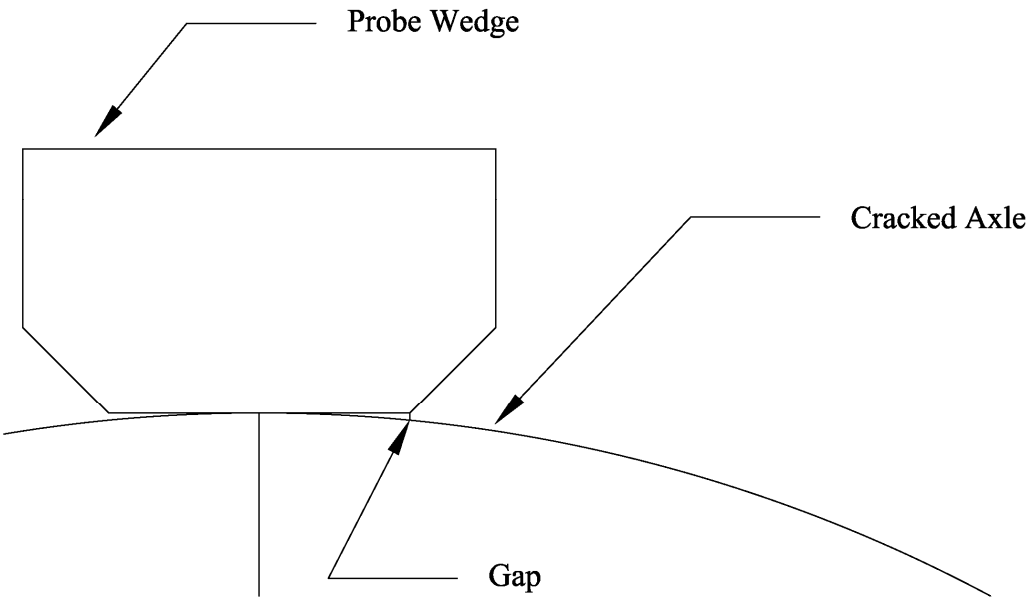

Figure 4.8. Gap between probe wedge and axle

4.5 Ultrasonic Wave Detection with LDV

Ultrasonic waves, which consist of P-waves, S-waves, and Rayleigh waves, are measured and compared using an angled ultrasonic beam with LDV. After 512 samples are obtained, the signals are averaged by an oscilloscope. A conventional ultrasonic transducer is used with a central frequency of 2.25 MHz. Figure 4.9 describes the experimental setup of ultrasonic wave detection. The incident angle is adjusted using Snell's law. Figure 4.10 shows the adjustable wedge.

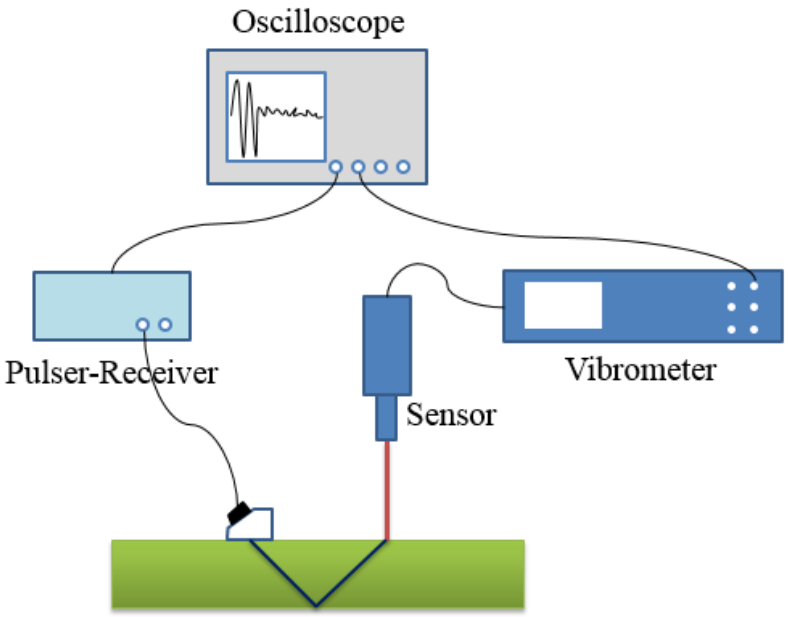

Figure 4.9. Experimental setup for ultrasonic detection

Figure 4.10. Adjustable angled wedge

Four different measurements are taken using through-transmission mode and pitch-catch mode. As shown in Figure 4.11, a) is through-transmission mode and b), c), and d) are pitch-catch mode.

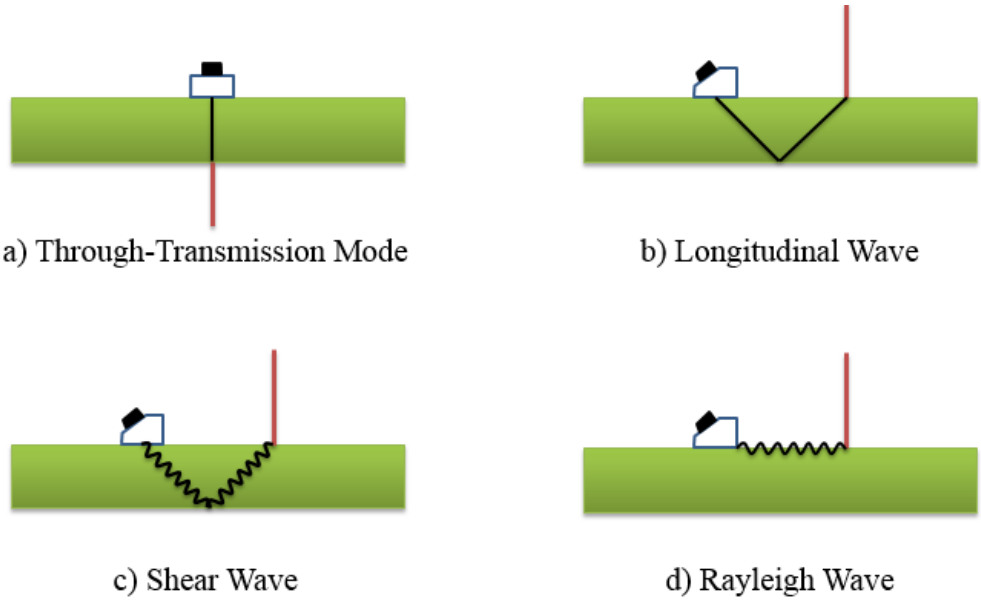

Figure 4.11. Different wave path

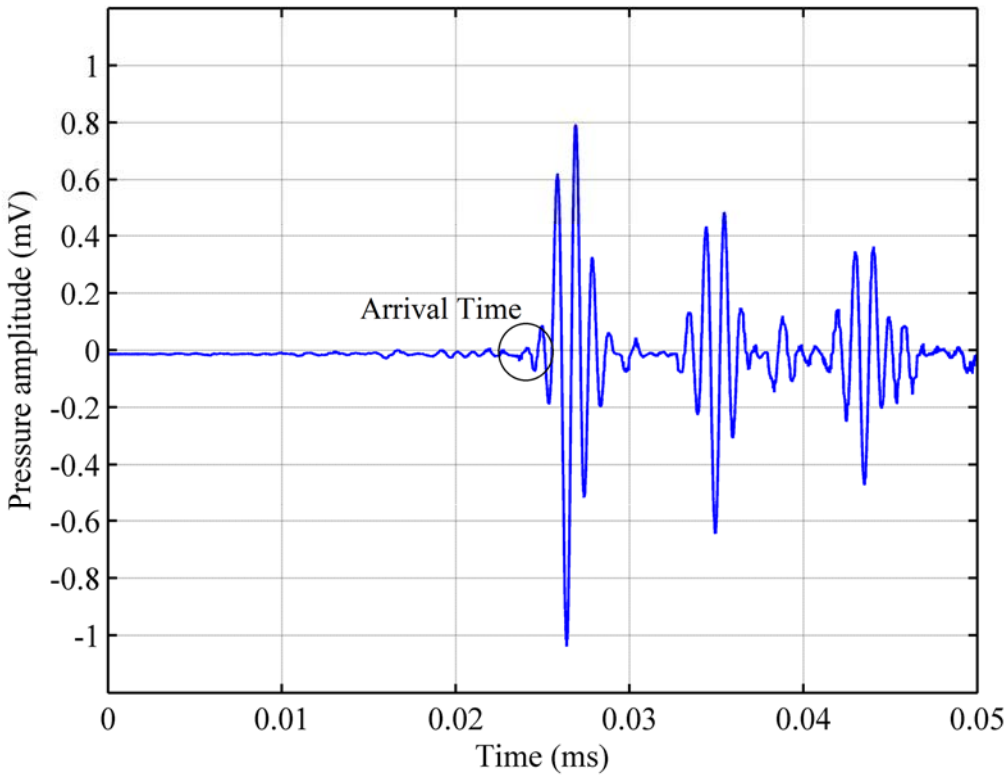

Figure 4.12. Through-transmission mode using P-waves

Through-transmission mode, as shown in Figure 4.12, allows for the calculation of wedge delay, which is 19.44 μs. The specimen has the thickness of 1 in. (25.4 mm). The theoretical wave propagation time on the steel specimen is 4.40 μs. It is subtracted from the total wave propagation time of 23.84 μs.

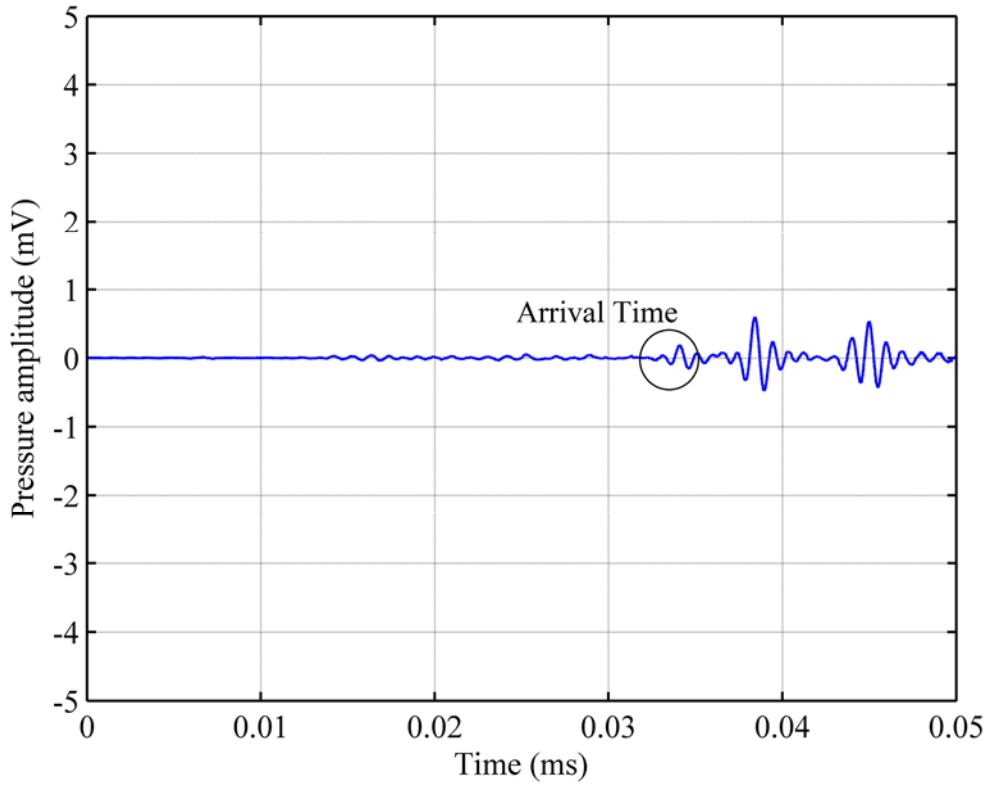

Figure 4.13. P-wave detection

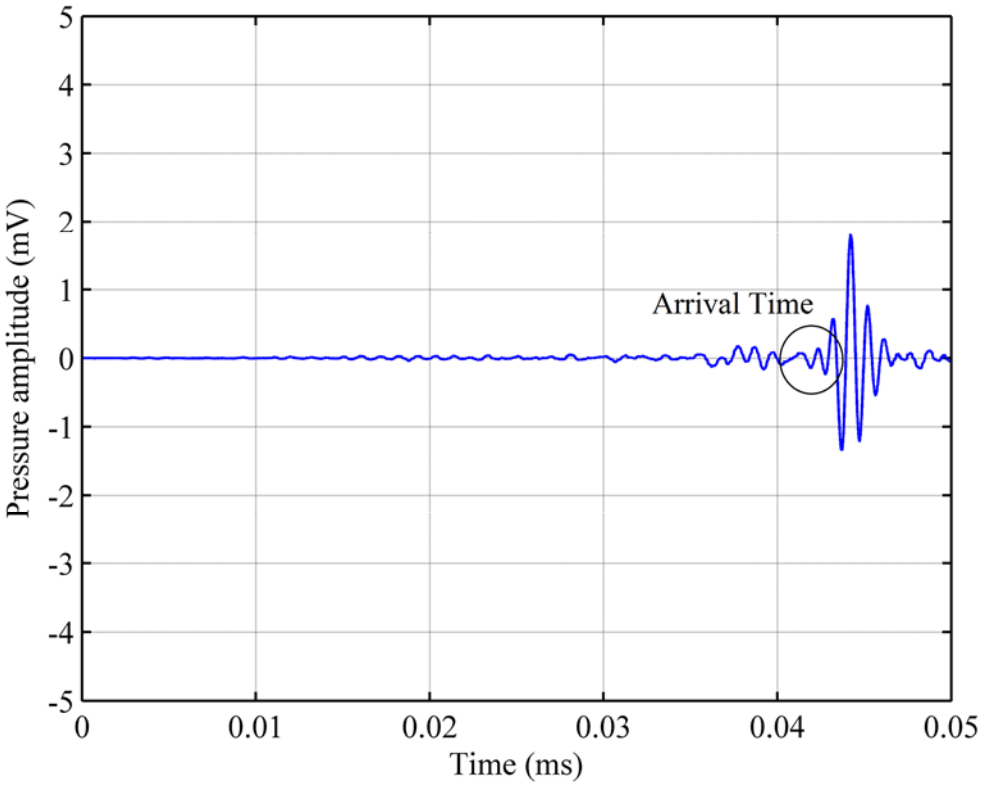

Figure 4.14. S-wave detection

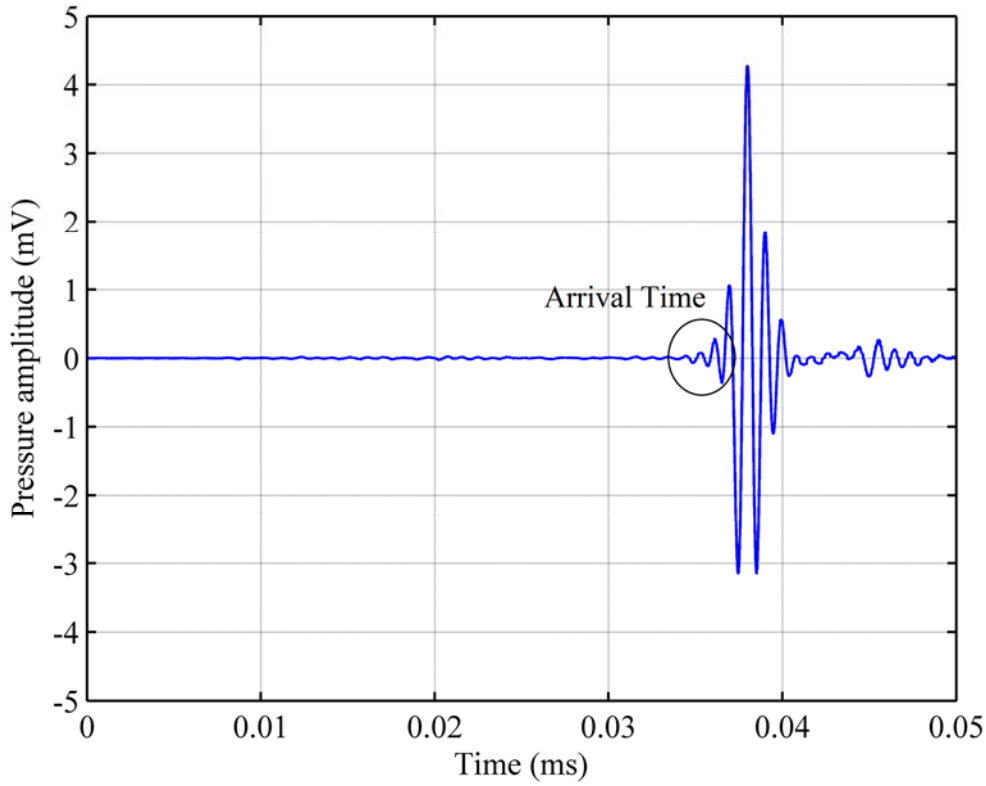

Figure 4.15. Rayleigh wave detection

Table 4.4. Comparison of results among ultrasonic wave types

	P-wave	S-wave	Rayleigh wave
Incident angle (°)	19	37	65
Refracted angle (°)	45	45	90
Propagation length (mm)	71.8	71.8	50.8
Wave speed (m/s)	5,770.8	3,138.5	2,906.9
Expected time (μs)	31.89	42.33	36.92
Experimental time (μs)	32.55	41.59	35.13
Error (%)	2.1	1.7	4.8

Table 4.4 shows a comparison of results from Figure 4.13 to 4.15. From the three plots, it is clear that the P-wave has the smallest amplitude and the Rayleigh wave has the largest amplitude. It is therefore recommended that the Rayleigh wave be utilized for one-side surface crack detection.

4.6 Conclusions

Based on in FEM results of ultrasonic wave propagation, it is shown that the ultrasonic phased array technique is able to detect discontinuities on the railway axle journal. The crack sizes of the axle specimen are carefully investigated, and measured crack sizes will be used as a baseline for further experiments. A curved wedge is recommended for the cracked railway axle research to minimize errors due to coupling. Finally, ultrasonic wave detection on LDV is performed for P-, S-, and Rayleigh waves. LDV can be used as a signal receiver for all wave types.

CHAPTER V

RAILWAY AXLE JOURNAL INSPECTION USING ULTRASONIC PHASED ARRAY TECHNIQUE*

5.1 Introduction

The primary objective of this research is to design an automated detection of cracked railway axle journals. A non-contact NDT inspection technique could be a candidate for the detection system, but it has many problems among current technology. The two major problems with non-contact ultrasonic are the attenuation of acoustic waves in the air and the large acoustic impedance mismatch between steel and air. The current inspection system requires that axles be disassembled from bogie cars, making the inspection both time-intensive and expensive. Establishing a method to inspect the railway axle on moving trains is a major need in this field of study. A portable axle inspection system, which can easily go underneath railway cars, is also desirable.

Any axle that has a defect greater than 0.12 in. (3 mm) must be removed from service (AAR 1984 and ARTC 2005). Therefore, the ultrasonic device is calibrated to detect defects less than 0.12 in. (3 mm). To increase the inspection interval time, the size of detectable cracks needs to be smaller. In addition, the cracked axle is tested in laboratory conditions with a contact ultrasonic phased array technique. It is important to keep the axle rotation and the coupling constant. Also, a chain scanner is applied to the axle as a different inspection method. The goal of these experiments is to inspect train axles without requiring disassembly.

---

*This article appeared in Structural Health Monitoring 2013-Proceedings of the 9th International Workshop on Structural Health Monitoring, 2013. Lancaster, PA: DEStech Publications, Inc.

5.2 Experimental Setup

An automated inspection system and a manual inspection system are developed and are presented in this section. Figure 5.1 shows an overview of the automated system. Axles are scanned using automated or manual techniques, and the results are saved in the DAQ system. Finally, to minimize any human involvement, a pattern recognition algorithm is performed by a computer.

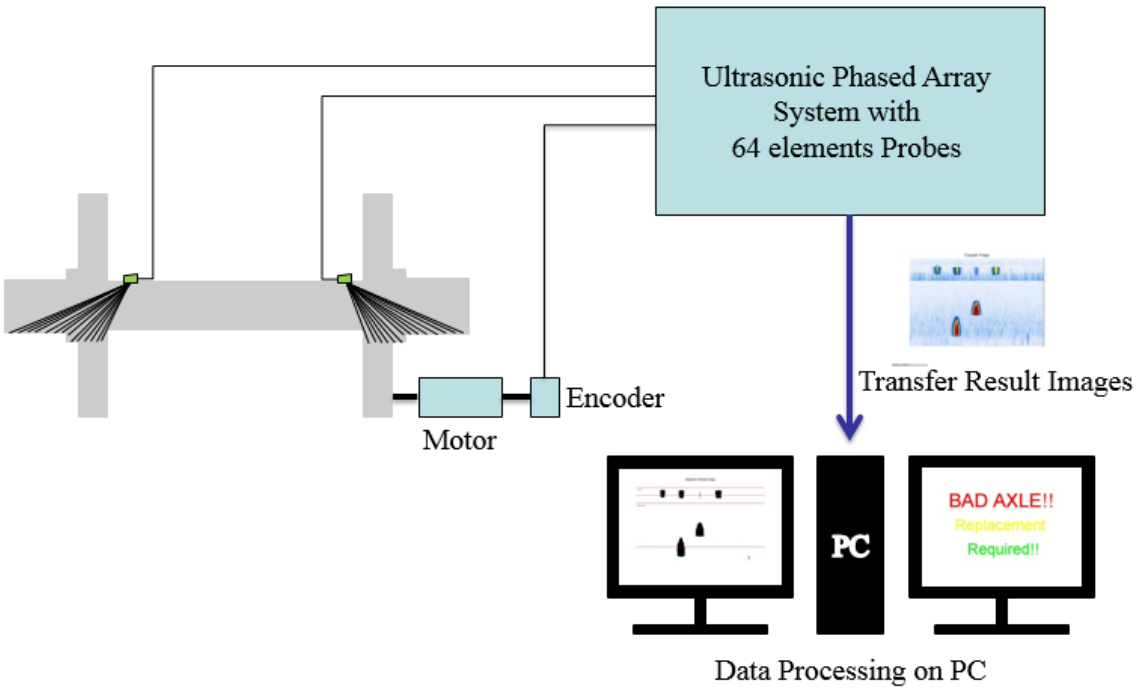

Figure 5.1. Automated inspection system overview

5.2.1 Frame Design

The main component of the fixture designed to inspect railway axle journals is an aluminum structural frame. The motor, controller, water pump, and encoder are attached

to the fixture, as shown in Figure 5.2. Bolt strength, flexural capacity, and torque on the shaft were considered in the design of the frame. The biggest issue in this design is the tolerance of the bearings, wheels, and shafts. The tolerance of parts is within 0.001 in. (0.0254 mm) and hence are difficult to assemble.

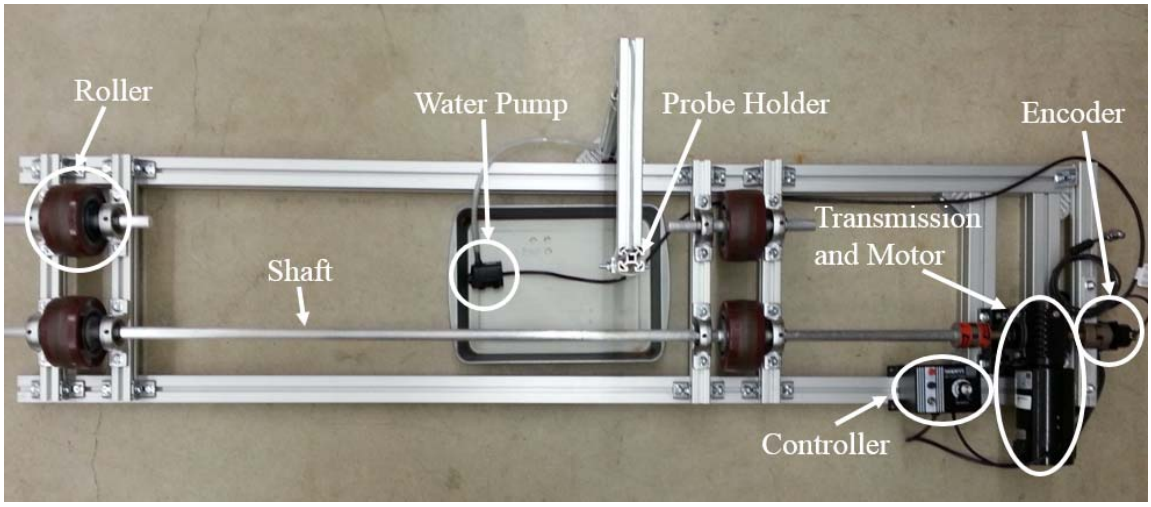

Figure 5.2. Detection system frame

The motor (42A-5H series DC right angle gearmotor Model 4101) has 23.8-lb-ft (32.3-Nm) peak torque and ½ hp, which is enough to rotate the axle. The motor is connected to the controller (type WPM filtered PWM speed controls for permanent magnet DC brush motors—Model 0791), which controls the rotation speed of the axle. The encoder (Incremental Encoder Series TRD-N1000-RZWD) is also attached to the motor. It is wired to the DE-15 connector to make it compatible with the DAQ system. The water pump (Beckett 130 GPH submersible fountain pump) is attached to provide a constant flow of water between the specimen and wedge for coupling.

5.2.2 Ultrasonic Phased Array System

Olympus Omniscan MX2 with 16:64 ultrasonic phased array acquisition modules is used for the DAQ system. The system can display the results from the A-scan, B-scan, C-scan, and S-scan, as shown in Figure 5.3. The focal law is preset between 30 and 70˚ based on the recommendation from the manufacturer.

Figure 5.3. Ultrasonic phased array DAQ system

A one-dimensional (1D) linear phased array probe with 64 elements, 5 MHz, and 0.0236-in. (0.6-mm) pitch is selected for this experiment. A curvature contact faced wedge is used with an irrigation holes and carbides (IHC) feature—irrigation holes for coupling supply and carbides legs for preventing wear of wedge. The wedge with curvature is well-

suited for the specimen, which has an 8-in. (203-mm) diameter. Figure 5.4 shows the ultrasonic phased array probe and wedge, and Figure 5.5 shows the experimental setup for the automated detection system.

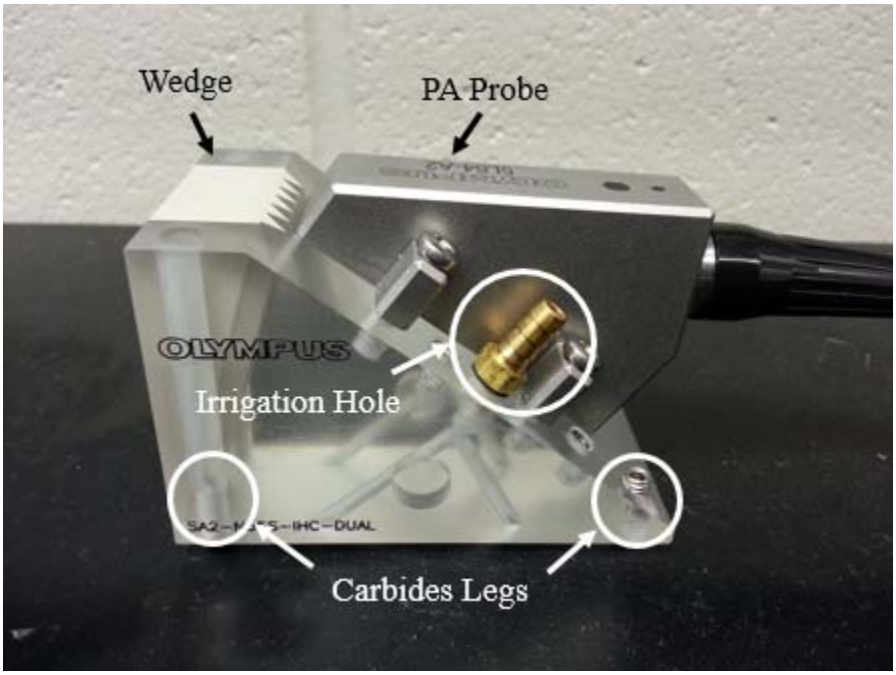

Figure 5.4. Ultrasonic phased array probe and curved wedge

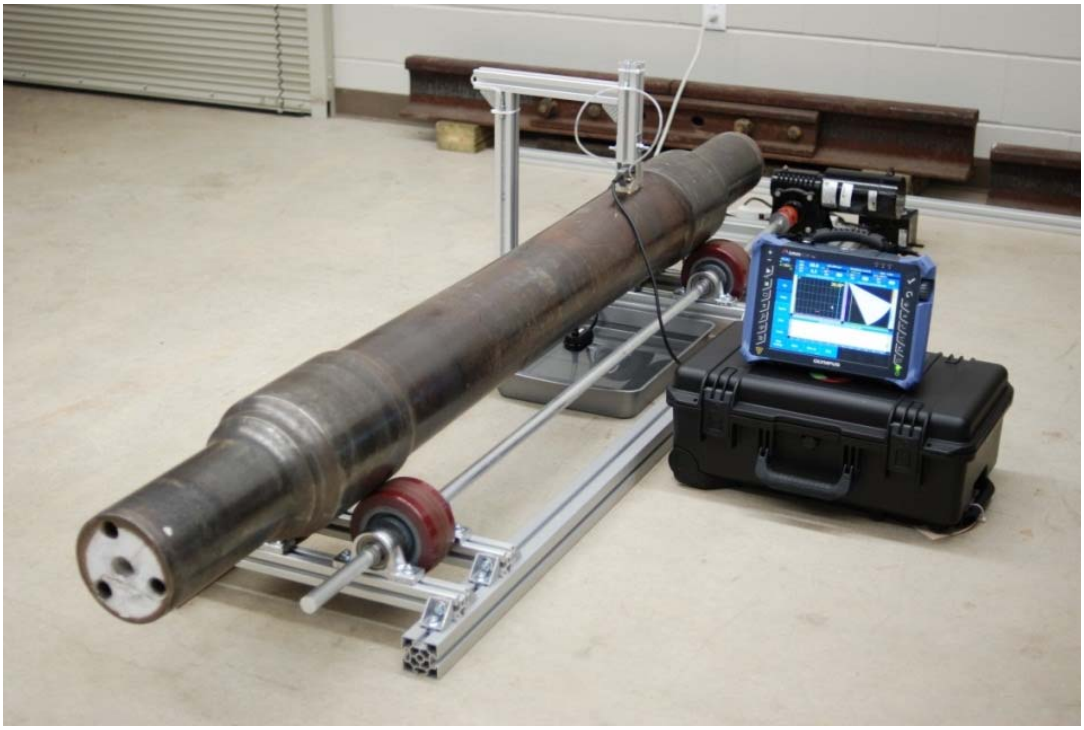

Figure 5.5. Experimental setup for automated detection system

The surface of the axle must be cleaned to obtain accurate results. Though it is not a significant issue in a laboratory test environment, in field conditions, surface preparation is a major concern for contact ultrasonic inspection. Because this application can be applied to a moving train, it is worth investigating how fast the axle can rotate and still give reliable inspection results.

5.2.3 Hand-Held Chain Scanner

A chain scanner is also used to inspect the train axle journals. The scanner is capable of two encoded axes. The axes are the circumference of the axle (X) and the axis along an axle (Y). The resolutions of encoder for the X and Y axes are 487.7 and 5,760.7

steps/in. (19.2 and 226.8 steps/mm), respectively. In this experiment, the axle is fixed while the scanner and probe move. This type of scanner is commonly used for pipe inspection. The chain link can hold the probe and scanner in position which helps to eliminate steering problems associated with the mouse-type scanner. Figure 5.6 shows the test setup of railway axle journal inspection using a chain scanner.

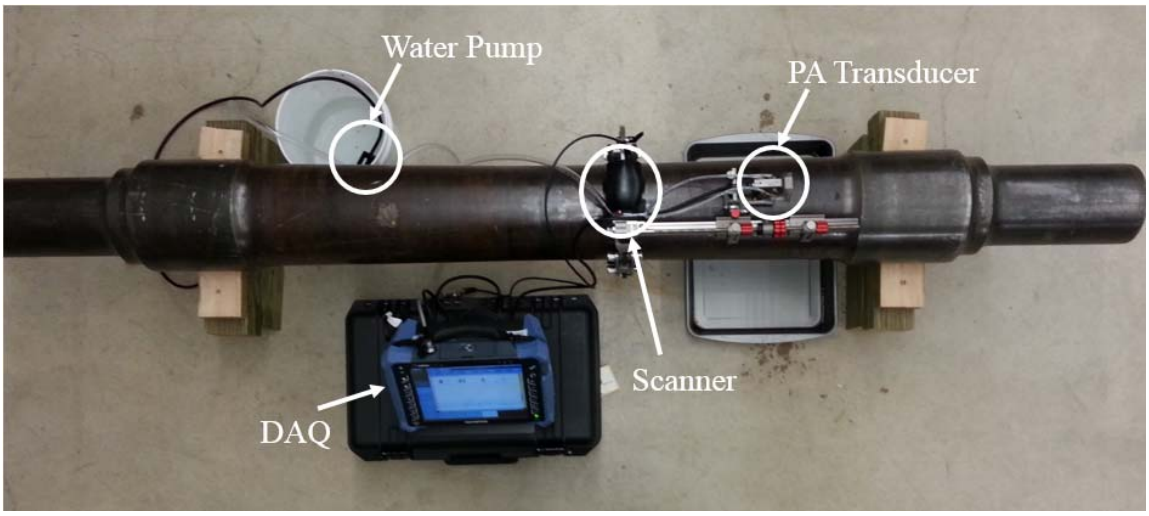

Figure 5.6. Chain scanner with ultrasonic phased array setup

This application is useful when the specimen has limited accessibility, as pulling on the chain link will make the scanner rotate easily. It will be valuable because the chain scanner can inspect each axle underneath a train when it is stopped at the inspection station.

5.3 Experimental Results of Ultrasonic Phased Array

5.3.1 Sensitivity Calibration

Each angled beam has a different amplitude for defects with the same size due to attenuation in the material. The angled beams are normalized to a known reflector through all the angles. After the calibration, all the angles produce similar amplitudes. The calibration is done for the system with a 0.079-in. (2-mm) depth defect.

5.3.2 Automated Detection System Results

The ultrasonic phased array probe and wedge are placed 5 in. (127 mm) away from the wheelseat region, which is about 15 in. (381 mm) away from the axle journal region. The beam angle scans from 30 to 70°. The axle journal region lies on an angle greater than 63°. The angular speed of the motor is set to 1 rad/s. The ultrasonic phased array system can provide A-scan, B-scan, C-scan, and S-scan from the system's own signal processing algorithms. The C-scan result is used to identify a defect. It is a 2D plot that shows a planar view of the test specimen. Figures 5.7 and 5.8 show the results for the intact and cracked axle journal, respectively. As shown in Figure 5.7, the section of the axle can be divided based on the color scheme and beam angle.

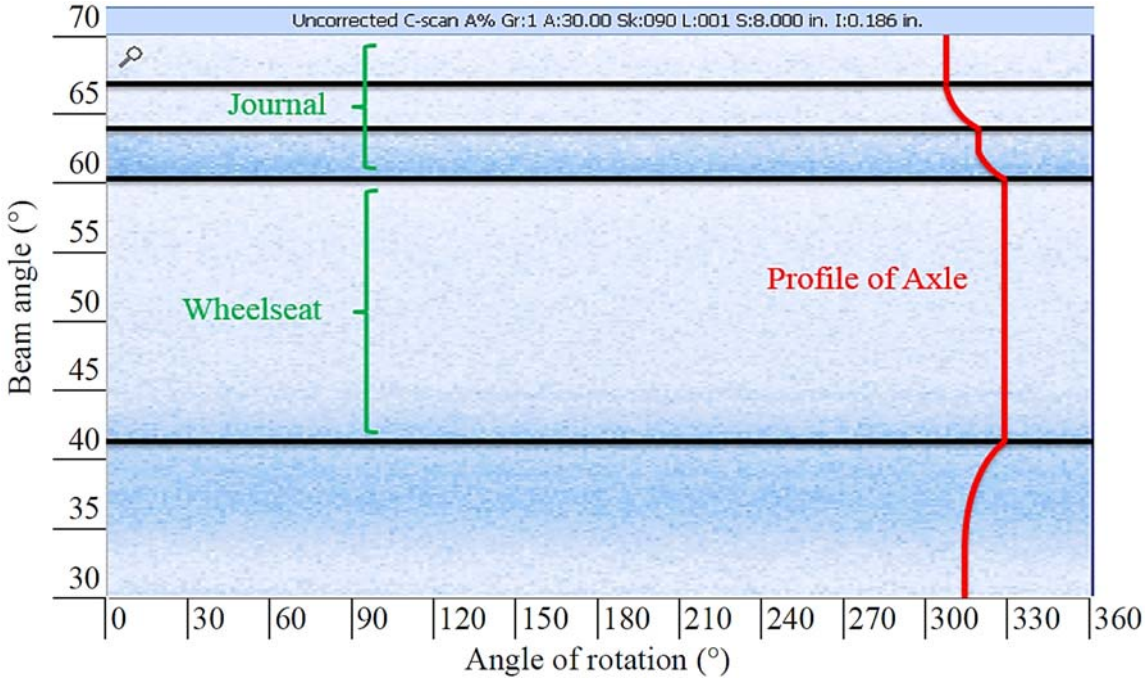

Figure 5.7. C-scan of a healthy axle

Figure 5.8 shows anomalies that can be correlated to the cracks in the axle journal. An ultrasonic testing device in a selected portion on an A-scan display is called a 'gate.' The gate range on the DAQ is set to 1 in. (25.4 mm) because the geometry of the axle is complex.

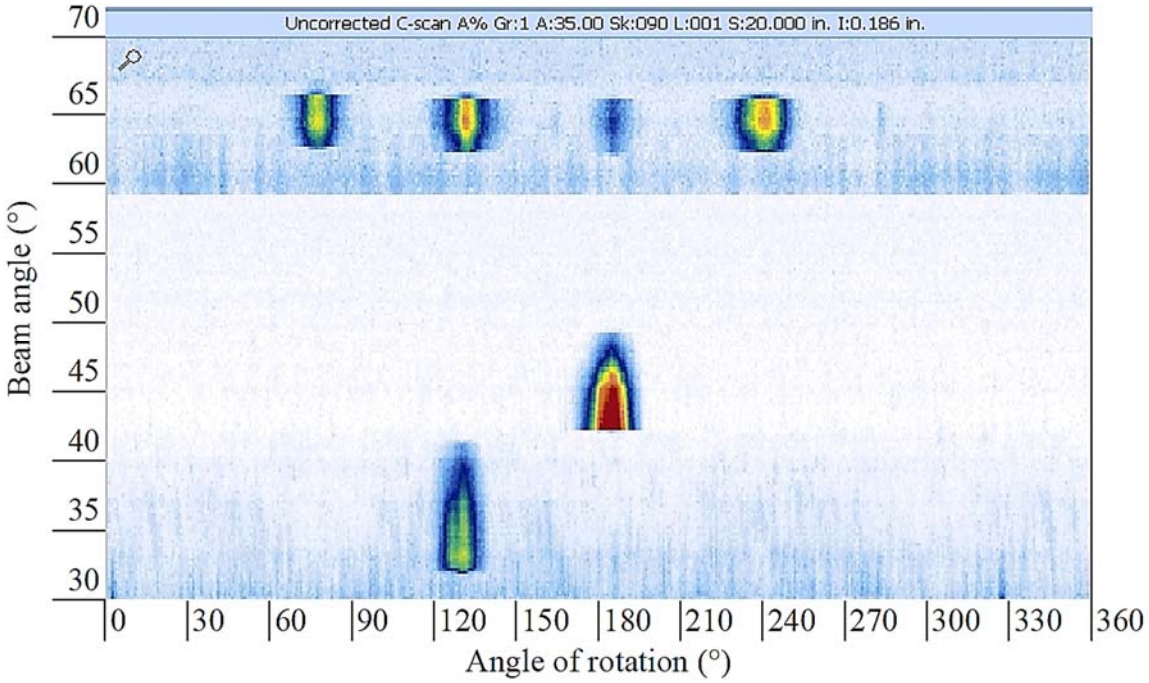

Figure 5.8. C-scan of a cracked axle

The test specimen is carefully investigated using ultrasonic phased array. Any indications from the resulting image such as, red, yellow, green, and dark blue, represent defects. With a proper experimental setup, it takes about 30 seconds (depends on speed of axle rotation) of the inspection time on one side of the axle journal. Based on the specification of the motor used in this experiment, the maximum angular speed is 14.56 rad/s. However, reliable results can be obtained on angular speeds less than 2 rad/s.

5.3.3 Hand-Held Chain Scanner Results

Figures 5.9 and 5.10 show the results of a scan on each side of the axle journal. Based on the crack locations shown in Figure 4.6, all the cracks located at the journal

region are detected. The four indications in Figure 5.9 correspond with crack numbers 1, 2, 3, and 4 in Figure 4.6.

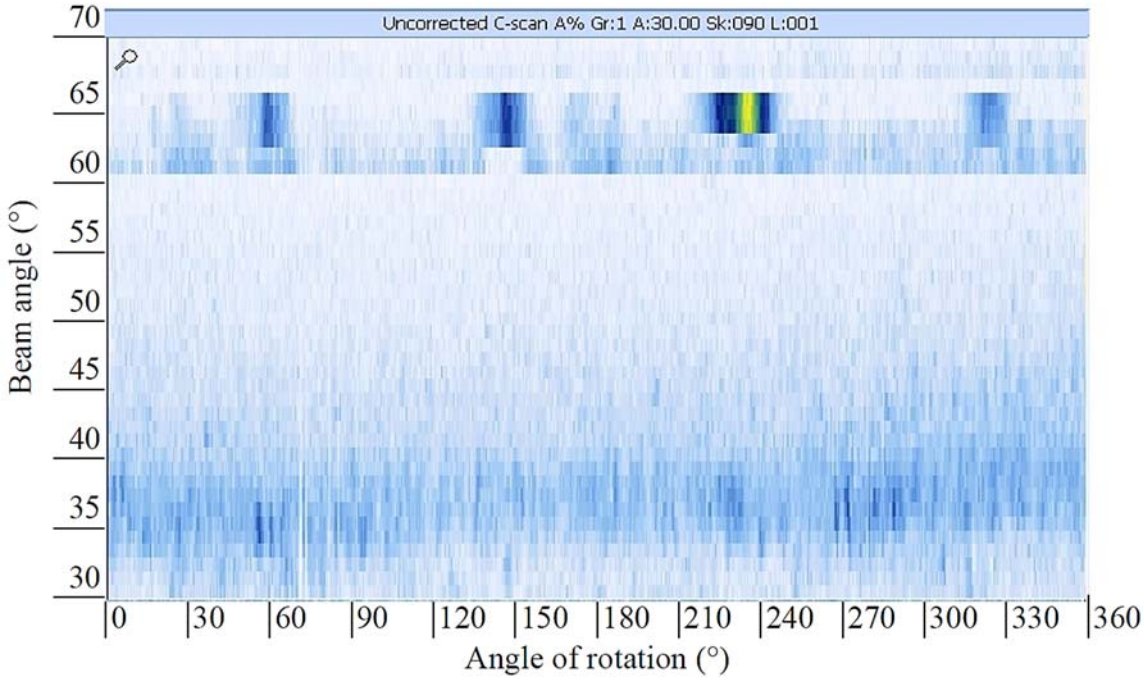

Figure 5.9. C-scan of a cracked axle (left side of journal) using a chain scanner

The six indications in Figure 5.10 match with crack numbers 9, 10, 11, 12, 13, and 14 in Figure 4.6.

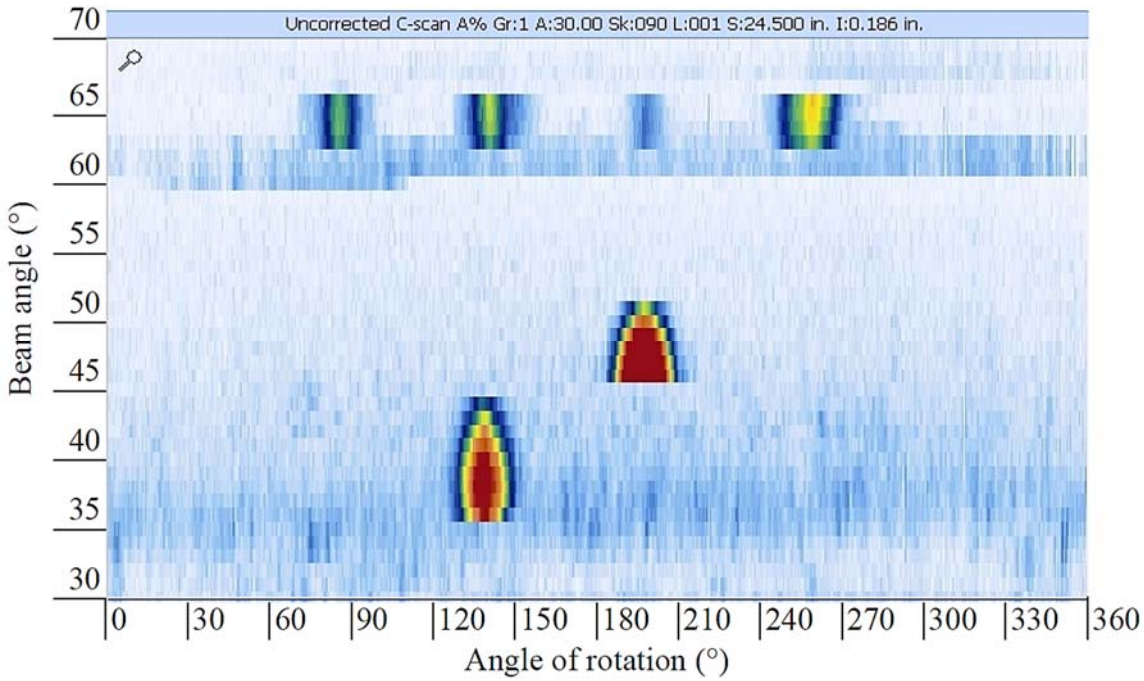

Figure 5.10. C-scan of a cracked axle (right side of journal) using a chain scanner

The installation and scanning time using the scanner takes about 1 minute on one side. The total journal inspection time of an axle is about 2 minutes with a high POD.

5.3.4 Investigation of Axle with Wheels and Bearings

The results obtained in the laboratory are from an axle without wheels and bearings. An axle with wheels and bearings is investigated to validate field conditions. Because the wheels and bearings are press-fitted on the axle, the signals received can be different for the axle with wheels and bearings. Texas A&M Transportation Institute (TTI) has axles with wheels and bearings at the Texas A&M University Riverside Campus. They are scanned with the chain scanner in the field. Figure 5.11 shows the experimental setup.

Figure 5.11. TTI axle scan setup

5.3.4.1 Healthy Axle Result

The axles are carefully investigated using an ultrasonic phased array system. These axles have no known defects, even though they were taken from a train formally in service. It is shown in Figure 5.12 that there is no defect indication on the axle journal region.

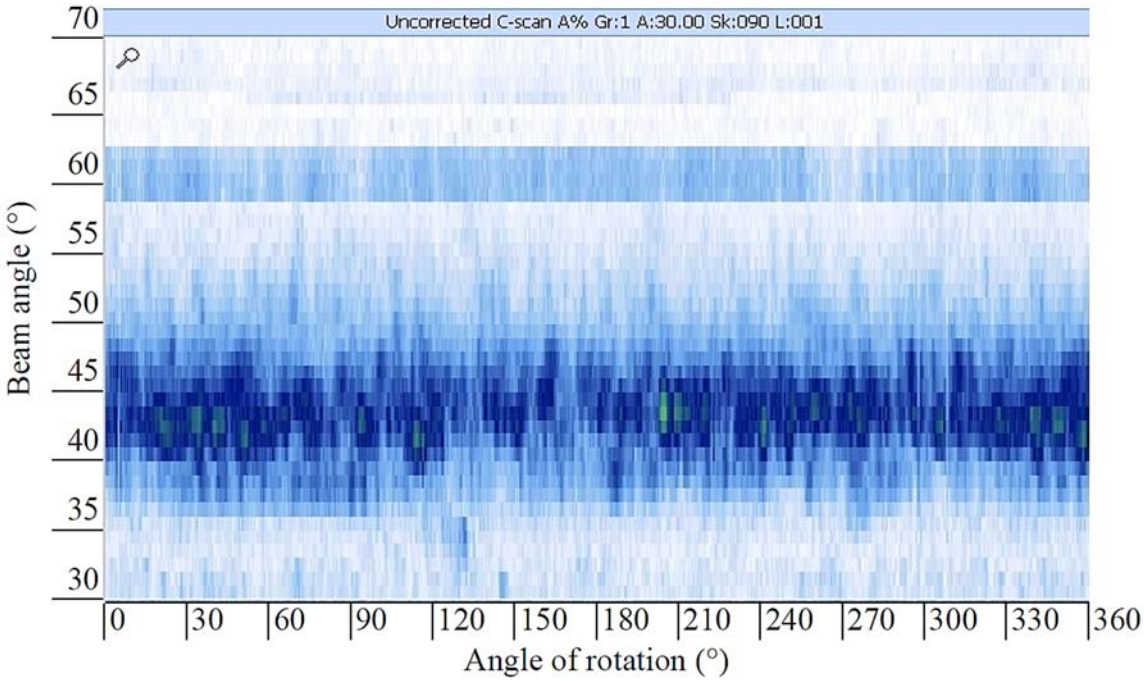

Figure 5.12. C-scan for a healthy axle with wheels and bearings

Therefore, it can be concluded that the placement of wheels and bearings will not affect the resulting signal of an axle journal region.

5.3.4.2 Artificial Crack and Cracked Axle Result

An artificial crack is made in the axle using a 0.04-in. (1-mm)-thick cutting wheel. Shown in Figure 5.13 is the crack. Three different size of cracks were made which has a depth of 0.039, 0.079, and 0.118 in. (1, 2, and 3 mm).

Figure 5.13. Artificial crack using cutting wheel

The result from the C-scan is shown in Figure 5.14. The artificial defects are identified even with the wheel and bearing mounted. It is difficult to detect 0.039-in. (1-mm) crack in the field condition. There is no significant interference on the resulting signals of the axle journal region.

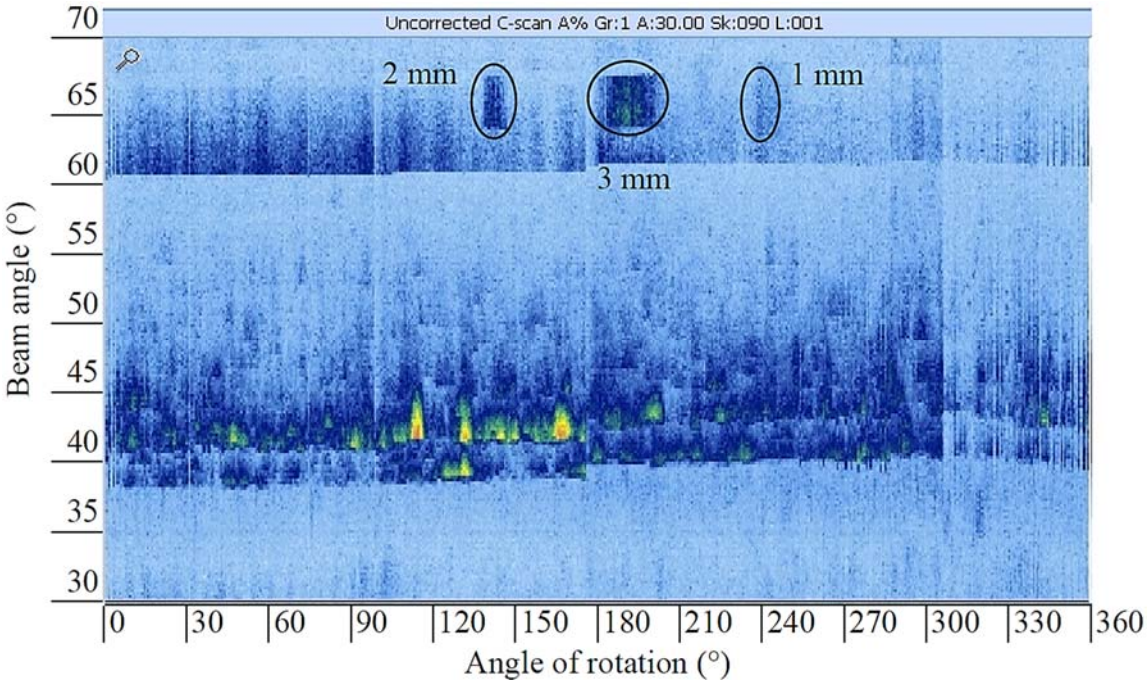

Figure 5.14. C-scan for a cracked axle with wheels and bearings

5.4 Results of Pattern Recognition Algorithm

5.4.1 Results of SVM

The SVM algorithm is described in this section. The RGB color model contains red, green, and blue, which use 8 bits. Each color has integer values from 0 to 255. Red represents a crack in the resulting image while blue is a background color. Red color and blue color data from RGB are used as feature vectors in this data processing among RGB colors. The resulting image contains 400 × 615 pixels after cutting off axes and information from the image. The total data point of the original image is 246,000. Every 10 × 5 pixels are averaged to reduce the total data point. The reduced image contains 4,920 data which are plotted in Figures 5.15 and 5.16.

As shown in Figures 5.15 and 5.16, support vector, hyperplane and data points are drawn in the plots. The points, which are below the line, indicate a defect. Even though Figure 5.15 shows the healthy-condition axle, there are some points below the hyperplane. The green points that are below the line are the trained data-set.

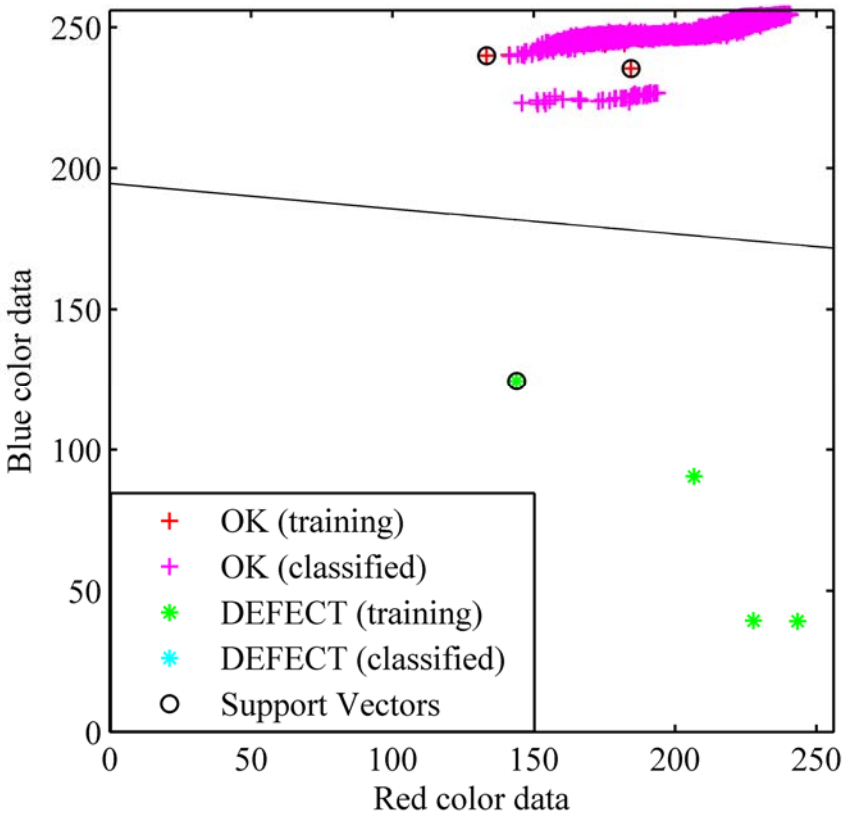

Figure 5.15. SVM results for a healthy axle

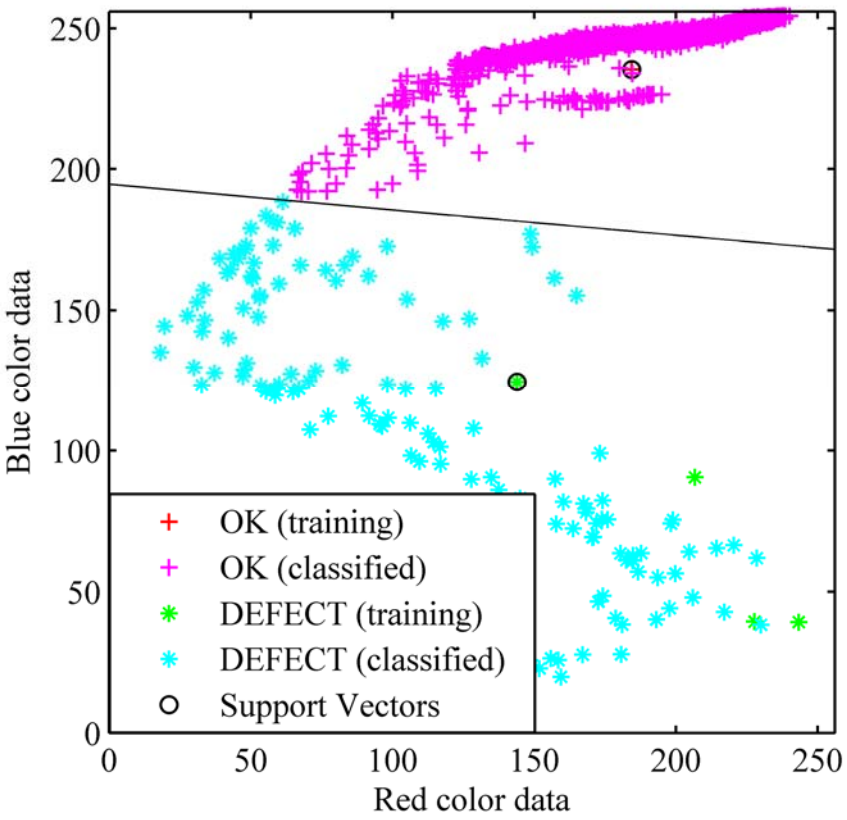

Figure 5.16. SVM results for a cracked axle

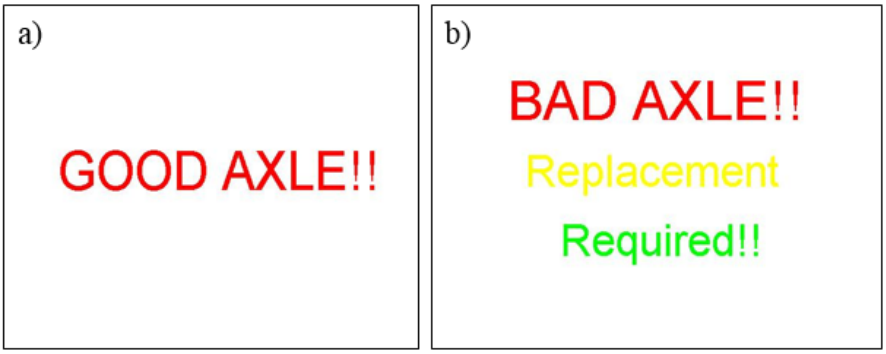

Figure 5.17. Inspection indicators: a) healthy axle and b) cracked axle

After the scanned result images pass through the program, the computer informs the user if an axle is in serviceable condition or not, as shown in Figure 5.17. Such a program will reduce any human involvement on axle inspection.

5.4.2 Signal Processing with Threshold Classifier

Signal processing with threshold classifier is developed based on equations in Chapter 3. The resulting image contains RGB data with the size of 400 × 615 pixels. It is divided by 15 sections for the case that there are multiple flaws. The background color of images that are obtained from the DAQ system is blue. Only blue data are used in this case.

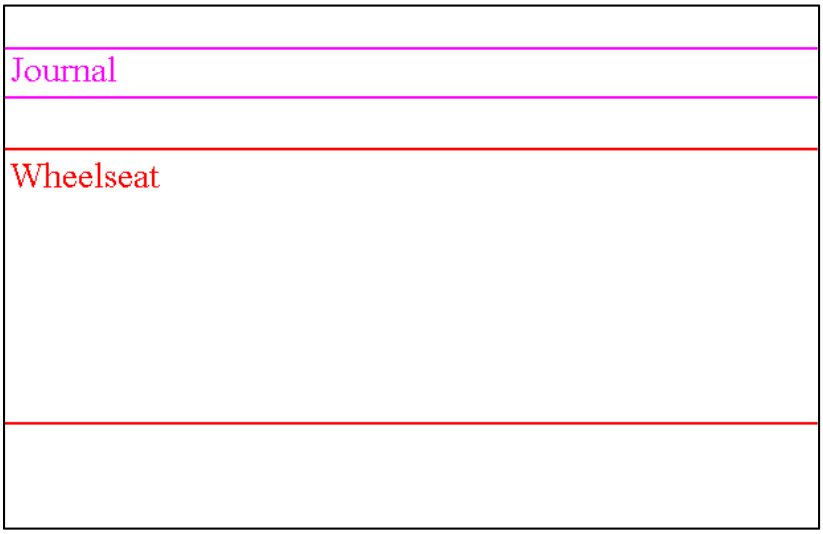

Figure 5.18. Image processing of a healthy axle

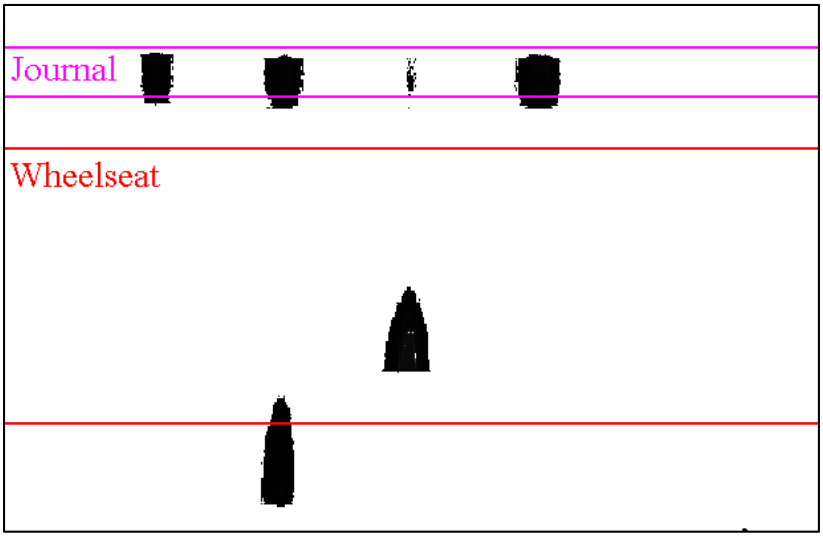

Figure 5.19. Image processing of a cracked axle (right side of journal)

Figure 5.18 shows the healthy-condition axle, there are no indication on the result. Regardless of the size of a defect, the program amplifies any signs of defects based on the threshold, which is 0.04 in. (1 mm), as shown in Figure 5.19. The images go through the threshold classifier and give the indicators shown in Figure 5.17.

5.5 Conclusions

Two main inspection concepts have been developed using ultrasonic phased array in this chapter: 1) automated detection system of a cracked axle journal using the ultrasonic phased array technique, and 2) detection of a cracked axle journal using a chain scanner. The automated detection system is developed for potential applications to a moving train. However, there could be issues of surface preparation and robotic equipment underneath the train. The second concept provides easy and fast inspection because the

probe placement is very flexible. It takes less than 2 minutes to inspect one axle, and the equipment is portable. No disassembly is required for either inspection concept, thus saving time and reducing cost. The threshold classifier does not require a baseline and the computation time is fast. SVM classifies two classes well, but it takes longer computation time that threshold classifier. Based on the defect signals obtained from the experiment, threshold classifier is better method to identify defects.

CHAPTER VI

RAILWAY AXLE JOURNAL INSPECTION USING SURFACE WAVES

6.1 Introduction

The railway axle journal is tested using a surface wave with conventional ultrasonic transducers. The railway axle has a curved surface on the wheelseat and journal region. This experiment will show that the surface wave can be used for axle journal inspection, which contains a complex geometry. An automated detection algorithm is developed for the surface wave using a signal processing technique.

6.2 Experimental Setup

Two conventional ultrasonic transducers are used to detect surface defects in this experiment. The transducers are connected to a pulser-receiver to transmit and then receive the resulting signal. Pulse-echo and pitch-catch modes are employed in this experiment.

6.2.1 Equipment

6.2.1.1 Pulser-Receiver

The Panametrics pulser-receiver (5072PR) is used as a preamplifier. Only the receiving transducer is connected to the pulser-receiver with the following characteristics: 100-Hz pulse repetition frequency (PRF), energy 4, damping 3 (50 ohm), and 59 dB of gain. It has both a low-pass (10 MHz) filter and a high-pass (1 MHz) filter.

6.2.1.2 Oscilloscope

An oscilloscope (Tektronics 3034B) is used to obtain the transmitted and received signals. After 512 samples are obtained, the signals are averaged by the oscilloscope. The data are transferred to a personal computer (PC) via a network using an Ethernet cable, and they are analyzed using MATLAB.

6.2.1.3 Transducer and Wedge

The conventional transducer, Panametrics C403, which has a central frequency of 2.25 MHz, is used in this experiment. The Panametrics wedge ABWX-2001 is attached to the transducer. An incident angle is set to 65° to generate a surface wave on the axle specimen. The wedge delay is 20 μs, and the surface wave speed is 116,811 in/s (2,967 m/s).

6.2.1.4 Function Generator

An Agilent 33220A function generator is used to generate a sine cycle signal. The frequency of the system is set to 2.25 MHz based on the central frequency of the transducers. The input voltage is 1 V peak-to-peak.

6.3 Surface Wave Detection Results

6.3.1 Pulse-Echo Mode

The transducer is placed on the axle body region, which is close to the wheelseat area, as shown in Figure 6.1. The distance from the transducer to the crack on the axle

journal is 10 in. (254 mm). The pulse-echo mode is performed on axle journals with and without defects for comparison. Figure 6.2 shows the result of the received signal for the axles with and without defects.

Figure 6.1. Experimental setup of pulse-echo mode [10 in. (254 mm) apart from the transducer to the defect]

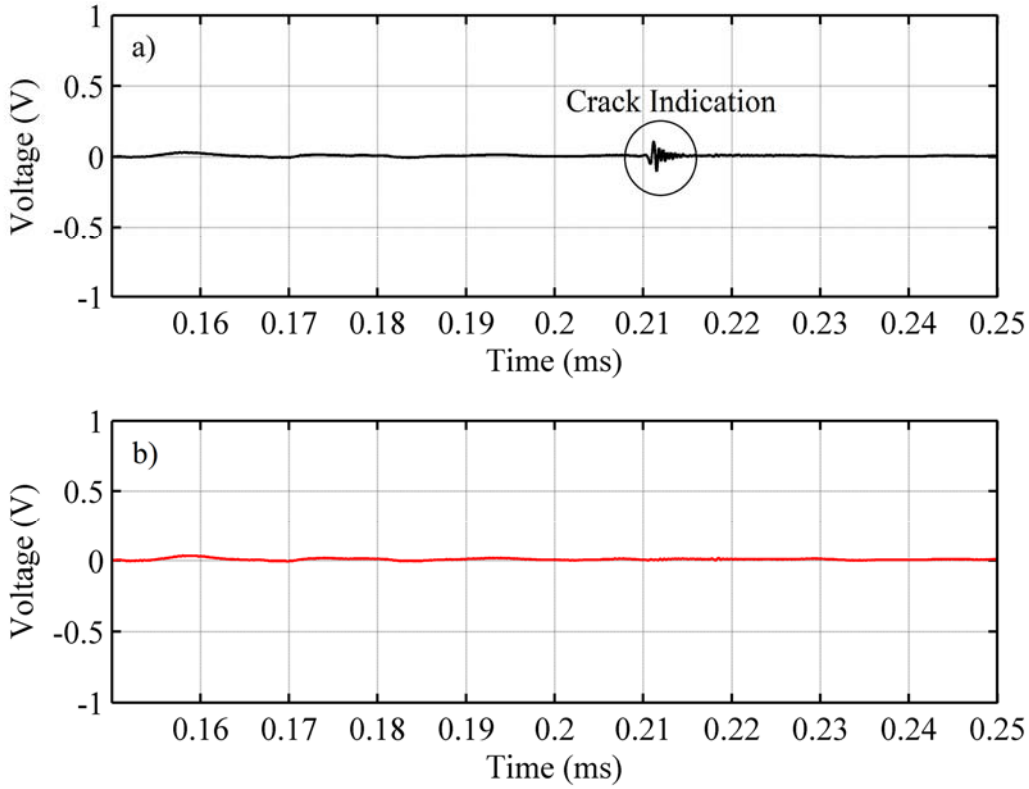

Figure 6.2. Crack detection in pulse-echo mode: a) cracked region and b) uncracked region

The experimental arrival time for a total wave propagation length of 20 in. (508 mm) (back and forth) is 0.210 ms for Figure 6.2a, and the theoretical arrival time with wedge delay is 0.211 ms. There is no reflected response shown in Figure 6.2b because there is no defect.

6.3.2 Pitch-Catch Mode

There are three different locations of transducer placement on pitch-catch mode:

Mode 1: transducers face each other, as shown in Figure 6.3

Mode 2: transducers are placed on one side of the same line, as shown in Figure 6.5

Mode 3: transducers are placed on the same side with a tilted angle, as shown in Figure 6.7

Figure 6.3. Transducers placed facing each other [20.5 in. (520.7 mm) apart from the transmitting transducer to receiving transducer]

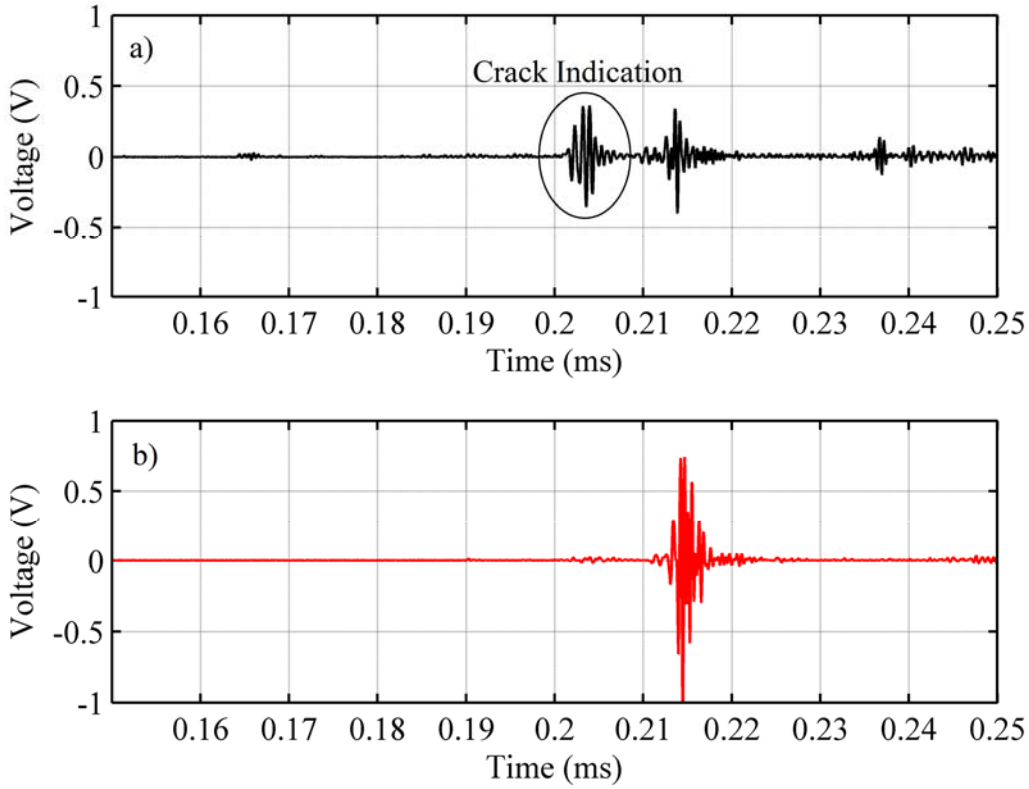

Figure 6.4. Crack detection in pitch-catch mode 1: a) cracked region and b) uncracked region

Figure 6.3 shows pitch-catch mode 1. As shown in Figure 6.4, the experimental and theoretical wave propagation time for a distance of 20.5 in. (520.7 mm) is 0.211 ms and 0.216 ms, respectively. The defect on the journal is located 19 in. (482.6 mm) from the transmitting transducer. The experimental arrival time for 19 in. (482.6 mm) is 0.201 ms, and the theoretical arrival time is 0.203 ms.

For pitch-catch mode 2, the transducers are facing the same side 5 in. (127 mm) apart, as shown in Figure 6.5. The one on the left is a transmitting transducer, and the one on the right is a receiving transducer.

Figure 6.5. Transducers placed on one side on the same line

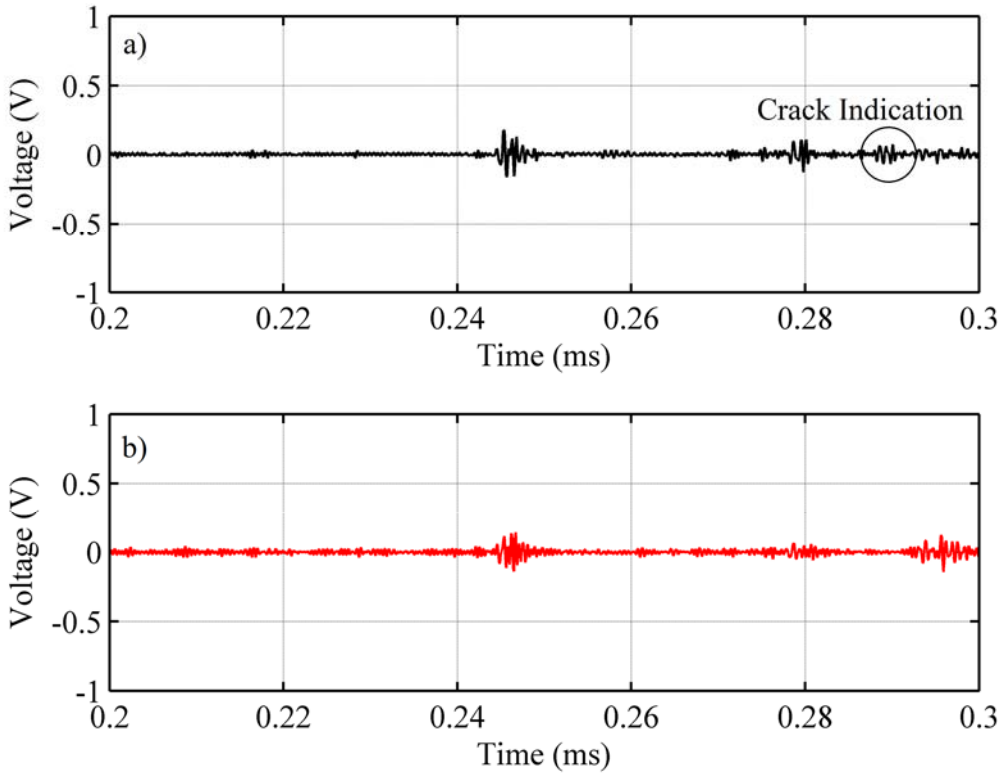

Figure 6.6. Crack detection in pitch-catch mode 2: a) cracked region and b) uncracked region

As shown in Figure 6.6, the experimental arrival time for 28 in. (711.2 mm) (back and forth), which is twice the wave propagation distance from transducers to the defect location on the axle journal, is 0.288 ms, and the theoretical arrival time is 0.280 ms. It is expected that high energy loss occurred when the wave pulse passed the receiver.

For pitch-catch mode 3, the transducers are placed 12.2 in. (309.8 mm) from the defect. The angle between two transducers is 14°, as shown in Figure 6.7.

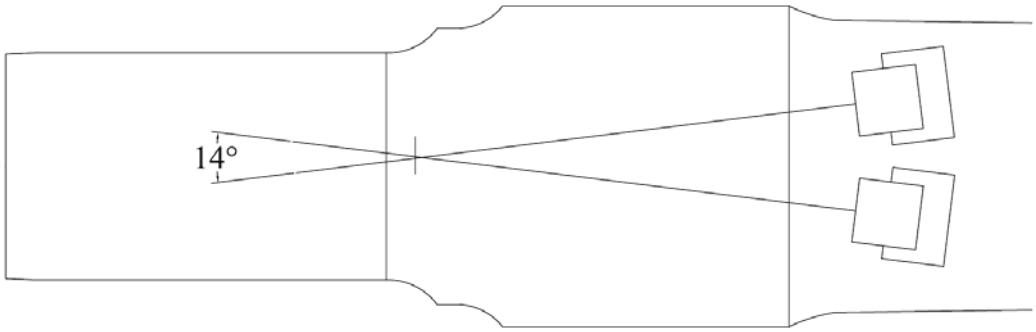

Figure 6.7. Transducers placed on the side with the tilted angle

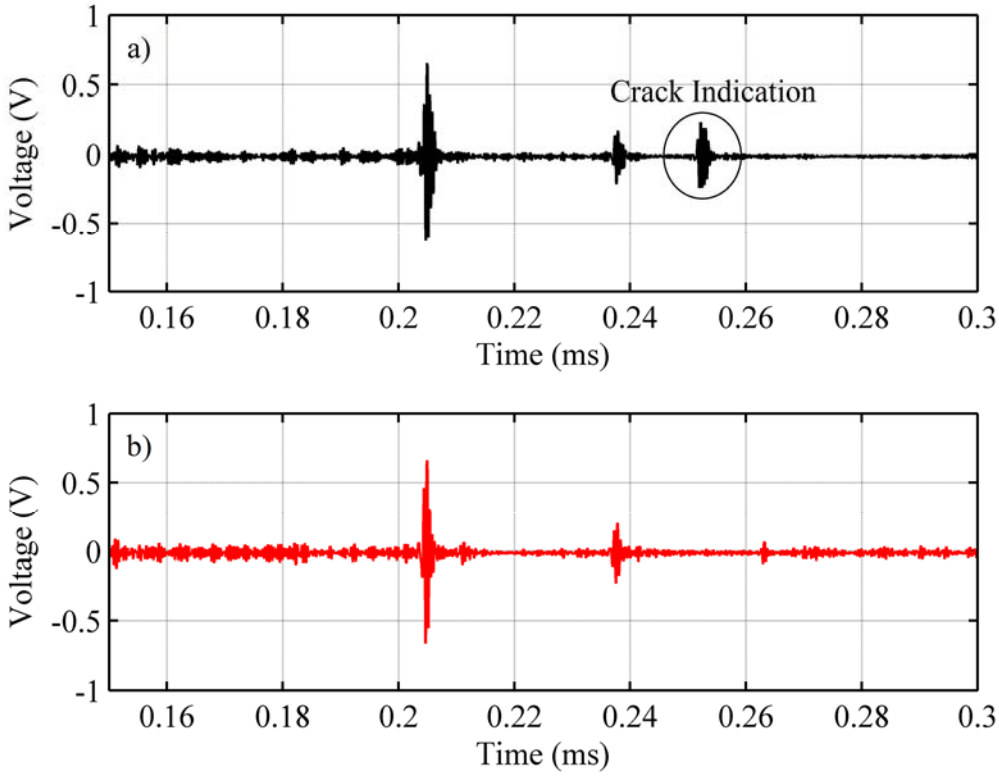

Figure 6.8. Crack detection in pitch-catch mode 3: a) cracked region and b) uncracked region

As shown in Figure 6.8, the experimental arrival time for a distance of 24.4 in. (619.76 mm) (back and forth), which is twice the distance to the defect location on the axle journal, is 0.251 ms, and the theoretical arrival time is 0.249 ms.

The surface wave detection on axle with wheels and bearings is demonstrated with pitch-catch mode 3. The transducers are placed 11 in. (279.4 mm) from the artificial defect. Two geometry echo signals are expected at 1.625 and 9.625 in. (41.3 and 224.5 mm) from the transducers.

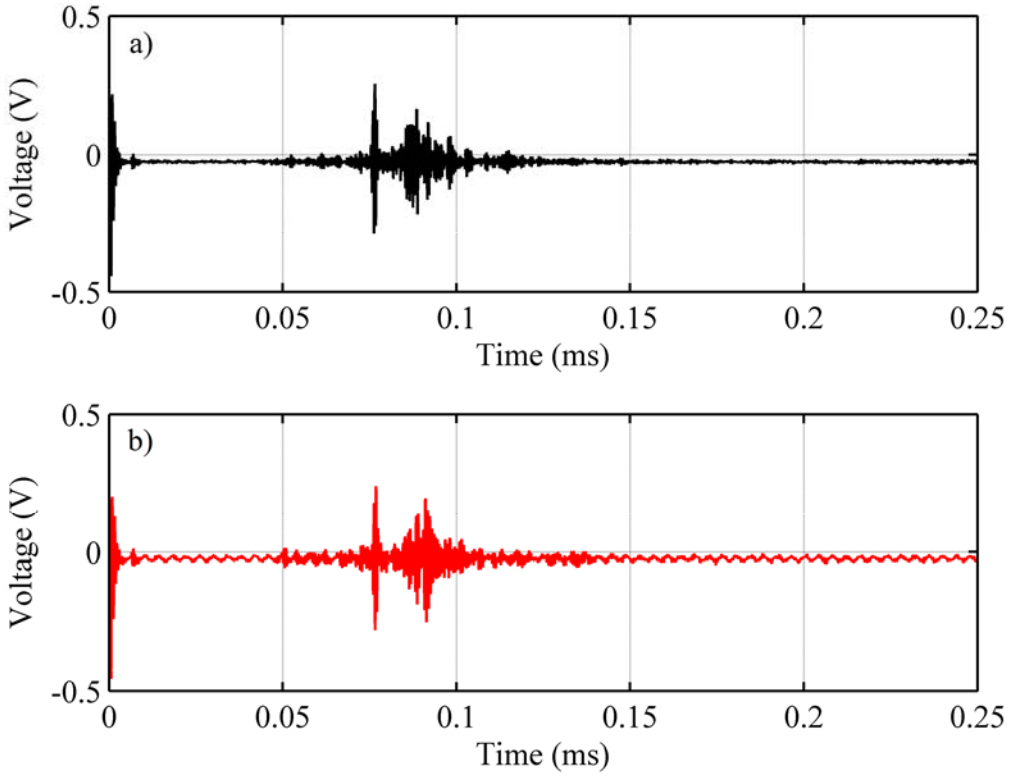

Figure 6.9. Crack detection in pitch-catch mode 3 on axle with wheels and bearings: a) cracked region and b) uncracked region

The theoretical arrival time for a wave propagation distance of 22 in. (558.8 mm) (back and forth), which is twice the distance to the defect location on the axle journal, is 0.228 ms. However, as shown in Figure 6.9, no energy reflection is detected. In addition, the geometry echo signal, which is expected at 0.204 ms, is not detected. Surface wave inspection technique is difficult to use when wheels and bearings are attached on axle.

6.4 Complex Geometry of a Railway Axle

The axle journal and wheelseat area have complex geometries. The surface wave is guided by its boundaries, which allows it to propagate a long distance with little energy loss. As shown in Figure 6.10, the transition region has an angle up to 32°.

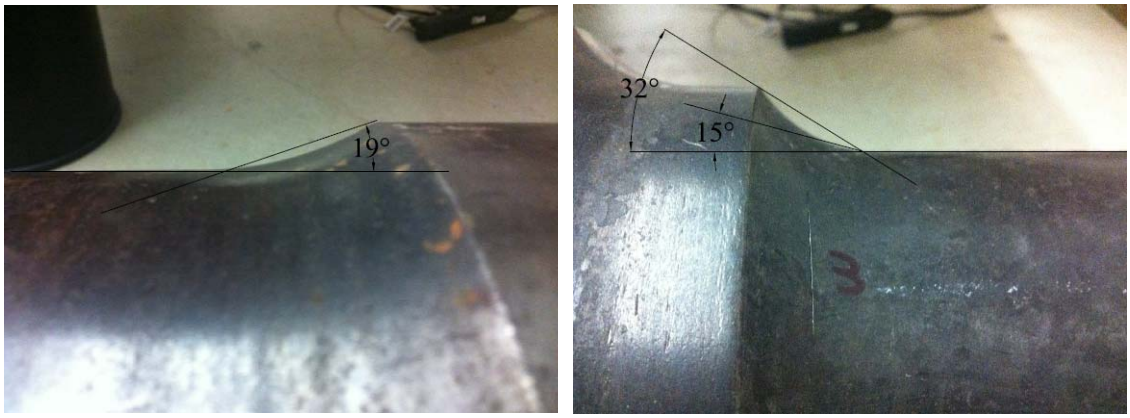

Figure 6.10. Complex geometry of the axle journal

Each reflected signal from the previous results drives the energy loss of the original ultrasonic wave. The surface wave detection experiment reveals that it can overcome the complex geometry of the wheelseat region of an axle and detect cracks on the axle journal region.

6.5 Results of Signal Processing Technique of Surface Wave

Automated detection is performed by the signal processing technique. The result, shown in Figure 6.8, is an example of the signal processing procedure. The damage index method is used to identify defects. The root-mean-square values are computed as

$$x_{\text{rms}} = \sqrt{\frac{(x_1^2 + \cdots + x_n^2)}{n}}. \tag{6.1}$$

The absolute difference values are computed between raw data and root-mean-square

$$x_{\text{difference}} = |x_{\text{raw}} - x_{\text{rms}}|. \tag{6.2}$$

The difference ratio values are calculated with the following equation

$$x_{\text{ratio}} = \frac{x_{\text{difference}}}{x_{\text{raw}}}. \tag{6.3}$$

To avoid singularity, the shifted difference ratio values are used to find defects

$$\text{Damage Index} = \frac{x_{\text{difference}} + 1}{x_{\text{raw}} + 1}. \tag{6.4}$$

The shifted damage index values are classified based on a threshold value of 1.5.

The procedure requires two input data: the distance from the transmitting transducer to journal region and the surface wave speed of the specimen.

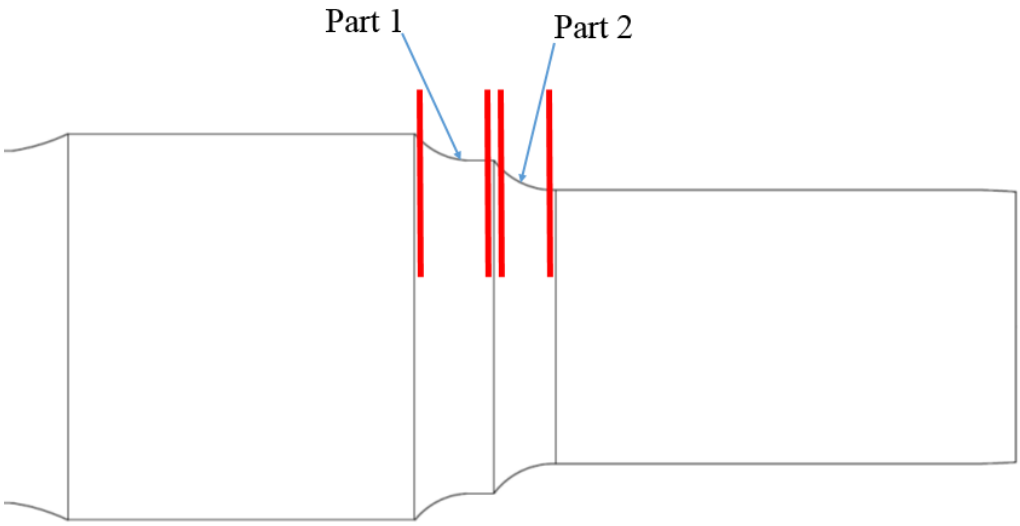

Figure 6.11. Geometry detail of a railway axle journal

As shown in Figure 6.11, the journal region is defined as Part 1 and Part 2. Each part is separated from the original A-scan results. The reason for using part separation is to avoid the geometry signals for automation purposes. Figure 6.8a is re-drawn in Figure 6.12 for each part. A defect is represented only in Part 2 of the cracked case in Figure 6.8a.

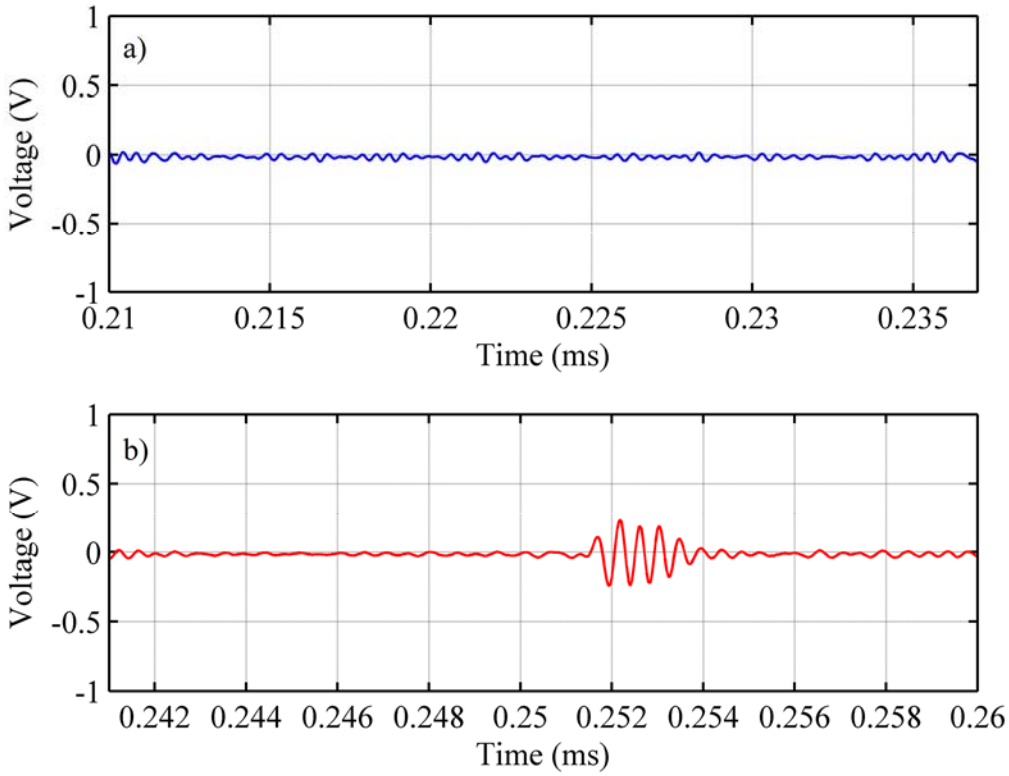

Figure 6.12. Separated signal: a and b correspond to Figure 6.8a

Figure 6.12 represents individual cases of Parts 1 and 2. Figures 6.12a and 6.12b are taken from Figure 6.8a. As expected, Figure 6.12b obtains the crack information. Equations (6.1) to (6.4) are used to compute the root-mean-square, difference ratio, and damage index.

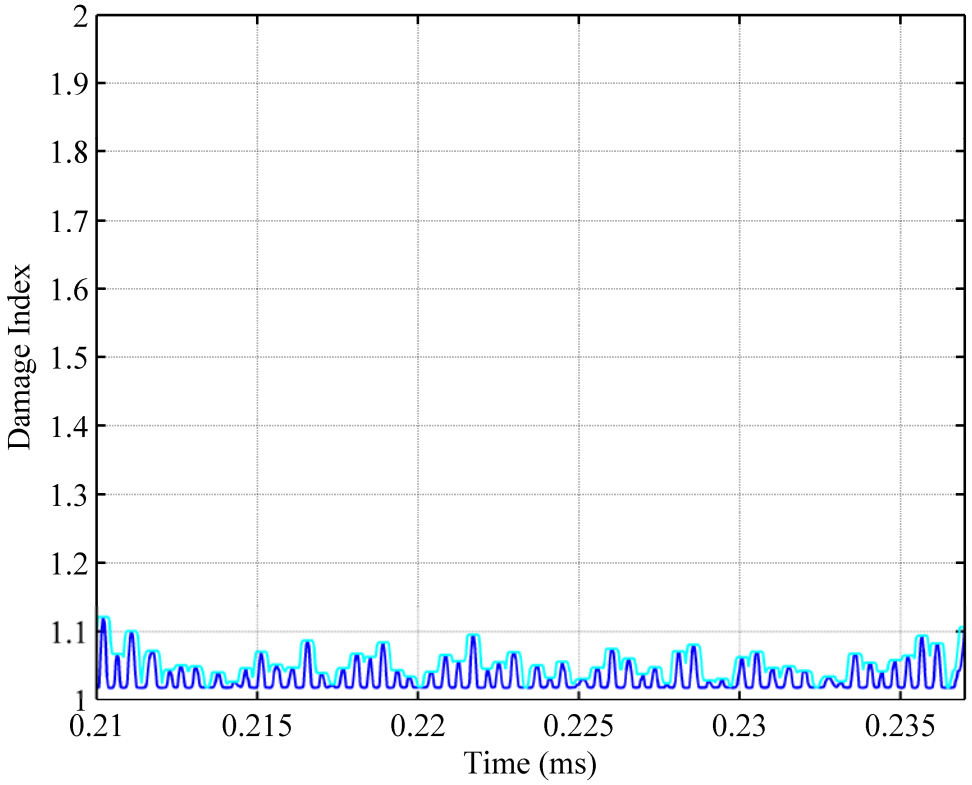

Figure 6.13. Damage index with envelope plots of the uncracked case

The damage index is calculated and plotted in Figures 6.13 and 6.14. Figure 6.13 shows the non-cracked case. The damage index numbers are located near 1 to avoid singularity, as represented in Equation (6.4). The envelope lies in the range between 1 and 1.2 and contains noise signal.

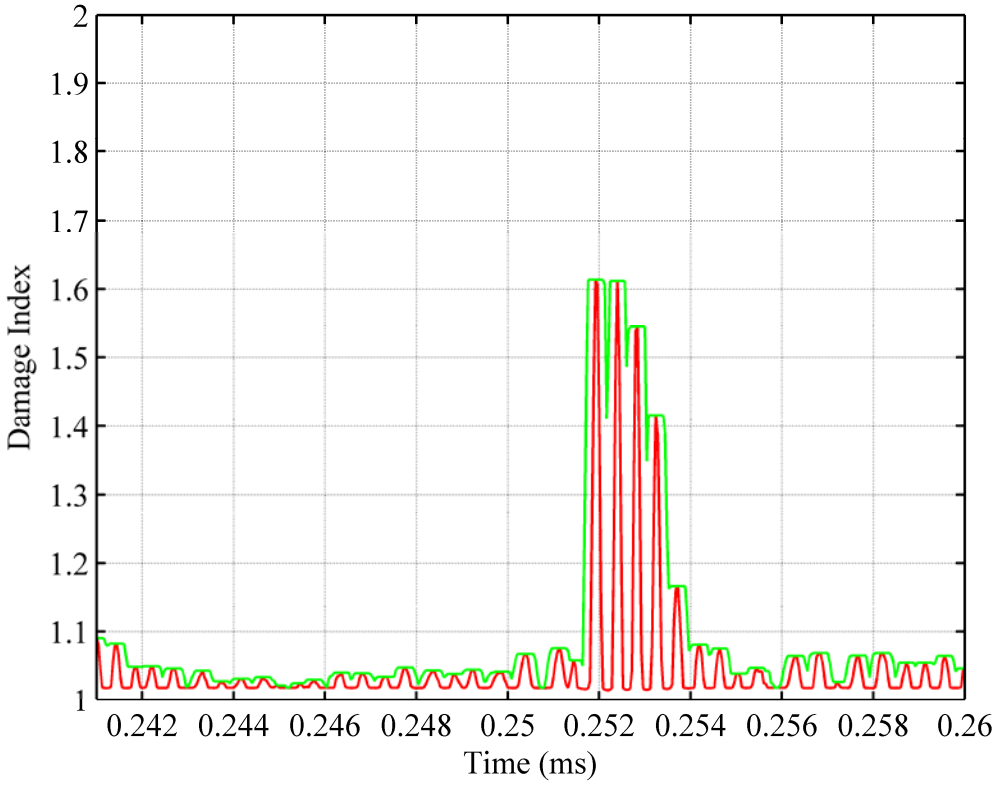

Figure 6.14. Damage index with envelope plots of the cracked case

Figure 6.14 represents the cracked case. The damage index curve has five peaks because of the sine wave signal. The first peak indicates the arrival time of the signal, which is 0.252 ms. The location of the defect is 12.4 in. (314.4 mm) from the ultrasonic transmitter for this case.

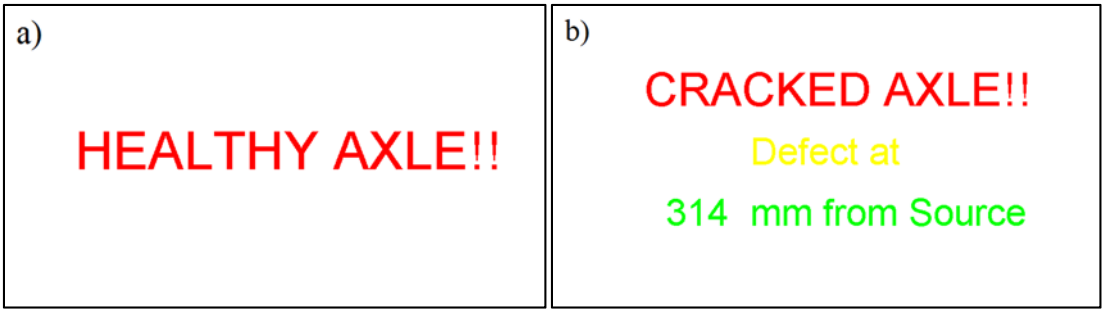

Figure 6.15. Inspection indicator: a) healthy axle and b) cracked axle

As shown in Figure 6.15, the developed program identifies the cracked and uncracked axle based on the damage index value. In the absence of a crack, the damage index value is between 1 and 1.2. When the damage index is greater than 1.2, there is a defect.

6.6 Conclusions

The demonstrations performed in this chapter prove that surface waves can propagate along complex geometries of the railway axle. One-side inspection is required to inspect axle journals using a surface wave without disassembly. It is suggested to use pulse-echo mode (Figure 6.1) or pitch-catch mode 3 (Figure 6.7) for one-side axle journal inspection. The inspection technique can be improved by replacing contact transducers with air-coupled transducers or magnetostrictive sensors for surface wave inspection.

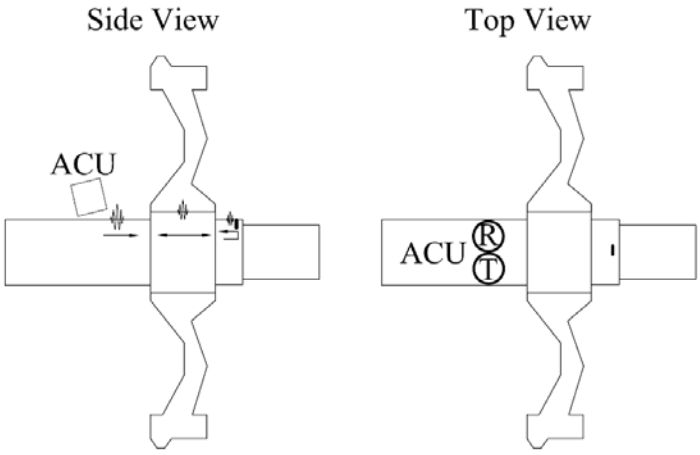

Figure 6.16. Examination of an axle using air-coupled ultrasonic

As shown in Figure 6.16, two air-coupled ultrasonic transducers are used to generate (transmitter) and detect (receiver) ultrasonic bursts on the axle. Surface waves will be used for diagnostic purposes. A higher voltage is required to overcome the high acoustic mismatch between air and steel. When the ultrasonic wave interacts with a discontinuity, such as a fatigue crack, a part of the incident wave will be reflected. The reflected wave is identified by the receiver. If the amplitude of the reflected signal is above a threshold value using the developed signal processing technique, it is assumed that a defect is presented. A DAQ receives and stores the result signals to identify and locate a defect.

CHAPTER VII

AIR-COUPLED ULTRASONIC SYSTEM

7.1 Introduction

In this chapter air-coupled ultrasonic techniques are demonstrated on concrete, aluminum, steel plate, and LDPE plate. The goal of these experiments is to perform the inspection in a non-contact manner on various materials. Given the state of current technology, there are various air-coupled ultrasonic transducers, but they only work well with non-metallic materials or thin metal plates using a through-transmission technique because of the high impedance mismatch between air and metal. Three different experimental concepts are demonstrated: 1) line-source air-coupled ultrasonic array sensors in through-transmission mode, 2) point-source air-coupled ultrasonic generation using a Rayleigh wave, and 3) laser array detector on steel plate. The result of this research will contribute to the field of non-contact railway axle inspection and ultrasonic NDT.

7.2 Experimental Setup on Air-coupled Ultrasonic

Figure 7.1 shows the overall experimental setup of the air-coupled ultrasonic array system. Three different methods of receiving signals are used: the contact transducer, microphone sensor, and LDV. The measurements are taken individually on the symmetric axis of the ultrasonic source.

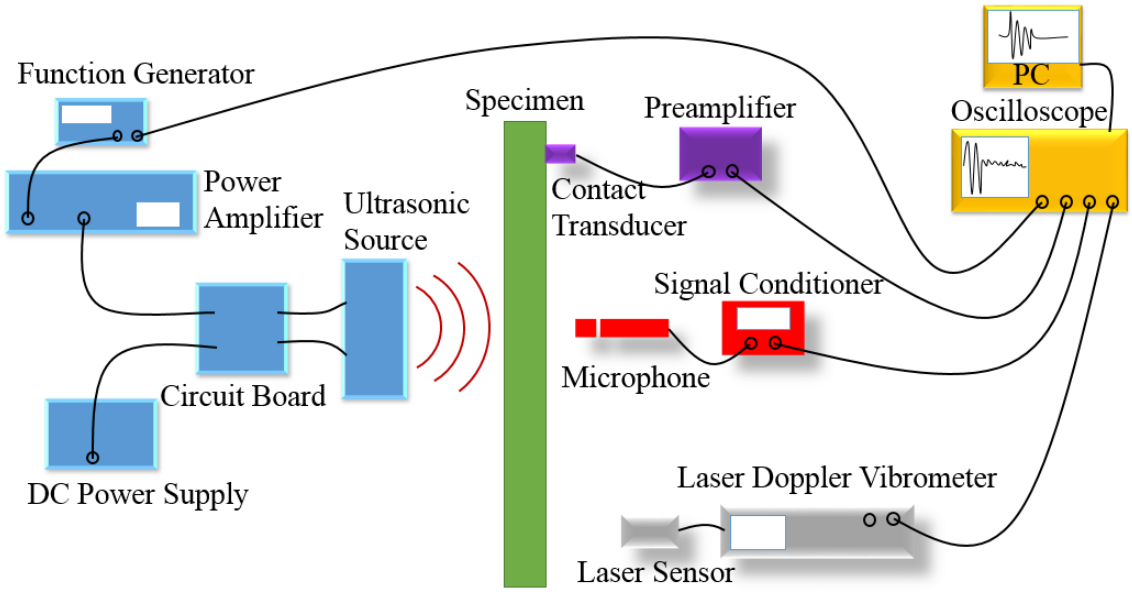

Figure 7.1. Experimental setup of the air-coupled ultrasonic system

7.2.1 Experimental Equipment

7.2.1.1 Test Specimen

The concrete mortars, aluminum sheet, and LDPE are tested to verify the effectiveness of the 20-array air-coupled transducer. The concrete mortar has dimensions of 12 × 12 in. (305 × 305 mm) and two different thicknesses of 0.75 and 1.5 in. (19 and 38 mm). The aluminum sheet has dimensions of 12 × 12 × 0.02 in. (305 × 305 × 0.5 mm). The LDPE plate has dimensions of 24 × 12 × 1.62 in. (607 × 305.5 × 41.4 mm). The typical P-wave speed of aluminum is 248,819 in/s (6,320 m/s). The P-wave speed of LDPE and concrete mortar are 81,969 and 127,874 in/s (2,082 and 3,248 m/s), respectively. If the concrete mortar mixed according to the manufacturer's specification, a Poisson's ratio and a modulus of elasticity are 0.21 and 3,889.9 ksi (26.82 GPa), respectively. The wave

speeds are measured and averaged 10 times using two digital wave B1025 transducers. The specimens are tested using the through-transmission method.

7.2.1.2 Air-coupled 20-Array Transducer

The air-coupled 20-array transducer was designed by Blum (2003), as shown in Figure 7.2. The transducer for this study was manufactured using the guidelines specified by Blum (2003). The 20-array air-coupled sources are built up with Polaroid 600 Series electrostatic transducers, producing a maximum SPL of 150.76 dB. The central frequency of transducer is 50 kHz. The best results are obtained in the frequency range of 50 to 100 kHz.

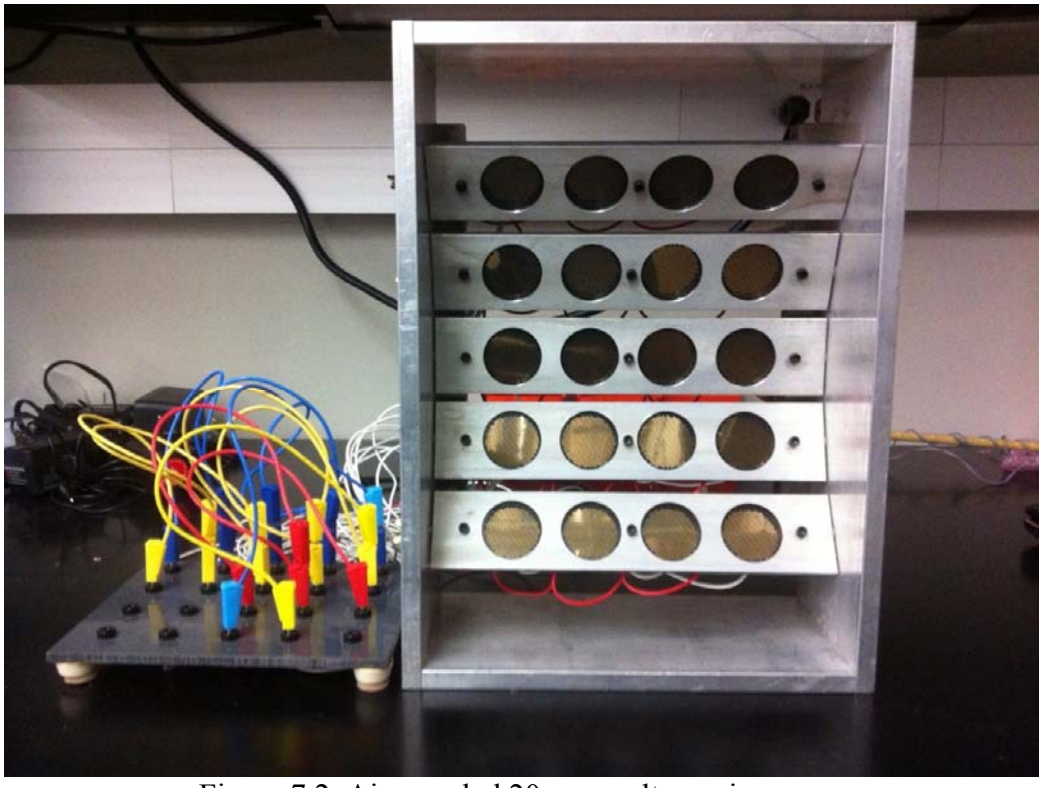

Figure 7.2. Air-coupled 20-array ultrasonic source

7.2.1.3 Power Amplifier

The E&I 240L broadband power amplifier is employed, which is capable of operating in a frequency range of 10 kHz to 12 MHz. It provides a saturated RF power output of 90 W in the frequency range.

7.2.1.4 Direct Current (DC) Power Supply

As shown in Figure 7.3, the transmitting circuit requires a bias voltage and an alternating current (AC) input voltage. EMCO high voltage power supply provides the bias voltage, which can produce up to 500 V. A bias voltage of 150 V is applied to the circuit in this experiment. It takes some time to stabilize the voltage to obtain a constant DC power from the supply. Figure 7.4 demonstrates how the DC power supply affects the overall received pressure amplitude. When AC and DC power supplies operate simultaneously, they provide eight times greater amplification than only the AC power amplifier is used. Resistor

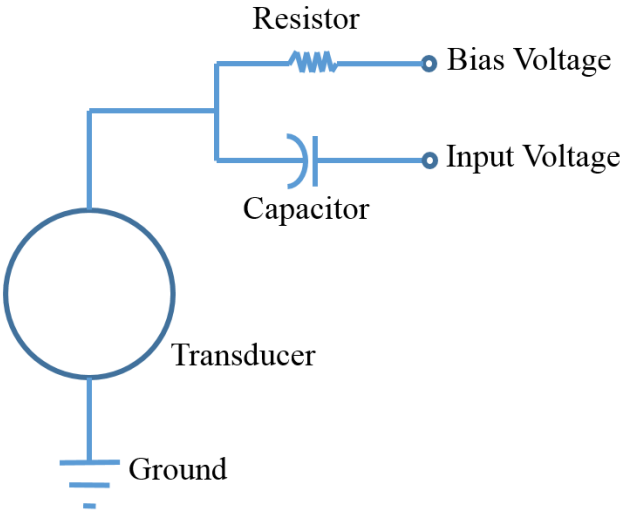

Figure 7.3. Transmitting circuit (Blum 2003)

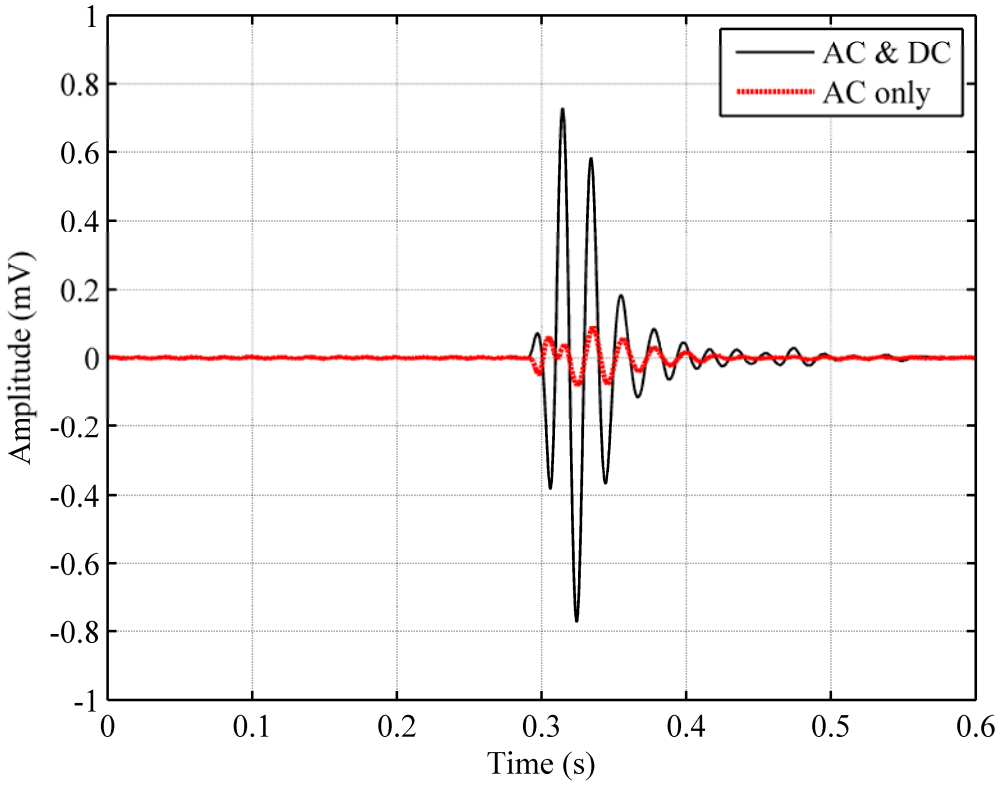

Figure 7.4. Comparison of received amplitude with and without DC power supply.

7.2.1.5 Function Generator

An Agilent 33220A function generator is used to generate a sine cycle signal. Blum (2003) recommends that the excitation frequency of the air-coupled system be 80 kHz for LDPE and 60 kHz for aluminum. The 1 V peak-to-peak is used with one cycle of bursts.

7.2.1.6 Receiving Transducers

A piezoelectric broadband transducer is used for acoustic emission measurements. The digital wave B1025 transducer has a small effective surface area of 8-mm diameter and a frequency range of 50 kHz to 2 MHz.

7.2.1.7 Microphone Sensors

The PCB Piezotronics 377A01 precision prepolarized condenser microphone is used for signal reception in air. Its characteristics include ¼-in. diameter, free-field type, sensitivity of 4 mV/Pa at 250 Hz, and frequency range of 4 Hz to 100 kHz at $\pm$2 dB. The microphone is directly connected to a PCB Piezotronics 426B03 microphone preamplifier. The PCB Piezotronics 426B03 is an ICP microphone preamplifier of ¼-in. diameter, attenuation of –0.08 dB, and frequency range of 3 Hz to 126 kHz.

7.2.1.8 Signal Conditioner

The preamplifier is connected to the PCB Piezotronics 480E09 ICP sensor signal conditioner. The signal conditioner can amplify the voltage gain by 1, 10, and 100.

7.2.1.9 Pulser-Receiver

The Panametrics pulser-receiver (5072PR) is employed as a preamplifier. Only the receiving transducer is connected to the pulser-receiver with 59 dB of gain. It has a low-pass (10-MHz) and high-pass (1-MHz) filter. Because the central frequencies of 80 kHz and 60 kHz are used for this experiment, the high-pass filter is off, and the low-pass filter is set to 10 MHz.

7.2.1.10 Oscilloscope

An oscilloscope (Tektronics 3034B) is used to record the transmitted and received signals. After 512 samples are obtained, the signals are averaged by the oscilloscope. The data are transferred to a PC via a network using an Ethernet cable, and they are analyzed using MATLAB.

7.2.1.11 Slit-Plate

Blum's (2003) design operates the 20-array sensors with a slit plate to shield the side lobes. He recommends using the spacing of the slit plate as a wavelength of the ultrasonic signal. For example, the wavelength of an 80-kHz excitation frequency is 0.167 in. (4.25 mm). The width of the slit is set to 0.167 in. (4.25 mm) to reduce the side lobes based on Blum's (2003) recommendations.

7.2.1.12 LDV

The LDV system contains a Polytec OFV 505 standard sensor head and an OFV 5000 vibrometer controller. The velocity decoder VD-09 is used, which has an upper frequency limit of 2.5 MHz. The concept of the system is to observe the surface particle's velocity changes. A complete review of LDV can be found in Hurlebaus (2002) and in Hurlebaus and Jacobs (2006).

7.2.2 Attenuation in Air

The attenuation coefficient of air, α_{air}, at 20 °C is 4.17 dB/(MHz·in) [1.64 dB/(MHz·cm)] (Jakevicius & Demcenko 2008). The experiment for the attenuation is performed with an excitation frequency of 50 kHz. The adjusted attenuation coefficient is 0.208 dB/in. (0.082 dB/cm), while Jakevicius and Demcenko (2008) recommended to use the attenuation coefficient of 0.132 dB/in. (0.052 dB/cm). One Polaroid 600 air-coupled sensor is used to measure the attenuation in air at the propagation distances of 3.9, 5.9, 7.9, 9.8, 11.8, 13.8, and 15.7 in. (10, 15, 20, 25, 30, 35, and 40 cm). Figure 7.5 shows the time domain signal obtained using a microphone sensor.

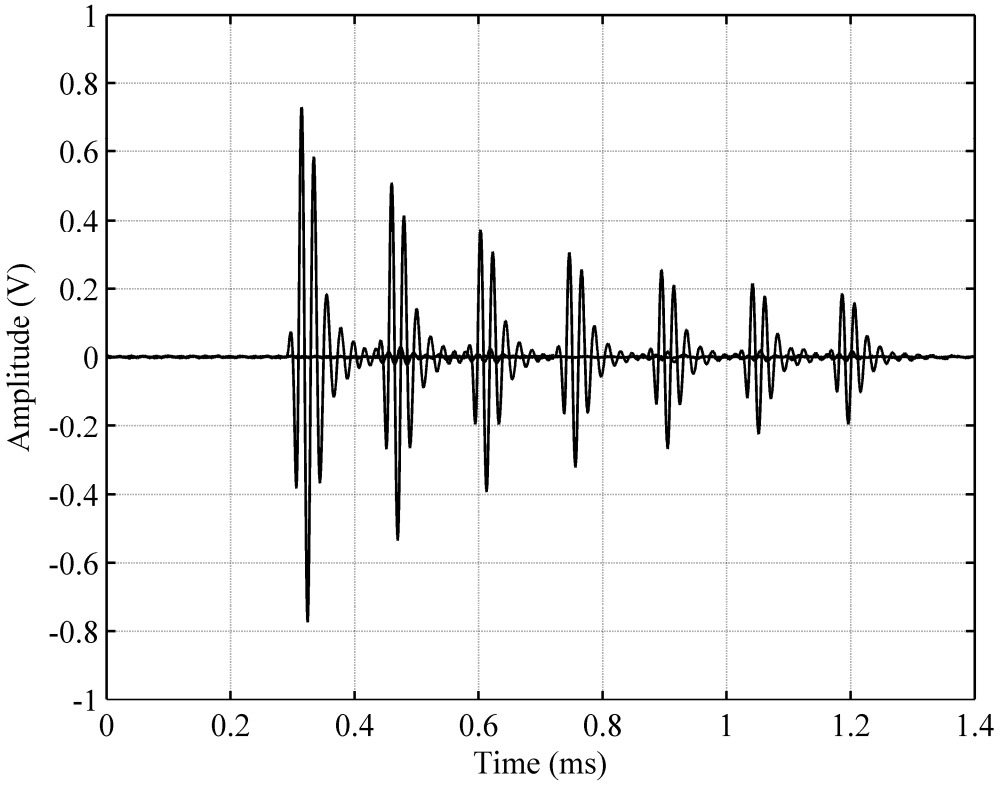

Figure 7.5. Attenuation curve of one air-coupled ultrasonic sensor with 50 kHz

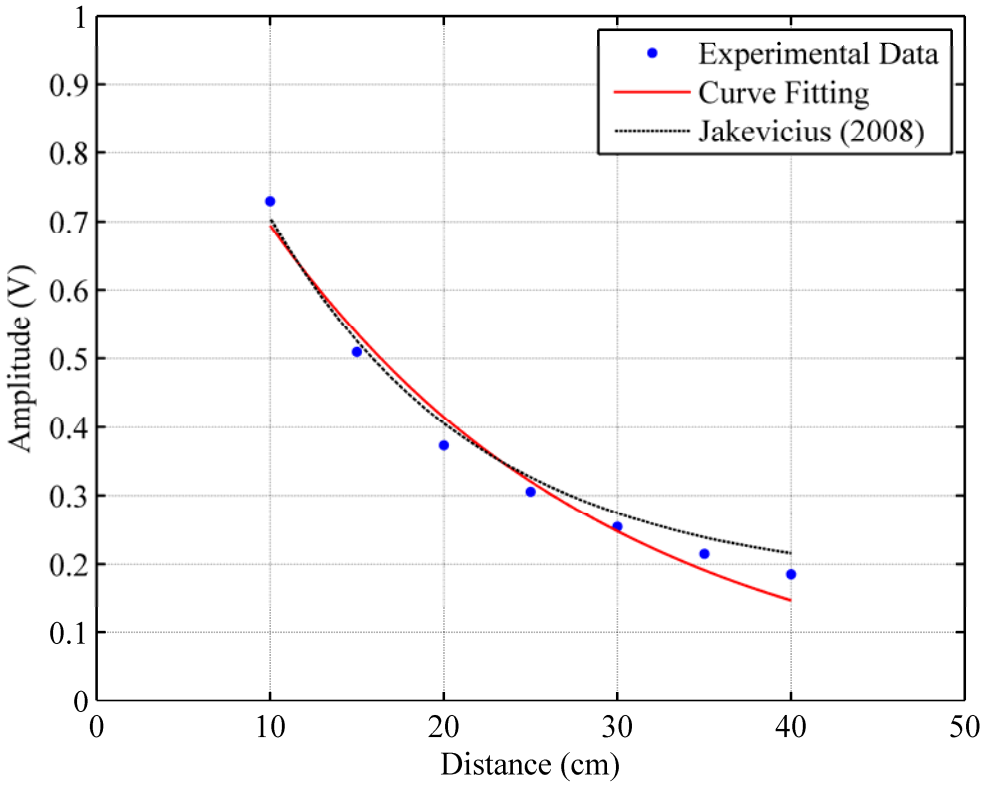

Figure 7.6. Attenuation curve fitting

Figure 7.6 displays the attenuation curve at various wave propagation distances. The theoretical attenuation curve is presented as

$$p(x) = p_0 \cdot \mathrm{e}^{-\alpha x}, \tag{7.1}$$

where p_0 is the pressure without energy absorption, x is the wave propagation distance, and α is the coefficient of absorption (dB/in. or dB/m). A single-term exponential model is used to generate the experimental attenuation curve using MATLAB. The results of

Jakevicius and Demcenko (2008) provide less energy absorption in air because they demonstrated the experiment in a closed chamber.

7.2.3 Air-coupled Array Design

The major purpose of the air-coupled 20 array ultrasonic source is to make an optimal focal point at the focused line as a line source. The maximized focal point will generate the highest-pressure amplitude. It is easy to steer the angle of columns. However, the sensors have to be aligned as accurately as possible on the column decks. Each sensor slot is polished precisely, and the sensors are placed as evenly as possible on the column decks. Figure 7.7 defines the axis and columns used in this experiment. Column

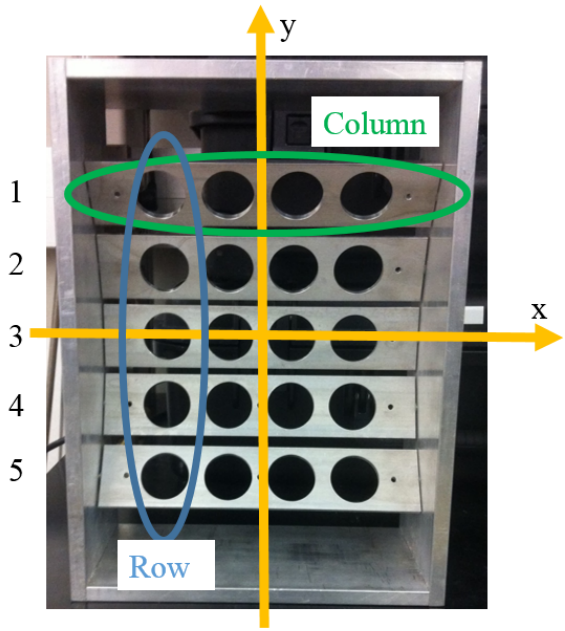

Figure 7.7. Axis of the array

The microphone sensor measures the pressure amplitude. The microphone sensor is placed at the optimum focal line, as recommended by Blum (2003). Each column operates separately to obtain the pressure amplitude from one sensor. Table 7.1 shows each pressure amplitude.

Table 7.1. Pressure amplitude of each column

	Column 1	Column 2	Column 3	Column 4	Column 5
Amplitude (mV)	224	292	328	312	228

The optimum combined voltage of five columns is 1,384 mV. However, the actual measurement with all five columns operating is 878 mV. The operation generates 63.4% of the ideal pressure amplitude. The combined voltage is separated into five individual circuits. Because the voltage is proportional to the pressure amplitude, each sensor generates less pressure amplitude than when it operates all together. Columns 2 and 4 are supposed to have similar pressure amplitudes. However, column 4 has a higher amplitude than column 2 because of the alignment error of the transducers.

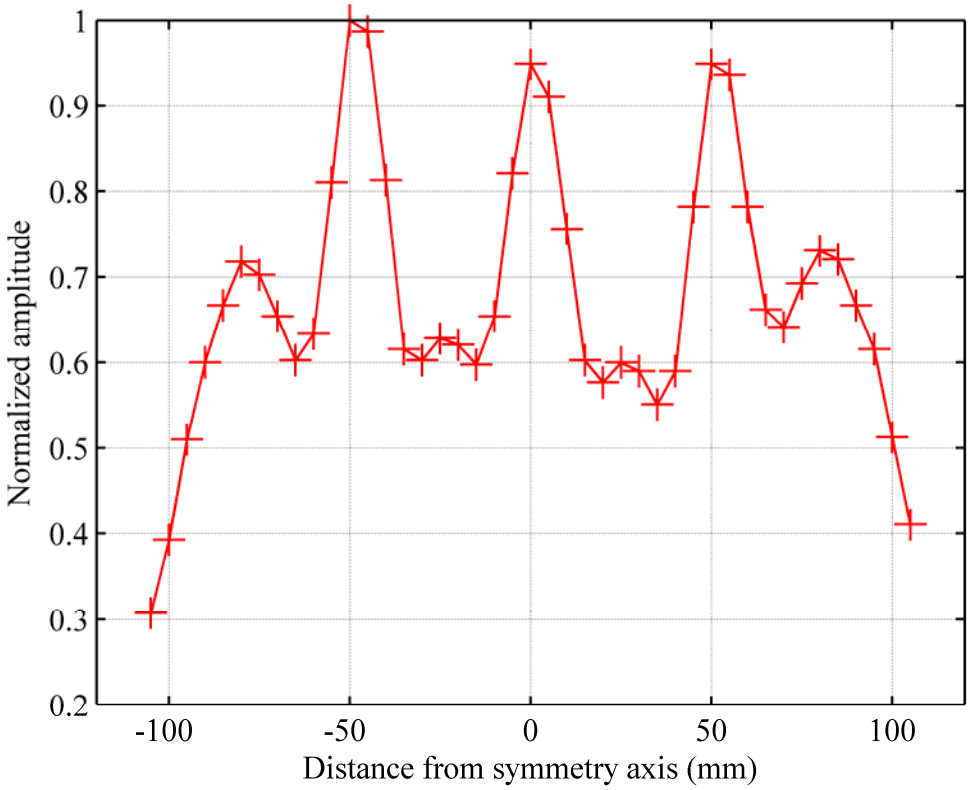

Figure 7.8. Pressure amplitude in the x-direction without a slit plate

The microphone sensor measures the pressure amplitudes along the x-axis and y-axis as shown in Figure 7.8 and 7.9, respectively. The data are collected every 0.20 in. (5 mm). The amplitude is normalized to the peak value of 878 mV at –2.0 in. (–50 mm). There are only three peaks on the x-direction measurement because of the principle of two point source interference pattern.

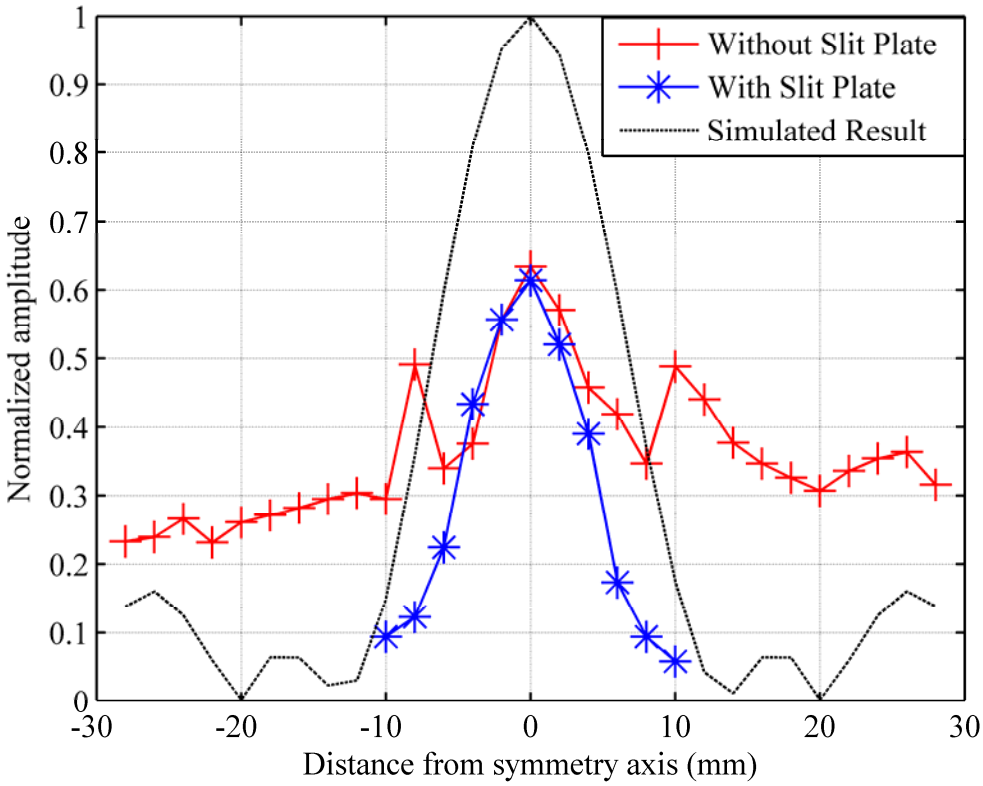

Figure 7.9. Pressure amplitude in the y-direction with and without a slit plate

Figure 7.9 contains the results of the signals with and without a slit plate. The results with and without the slit plate are measured for every 0.079 in. (2 mm), as well as the simulated data. The main purpose of the slit plate is to remove the side lobes at the focal line. The data are normalized to the maximum ideal pressure value of 1,384 mV. The simulation results are used as the ideal case. The spacing of the slit plate is set to 0.167 in. (4.25 mm), as recommended by Blum (2003). ABAQUS is used to simulate air-coupled ultrasonic. The air-coupled 20-array ultrasonic system is optimized and validated to use as an air-coupled ultrasonic generation source.

7.2.4 Efficient Point Source of Air-coupled Ultrasonic

The major issue of the air-coupled 20-array ultrasonic source is to make an optimal focal point at the focus line. In addition, it losses a significant amount of energy because of the fixed 7.87 in. (20 cm) of wave propagation distance. It is tested to find the maximum capacity of one air-coupled ultrasonic transducer.

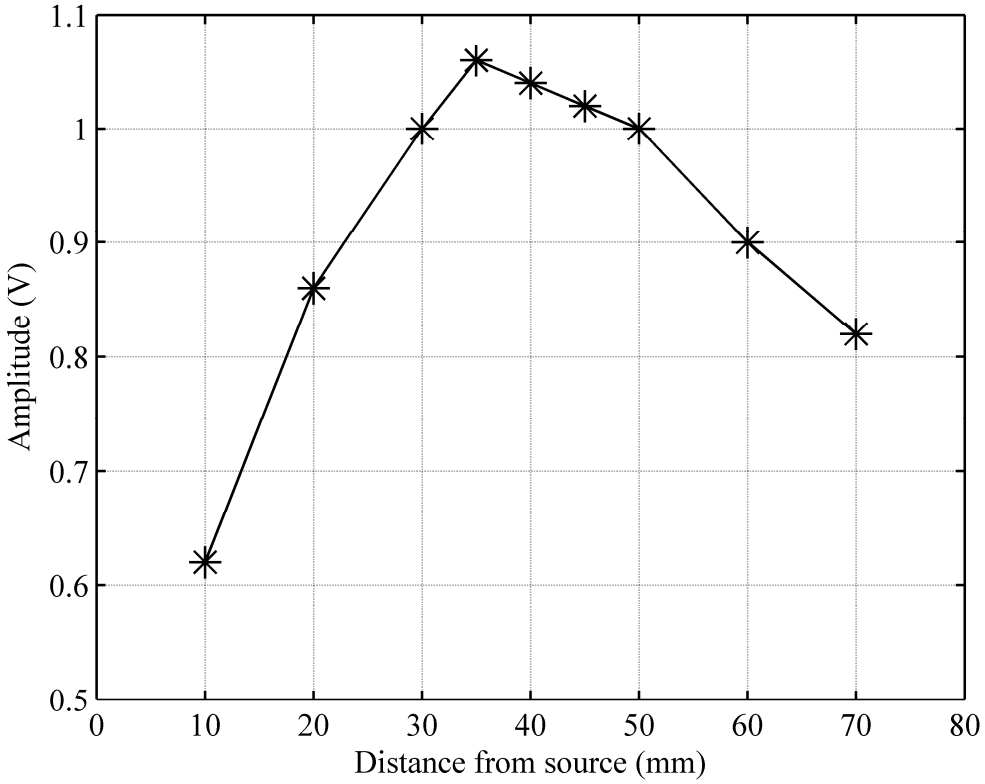

Figure 7.10. Variation of pressure amplitudes with change in source distance

Because of the attenuation in air, the shorter wave propagation distance is better. However, near-field effects have to be accounted for. The theoretical near-field distance is

$$N = \frac{D^2 f}{4 v}, \tag{7.2}$$

where D is the diameter of transducer, f is the frequency, and v is the wave velocity of the material.

The theoretical near-field distance is 2.10 in. (53.4 mm). For the experimental results shown in Figure 7.10, the maximum pressure amplitude is 1,060 mV at 1.37 in. (35 mm) from the ultrasonic source.

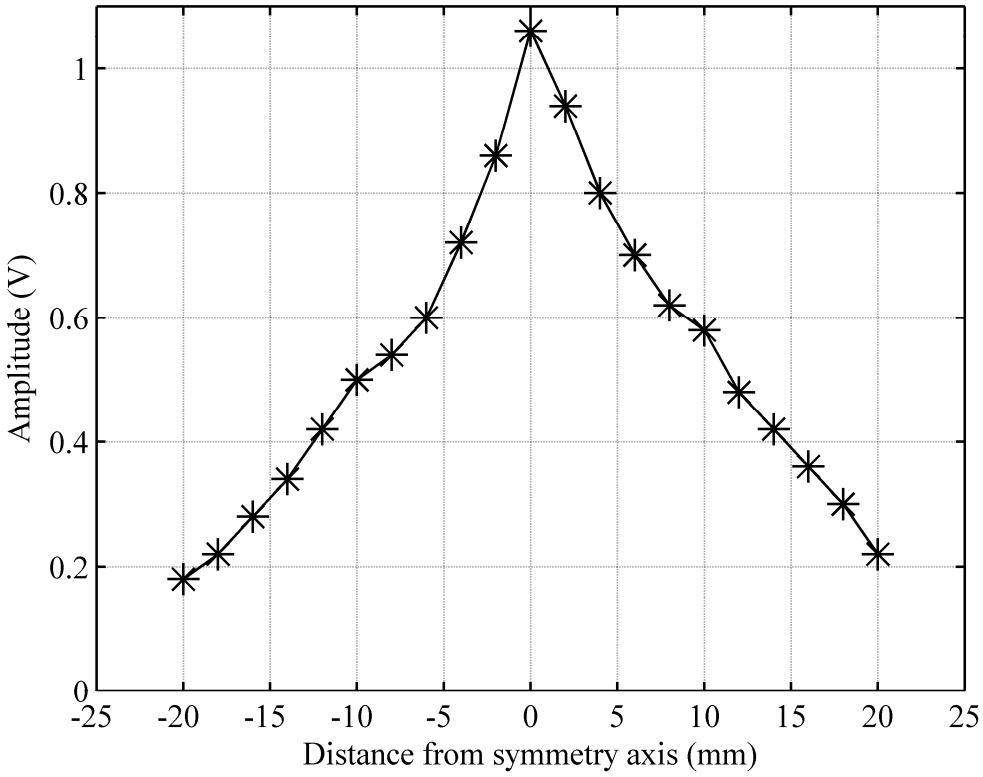

Figure 7.11. Pressure amplitude of one transducer in the y-direction

Figure 7.11 shows that no side lobe is generated when only one transducer is used. It provides the sufficient pressure amplitude within 0.20 in. (5 mm) from the symmetric axis to test the specimen.

It is recommended to employ only one transducer for the purpose of a point source. The one air-coupled ultrasonic transducer system provides about 20% higher amplitude than the 20-array air-coupled ultrasonic system. Attenuation in air is the critical factor for designing the air-coupled ultrasonic experiment.

7.3 Air-coupled Ultrasonic Detection Results

7.3.1 Signal Processing

The low pass and high pass filters are designed using MATLAB. The sampling frequency is set to 5 MHz based on the signal received from the oscilloscope. The excitation frequency of 80 kHz and 60 kHz is used for LDPE and aluminum, respectively, based on the recommendation by Blum (2003). The excitation frequency of 60 kHz is used for concrete, which is determined by a parametric study. Figure 7.12 shows the variation in amplitude as the frequency changes in concrete material. The results are normalized by the maximum amplitude of 1,060 mV at 60 kHz. Table 7.2 represents each filter cutoff frequency.

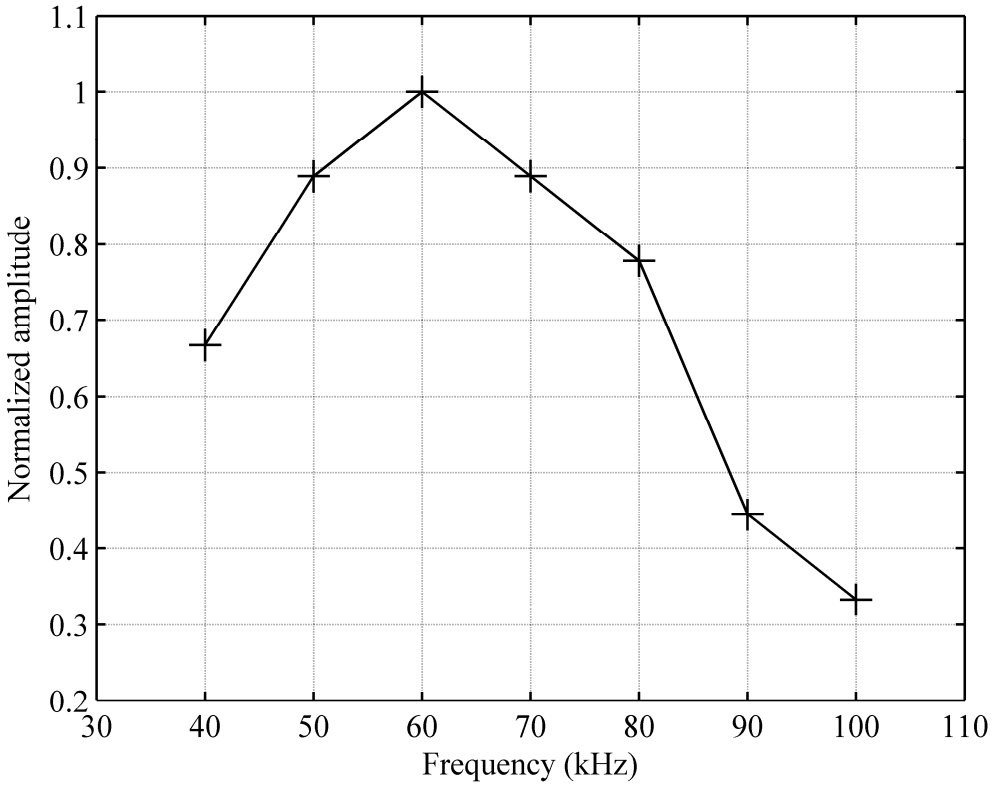

Figure 7.12. Output amplitude change in concrete mortar

Table 7.2. High pass and low pass filters for each specimen

	High pass filter (kHz)	Low pass filter (kHz)
LDPE	70	90
Aluminum	50	70
Concrete	50	70

7.3.2 Through-Transmission Method—P-Wave

The microphone sensor and LDV are used to detect the air-coupled ultrasonic signals. The microphone sensor is set to gain 1 for comparison purposes with LDV. A low-pass filter of 250 kHz is enabled on LDV with a range of 39.4 in/s/V (1 m/s/V).

7.3.2.1 LDPE Plate

The P-wave speed of LDPE and air are 81,968.5 and 13,385.8 in/s (2,082 and 340 m/s), respectively. The distances from the ultrasonic source to the specimen of microphone and laser detection are 0.79 and 1.26 in. (20 and 32 mm), respectively. The distance from microphone to specimen is 0.39 in. (10 mm). The specimen thickness is 1.63 in. (41.4 mm).

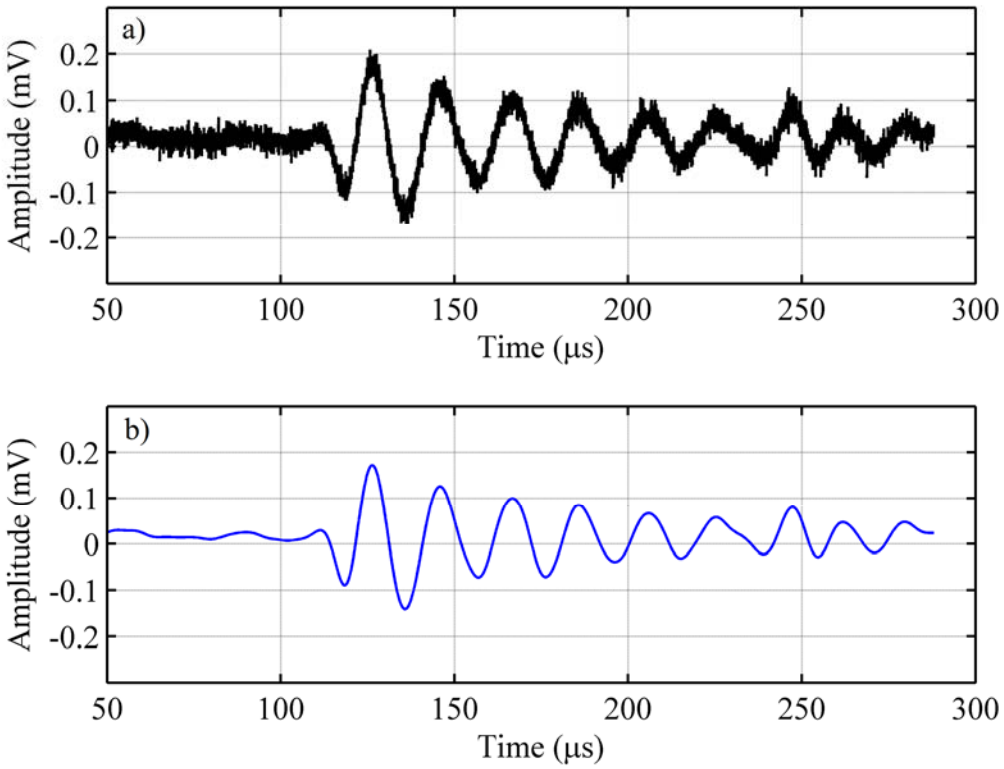

Figure 7.13. Results on LDPE plate (80 kHz) with microphone detection: a) raw data and b) filtered data

As shown in Figure 7.13, the experimental arrival time is 105.6 μs. The theoretical arrival time is 108.1 μs. The measurement matches the theoretical value well. The maximum received voltage is 0.070 mV.

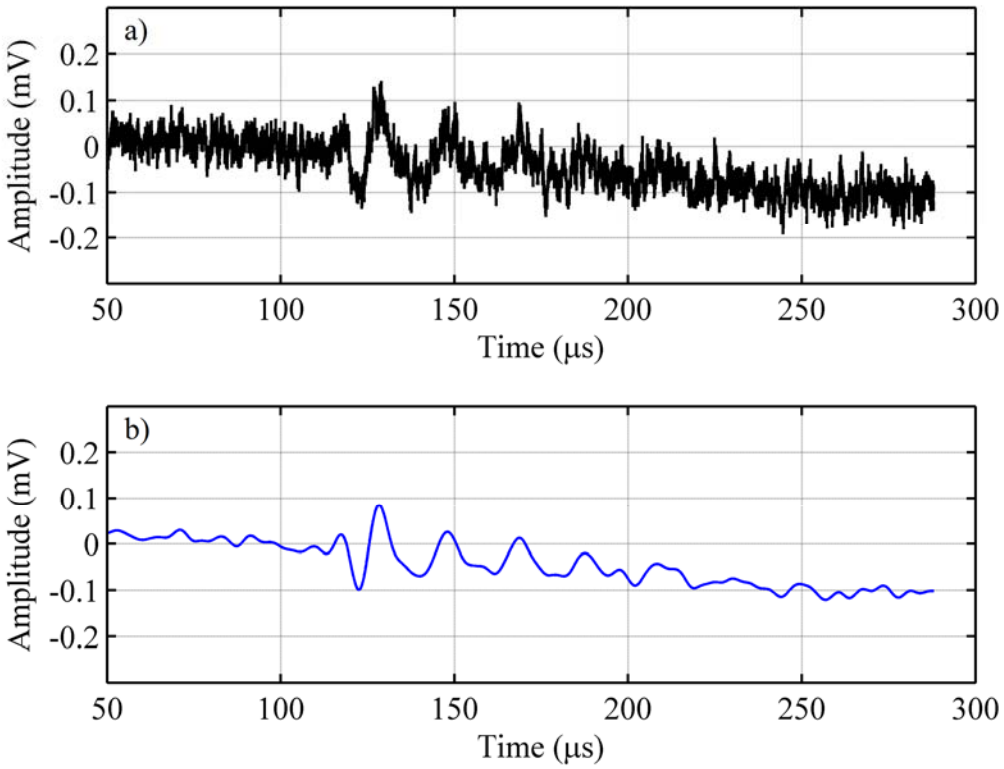

Figure 7.14. Results on LDPE plate (80 kHz) with LDV detection: a) raw data and b) filtered data

Figure 7.14 shows the wave motion on an LDPE plate with LDV. The experimental arrival time is 110.88 μs. The theoretical value is 114.0 μs. The maximum received voltage is 0.054 mV.

7.3.2.2 Aluminum Sheet

The P-wave speed of aluminum is 252,756 in/s (6,420 m/s). The distances from the ultrasonic source to the specimen are 0.79 in. (20 mm) for a microphone sensor and 1.26 in. (32 mm) for LDV. The wave propagation time for a 0.020-in. (0.5-mm)-thick

aluminum sheet is negligible. The distance from microphone to specimen is 0.39 in. (10 mm).

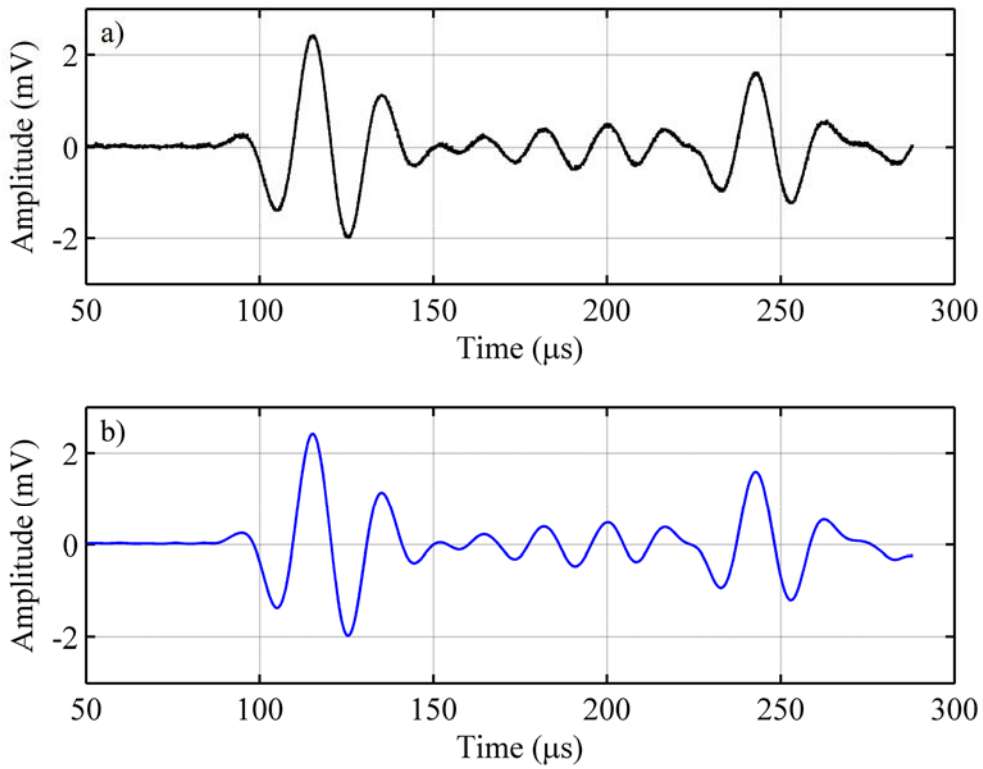

Figure 7.15. Results on aluminum sheet (60 kHz) with microphone detection: a) raw data and b) filtered data

As shown in Figure 7.15, the experimental arrival time is 83.2 μs. The theoretical arrival time is 88.2 μs. The measurement matches the theoretical value well. The maximum received voltage is 1.571 mV.

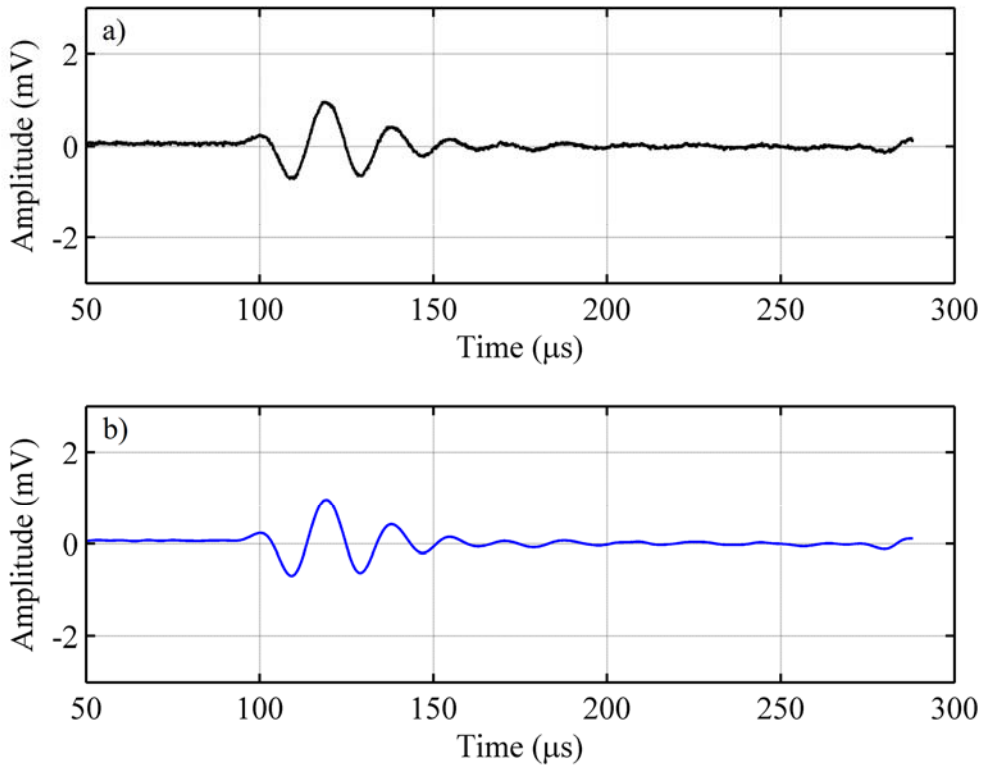

Figure 7.16. Results on aluminum sheet (60 kHz) with LDV detection a) raw data and b) filtered data

Figure 7.16 shows the wave motion on an aluminum sheet with LDV. The experimental arrival time is 96.6 μs. The theoretical value is 94.1 μs. The maximum received voltage is 0.642 mV.

7.3.2.3 Concrete Mortar: 0.75 and 1.5 in. (19 and 38 mm)

The measured P-wave speed of concrete mortar is 3,248 m/s. Two different thicknesses of mortars are tested: 0.75 and 1.5 in. (19 and 38 mm). The microphone sensor and LDV are used to detect the signal. The distances from the ultrasonic source to the

specimen of microphone and laser detection are 0.79 and 1.26 in. (20 and 32 mm), respectively. The distance from microphone to specimen is 0.31 in. (8 mm).

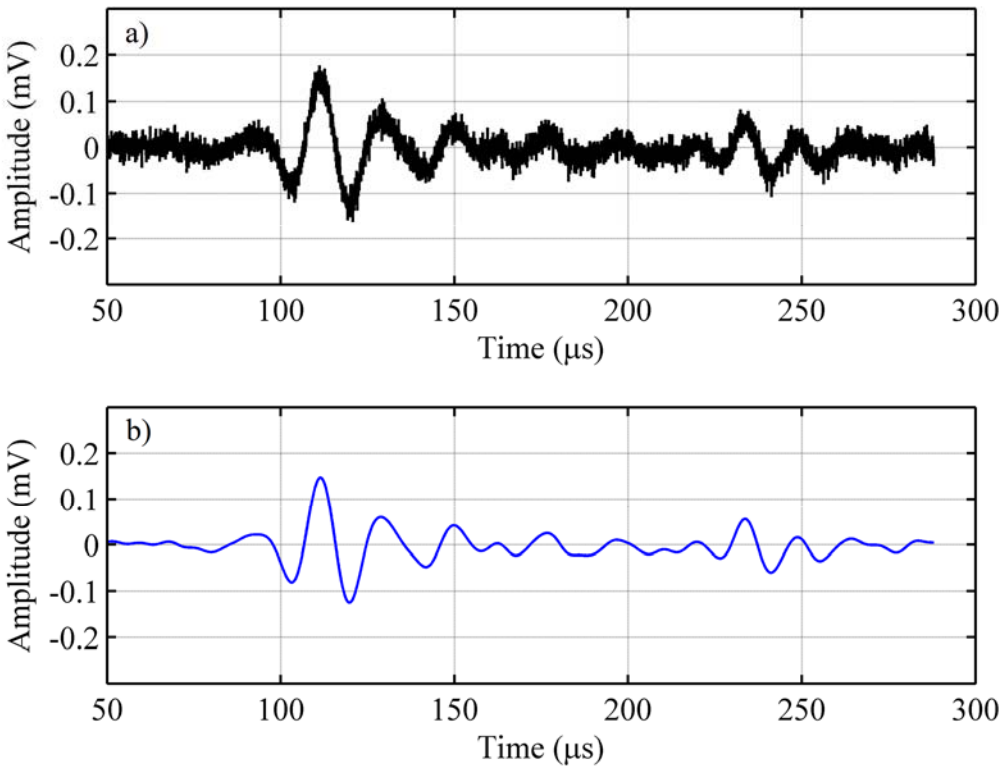

Figure 7.17. Results on 0.75-in. (19-mm) mortar (60 kHz) with microphone detection: a) raw data and b) filtered data

Figure 7.17 shows the wave motion in 0.75-in. (19-mm) mortar with a microphone. The experimental arrival time is 87.2 μs. The theoretical value is 87.9 μs. The maximum received voltage is 0.111 mV.

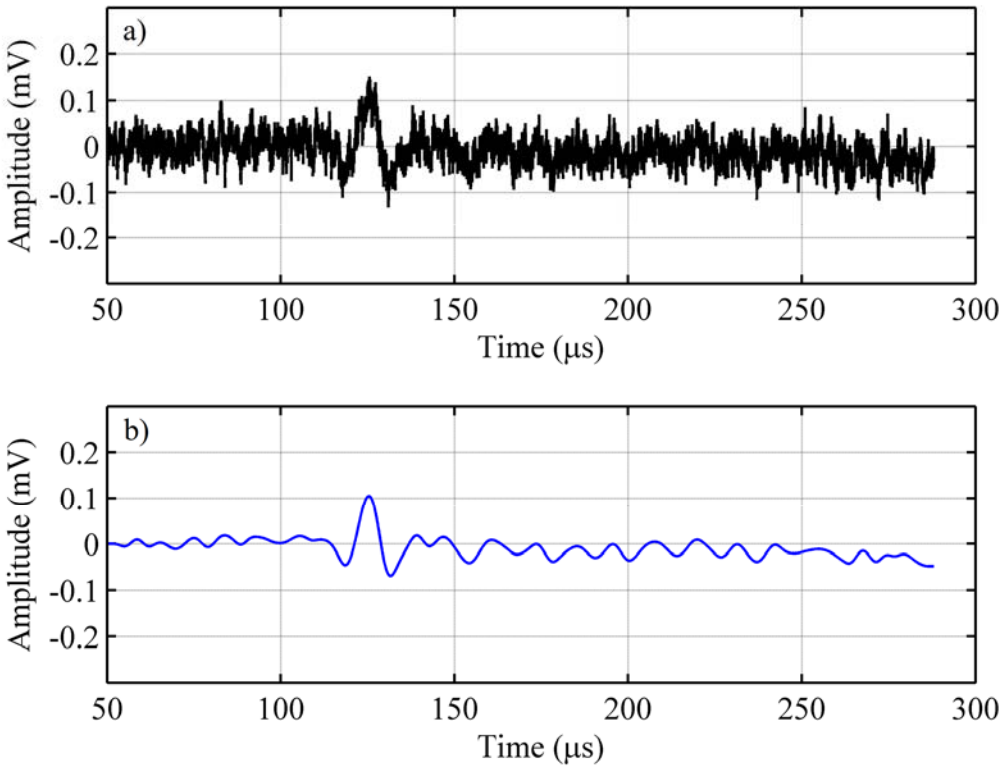

Figure 7.18. Results on 0.75-in. (19-mm) mortar (60 kHz) with LDV detection: a) raw data and b) filtered data

Figure 7.18 shows the wave motion in 0.75-in. (19-mm) mortar with LDV. The experimental arrival time is 102.7 μs. The theoretical value is 99.7 μs. The maximum received voltage is 0.068 mV.

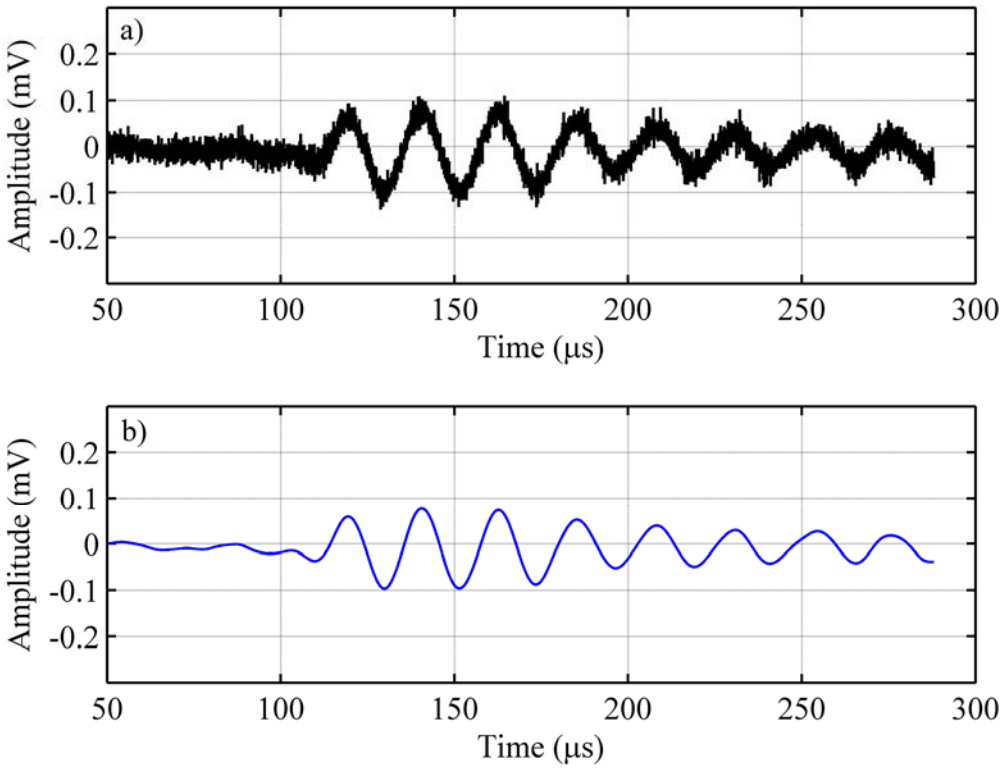

Figure 7.19. Results on 1.5-in. (38.1-mm) mortar (60 kHz) with microphone detection: a) raw data and b) filtered data

Figure 7.19 shows the wave motion in 1.5-in. (38.1-mm) mortar with a microphone. The experimental arrival time is 94.64 μs. The theoretical value is 93.5 μs. The maximum received voltage is 0.062 mV.

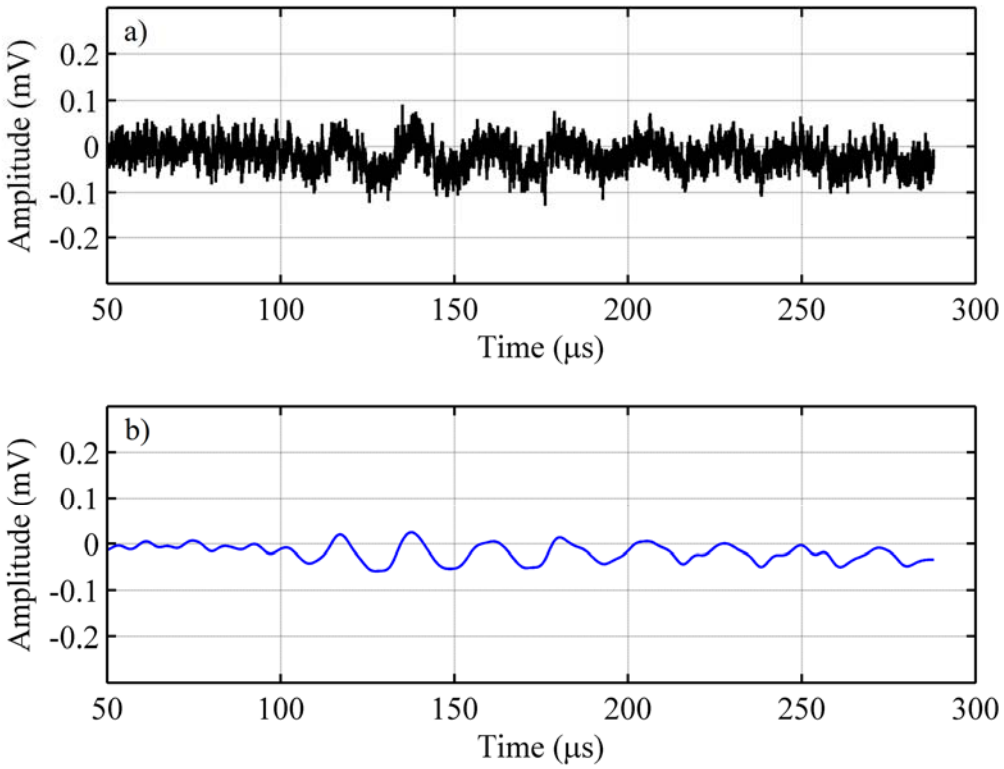

Figure 7.20. Results on 1.5-in. (38.1-mm) mortar (60 kHz) with LDV detection: a) raw data and b) filtered data

Figure 7.20 shows the wave motion in 1.5-in. (38.1-mm) mortar with LDV. The experimental arrival time is 106.3 μs. The theoretical value is 105.3 μs. The maximum received voltage is 0.034 mV.

7.3.3 Pitch-Catch Method—Rayleigh Wave

The concrete mortar specimen is employed for the pitch-catch method experiment using a Rayleigh wave. The Rayleigh wave is generated using the point source of air-coupled ultrasonic. One-side inspection is performed with a complete non-contact

ultrasonic technique, as shown in Figure 7.21. The air-coupled ultrasonic transducer is placed 1.18 in. (3 cm) apart from the specimen. The distance from the air-coupled ultrasonic transducer to LDV is 3.54 in. (9 cm).

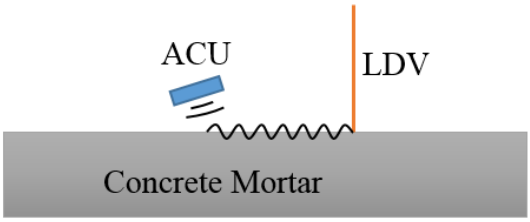

Figure 7.21. One-side inspection using the non-contact ultrasonic technique

The S-wave speed, Rayleigh wave speed, and incident angle are calculated as 89,137.8 in/s (2,264.1 m/s), 81,311 in/s (2,065.3 m/s), and 9.47°, respectively, using the equations provided in Chapter 3. It is expected that the maximum amplitude will occur when the incident angle is 9.47° based on Snell's law. The experimental result is shown in Figure 7.22. The amplitude peak occurs at 9.5°.

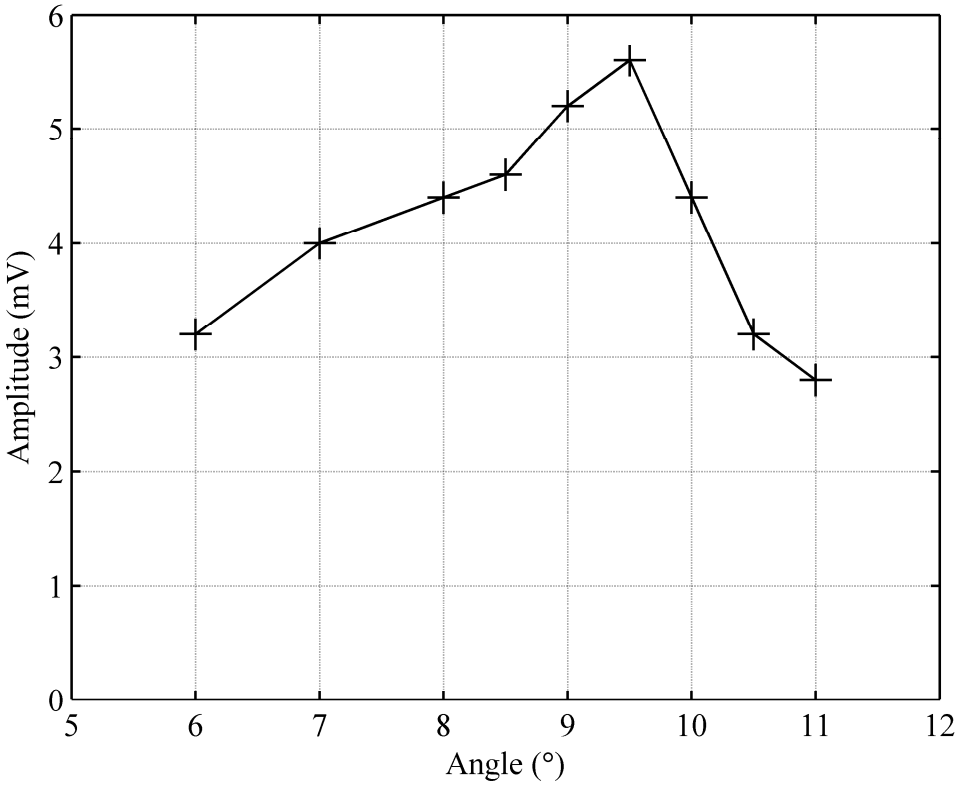

Figure 7.22. Transmitting angle of air-coupled ultrasonic at 70 kHz

Using the pitch-catch measurement, the signal generated by one air-coupled ultrasonic with frequencies ranging from 40 to 110 kHz are shown in Figure 7.23.

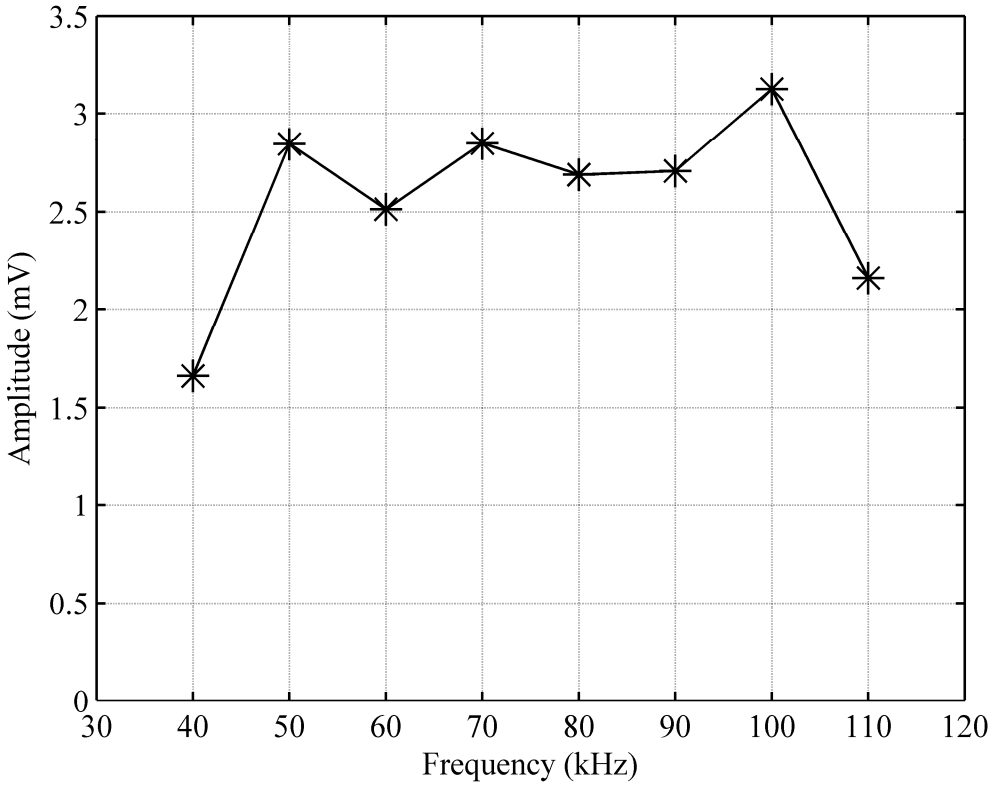

Figure 7.23. Transmitting frequencies of air-coupled ultrasonic on the concrete surface at 9.5°

It is observed that the frequencies ranging from 50 to 100 kHz have similar high amplitudes. The highest amplitude occurs at 100 kHz and is a function of the material property of concrete mortar.

The one-side non-contact crack detection is employed to verify the Rayleigh wave propagation. An excitation frequency of 100 kHz and an incident angle of 9.5° are used in this experiment. An artificial crack is made on the concrete mortar surface. The depth of the crack is 0.20 in. (5 mm), as shown in Figure 7.24.

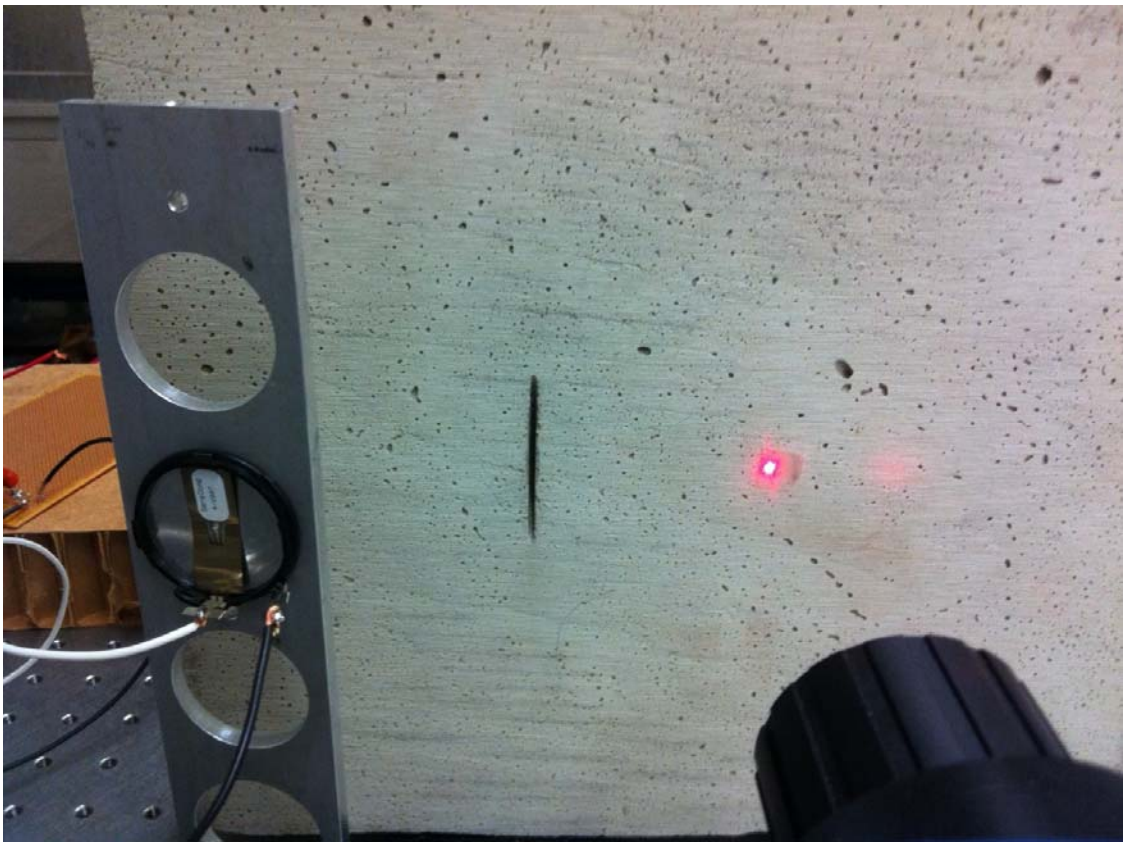

Figure 7.24. An artificial crack on concrete mortar

The results of the cracked region and uncracked region are compared in Figure 7.25. The theoretical arrival time is 187 μs, which includes 1.57-in. (40-mm) propagation time in air and 5.71 in. (145 mm) for the concrete mortar surface.

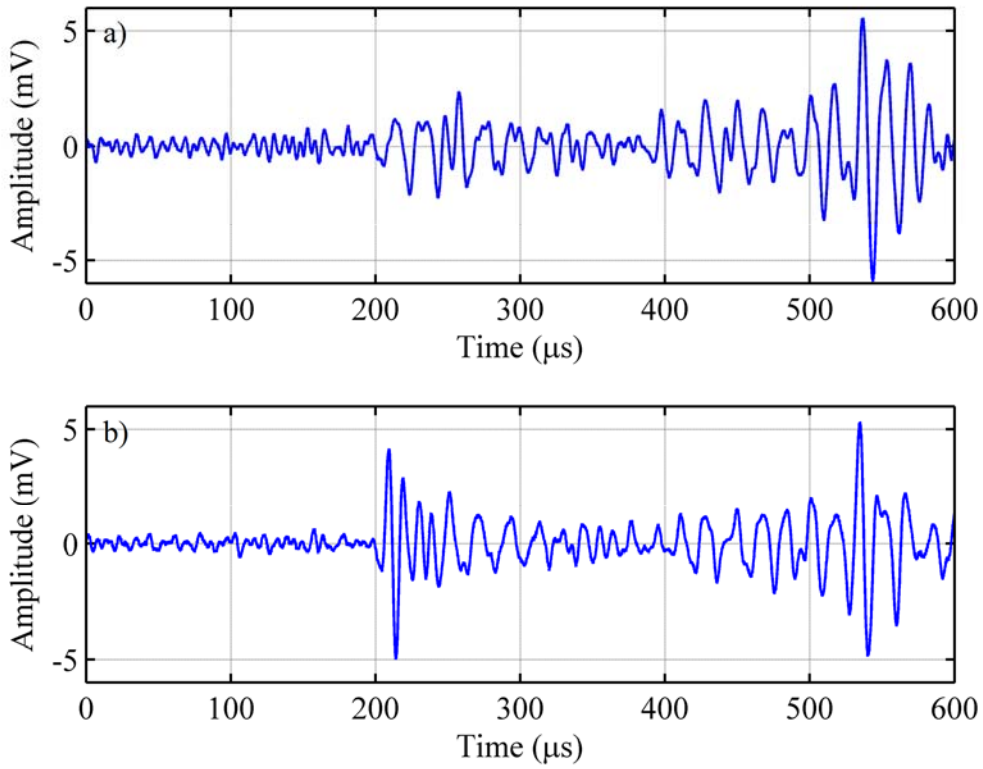

Figure 7.25. Rayleigh wave on concrete surface (100 kHz): a) cracked region and b) uncracked region

The experimental arrival time of the uncracked case is 190.6 μs for pitch-catch mode. However, the Rayleigh wave is not detected at the expected region because most of the transmitted energy from the source is reflected back to the other direction.

7.4 Limitations and Feasibility of Air-coupled Ultrasonic System

The air-coupled 20-array ultrasonic source can generate the effective excitation frequency of ultrasonic waves from 50 to 100 kHz. Higher frequencies cannot be achieved because of attenuation by air. The generated ultrasonic waves successfully penetrate the

aluminum sheet, the LDPE plate, and the concrete mortar using the through-transmission technique. A complete non-contact system is demonstrated in this research. The signal conditioner that is attached to the microphone provides a maximum voltage gain of 100 (40 dB of power gain). The best results can be measured using a microphone with a voltage gain of 100. The LDV obtained less amplitude of signal than the microphone with the same gain setting. All received signals are filtered using a low pass and high pass filter using MATLAB software. It is difficult to generate Rayleigh waves or S-waves from an air-coupled 20-array ultrasonic source because of the placement of sensors. Because the 20-array sensors has a complex design, it is difficult to generate an angled beam, such as Rayleigh waves and shear waves. Therefore, the array application is difficult to apply in the crack detection of railway axles.

This research shows the feasibility of an air-coupled concrete inspection, especially when one air-coupled ultrasonic sensor is used. One of the methods to find a material property of concrete is the ultrasonic testing approach. The system can be a handy tool for finding the material properties, such as modulus of elasticity, because it does not require a coupling medium.

Finally, the one-side non-contact crack detection is demonstrated using a Rayleigh wave. The microphone sensor cannot detect the Rayleigh wave signal, but the LDV can. It successfully distinguished between a cracked region and an uncracked region by the time-of-flight technique. The one-side non-contact ultrasonic application is beneficial for inspecting when the application has limited accessibility, such as a concrete wall.

7.5 Laser Array Detection with a Steel Specimen

7.5.1 Background and Design of Array

The laser array receiver is designed based on the theory of a two-element antenna array. Two LDVs receive ultrasonic waves from a source in a different path length, as shown in Figure 7.26.

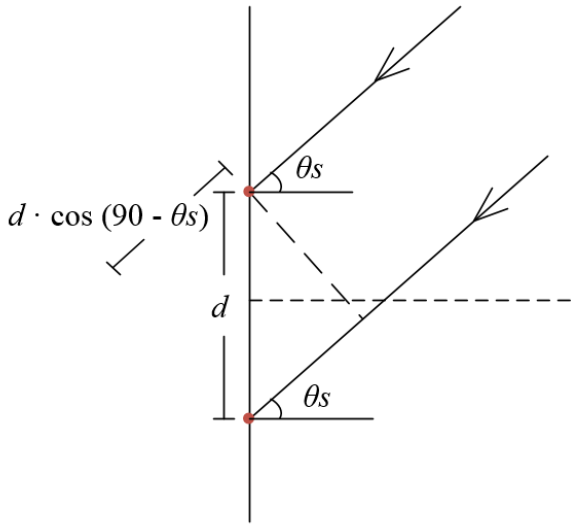

Figure 7.26. Two-linear array

The far-field approximation is made to design the LDV array that receives at two different points with the same angle (Williams 1966 and Balanis 2005). Therefore, the difference of the wave path becomes $d \cdot \cos(90 - \theta_s)$ as shown in Figure 7.26. The detecting angle is calculated using different wave propagation distances. The system is designed based on three parameters: number of element, element spacing, and beam steering range.

The directivity function of the single-point source array model, *H*, is used in this design process (Hansen 1998, and Wooh & Shi 1998)

$$H = \frac{\sin\left(\frac{\pi\, d\, (\sin\theta_s - \sin\theta)}{\lambda}\, N\right)}{\sin\left(\frac{\pi\, d\, (\sin\theta_s - \sin\theta)}{\lambda}\right) N}, \tag{7.3}$$

where d is the spacing between two LDVs, λ is the wavelength, θ is the beam steering angle, θ_s is the receiving angle, and N is the number of element.

7.5.1.1 Parametric Study

The number-of-element study shows how it affects the directivity. The frequency is 2.25 MHz, the receiving angle is 30°, and the spacing is $\lambda/2$ when the number of the element is 2, 4, 8, and 16, as shown in Figure 7.27.

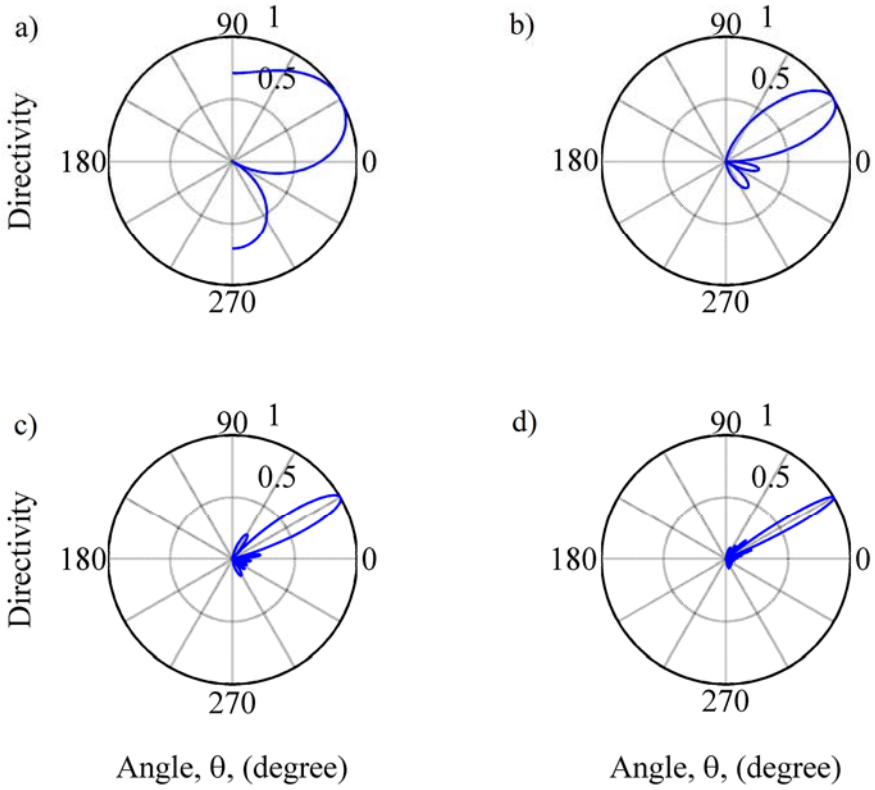

Figure 7.27. Number-of-element study: a) $N = 2$, b) $N = 4$, c) $N = 8$, and d) $N = 16$

More elements provide sharper directivity with less grating and side lobes. A larger number of LDVs will provide better directivity, but this experiment is limited to two.

The distance between two elements is also designed. The frequency is 2.25 MHz, the receiving angle is 30°, and the number of the element is 2 when the spacing is $\lambda/8$, $\lambda/4$, $\lambda/2$, and λ. When the spacing is $\lambda/2$, it provides the best directivity, as shown in Figure 7.28. When the spacing is λ, it has a sharper directivity than $\lambda/2$, but it also generates a grating lobe at –30°. The wavelength of $\lambda/2$ provides the best result. The spacing is 1.25 mm based on the P-wave speed of the specimen and the frequency used.

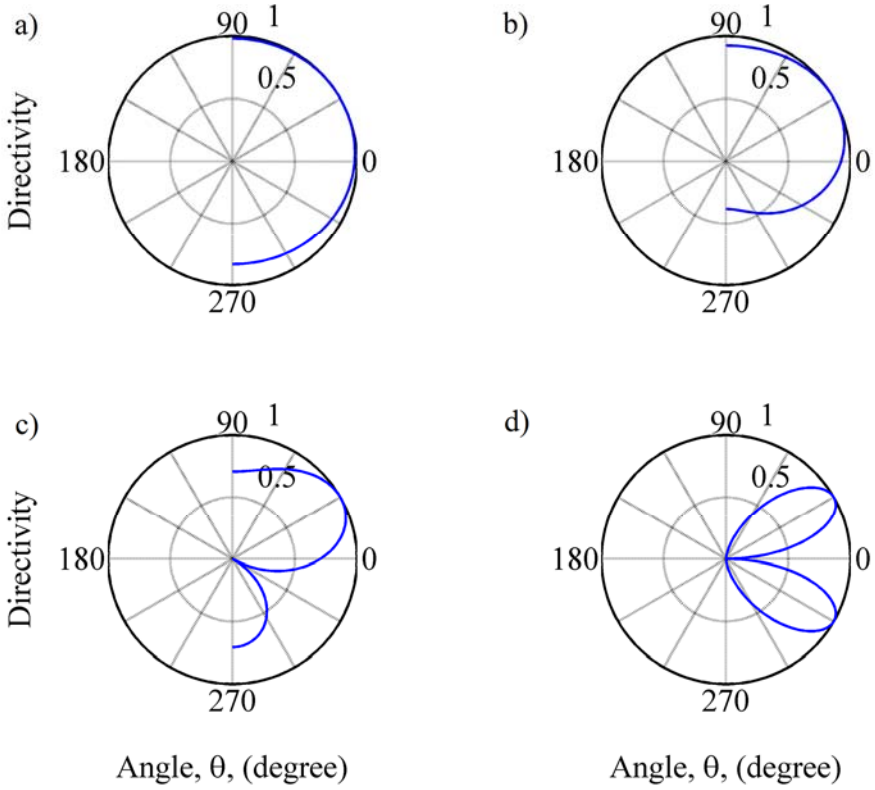

Figure 7.28. Optimum spacing: a) $d = \boldsymbol{\lambda}/8$, b) $d = \boldsymbol{\lambda}/4$, c) $d = \boldsymbol{\lambda}/2$, and d) $d = \boldsymbol{\lambda}$

The steerable angle is designed in this experiment. The frequency is 2.25 MHz, the number of the elements is two, and the spacing is $\lambda/2$ when the receiving angle changes from 0 to 35° at a 5° increment, as shown in Figure 7.29.

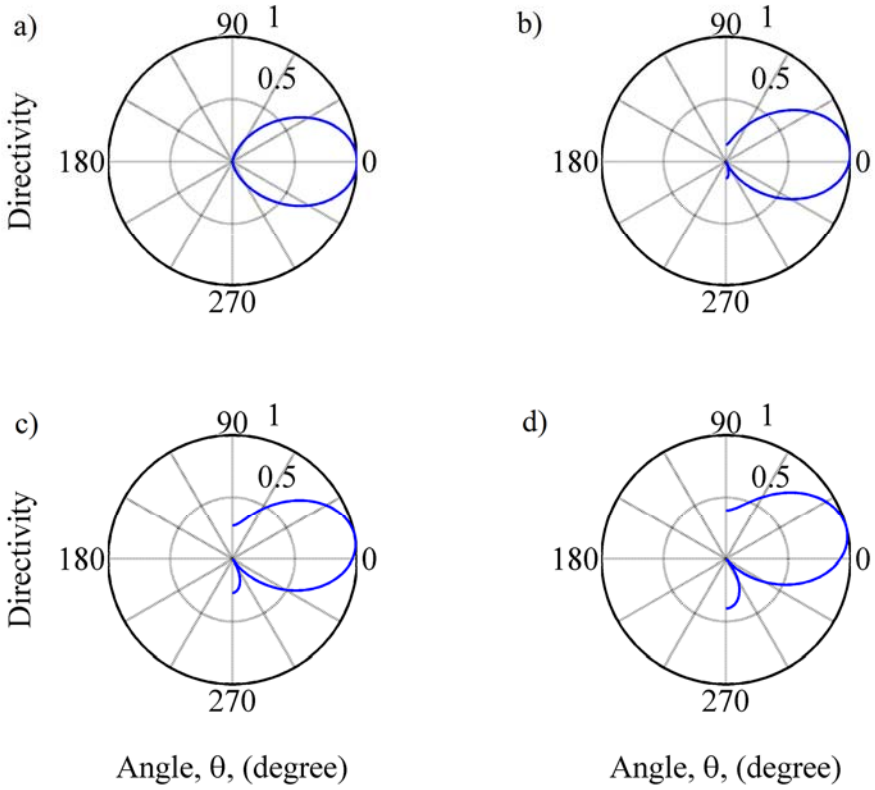

Figure 7.29. Steering angle: a) $\theta = 0°$, b) $\theta = 5°$, c) $\theta = 10°$, d) $\theta = 15°$, e) $\theta = 20°$, f) $\theta = 25°$, g) $\theta = 30°$, and h) $\theta = 35°$

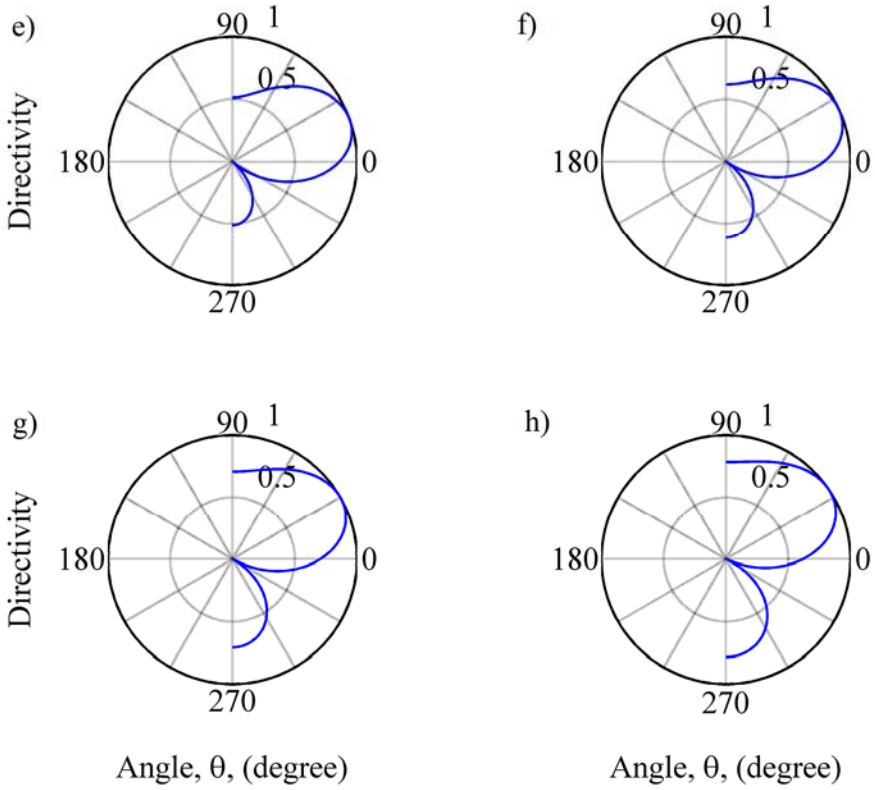

Figure 7.29. Continue

A grating lobe is developed as the angle increases. It is acceptable to use angles from 0 to 15°. Angles exceeding 15° create a significant side lobe.

The frequency of 2.25 MHz is used with two LDV sensors, a spacing of 0.047 in. (1.2 mm), and an angle from –15° to 15°. In this experiment, only P-waves will be generated from the transmitting transducer.

7.5.2 Experimental Setup of Laser Array

The through-transmission mode is used to test the laser array system, as shown in Figure 7.30. The excitation transducer generates a central frequency of 2.25 MHz. The

first signal from the excitation probe to the receiver contains information of one-way propagation and the coupling delay. The coupling delay is measured as 3.5 μs. The second lag signal goes back and forth as the pulse-echo mode does. The first laser measures the A-scan of the specimen. The second laser measures another A- scan, and the angle of excitation is calculated using the arrival time difference of the two lasers.

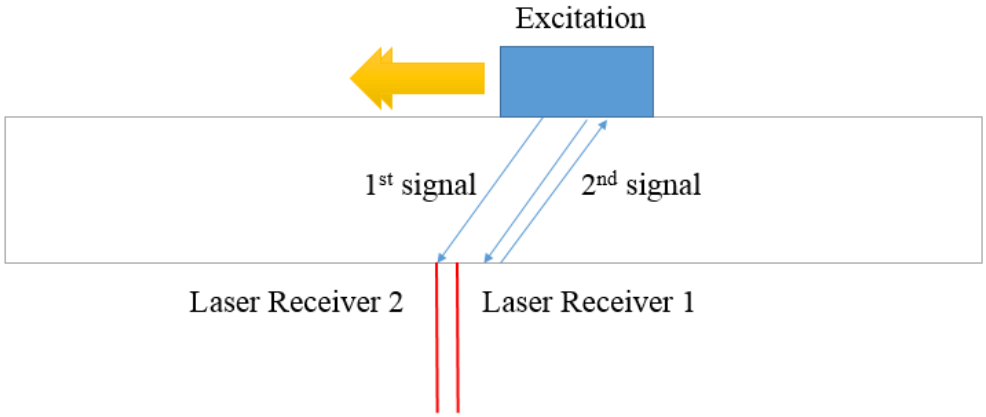

Figure 7.30. Wave propagation scheme

7.5.2.1 LDV

The LDV system is a broadband receiver. The velocity decoder has an upper frequency limit of 2.5 MHz. Two LDVs are used as receivers of ultrasonic signals in this experiment, as shown in Figure 7.31.

Figure 7.31. Laser array system

7.5.2.2 Contact Ultrasonic Transducer

This experiment uses the Panametrics A403 with a central frequency of 2.25 MHz. The transducer is directly in contact with the specimen. It only generates an ultrasonic P-wave.

7.5.2.3 Test Specimen

The test specimen of this experiment is a mild steel plate that has dimensions of 6 × 4 × 1 in. (152 × 102 × 25.4 mm). One side of the specimen has the reflected finish in order to increase the laser signal amplitude. The measured P-wave speed of the specimen is 221,220 in/s (5,619 m/s). It has a hole, which has a diameter of 0.1 in. (2.5 mm), as shown in Figure 7.32.

Figure 7.32. Discontinuity of the test specimen

7.5.2.4 Oscilloscope

An oscilloscope (Tektronics 3034B) is used to record the transmitted and received signals. After 512 samples are obtained, the signals are averaged by the oscilloscope. The data are transferred to a PC via a network using an Ethernet cable and are analyzed using MATLAB.

7.6 Laser Array System Results

As shown in Figure 7.33, there is no information on the first lag as to whether there is or isn't a crack. After the first lag, each lag has a 9.4-μs interval for a 1-in. steel specimen. It acts in pulse-echo mode from the second lag. It is easy to identify the crack information.

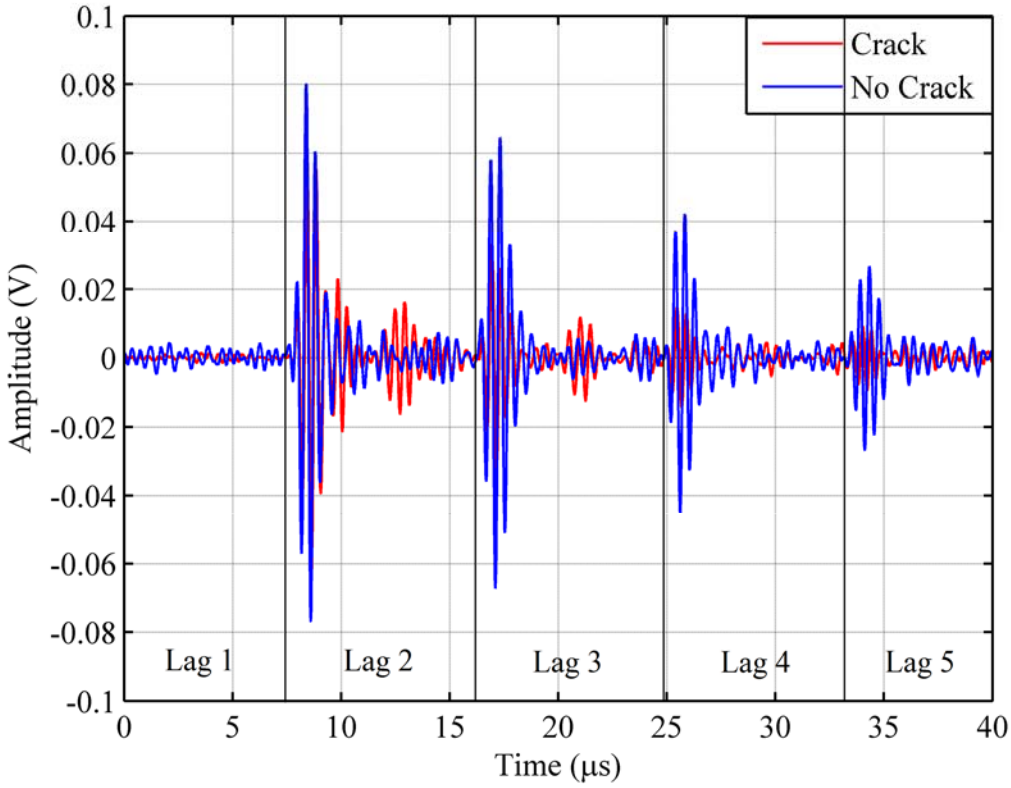

Figure 7.33. Resulting signal of cracked and uncracked region

Figure 7.34 compares the time domain signal. The maximum value of the result is marked with a red star on the curve. The red lines connect the maximum values of the results across the plots. The resulting signals are compared using the time-of-flight technique. Table 7.3 shows the comparison of the theoretical and experimental arrival times. The arrival time at 0° is used as the baseline and the other arrival time is subtracted from the 0° result.

Table 7.3. Comparison of arrival time

Angle	–15°	–10°	–5°	0°	5°	10°	15°
Theoretical (ns)	160	70	20	0	20	70	160
Experimental (ns)	140	30	0	0	10	40	160

The experimental results are different from the theoretical values. The inconsistency occurs because the coupling medium applied in the ultrasonic generation source can cause the error in the results. After 512 samples are obtained, the signals are averaged by the oscilloscope. Several measurements are taken to ensure accurate results.

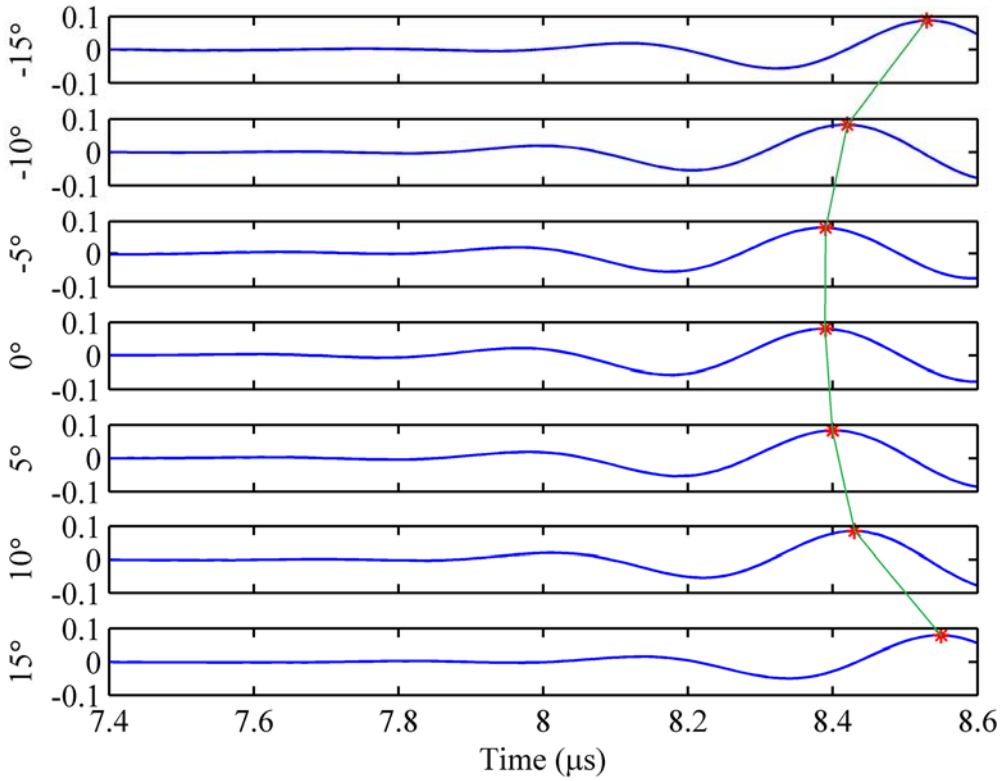

Figure 7.34. Wave arrival time of different angles

Figure 7.35 compares the time difference between the two lasers. The difference is used to calculate the refracted angle of the ultrasound. The experimental results in Figure 7.35 are set to a baseline to calculate the refracted angles. The theoretical difference is calculated based on the thickness of the material and the P-wave speed with far-field approximation.

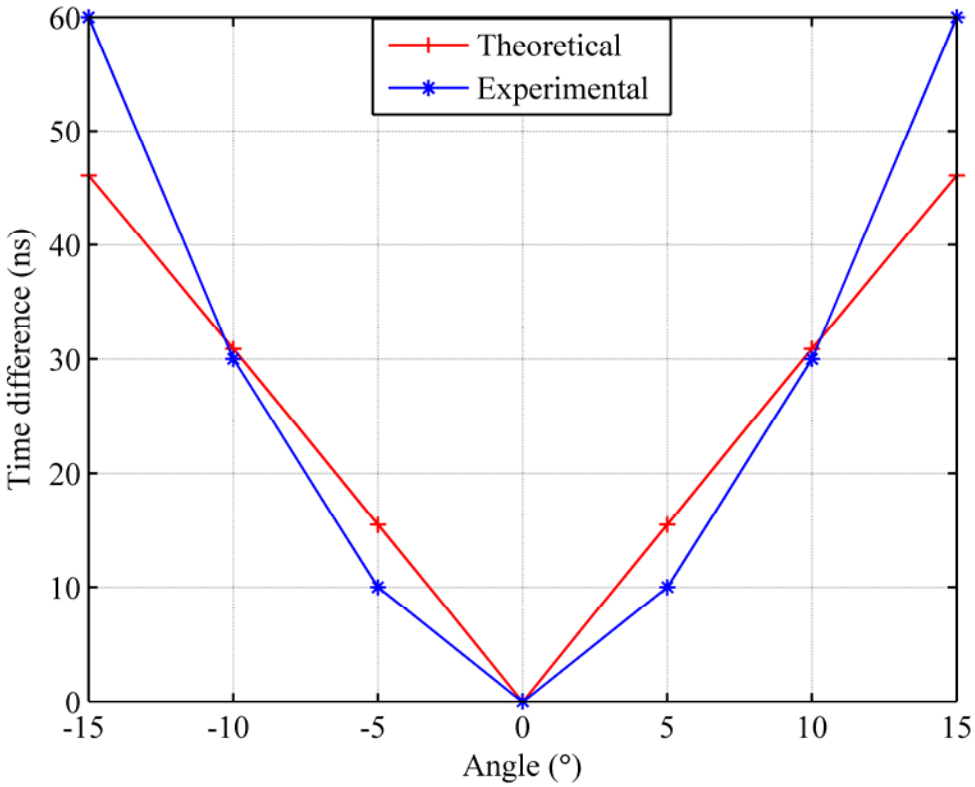

Figure 7.35. Time difference of two laser receivers

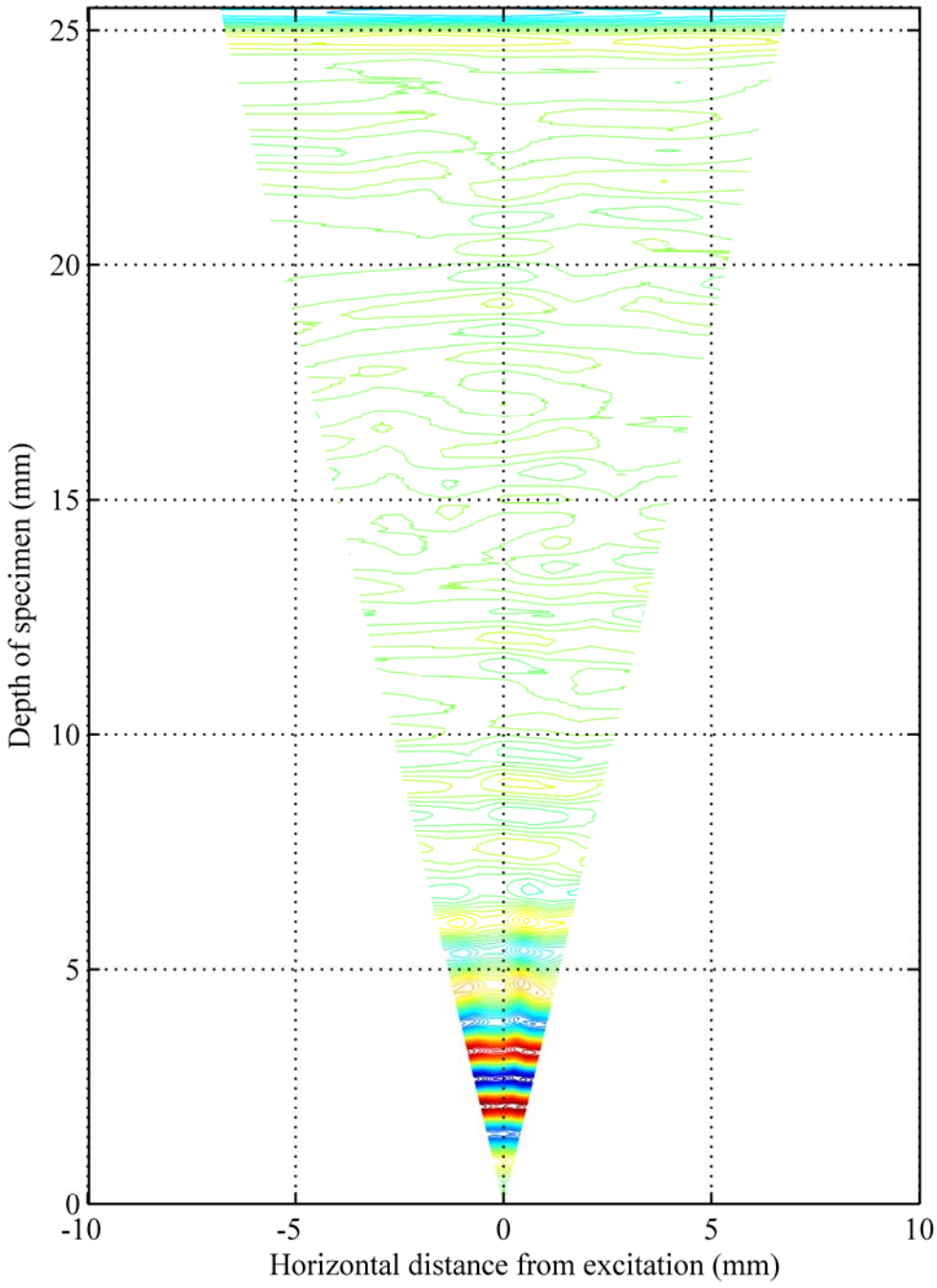

Figure 7.36. S-scan result of laser array—uncracked region from –15° to 15°

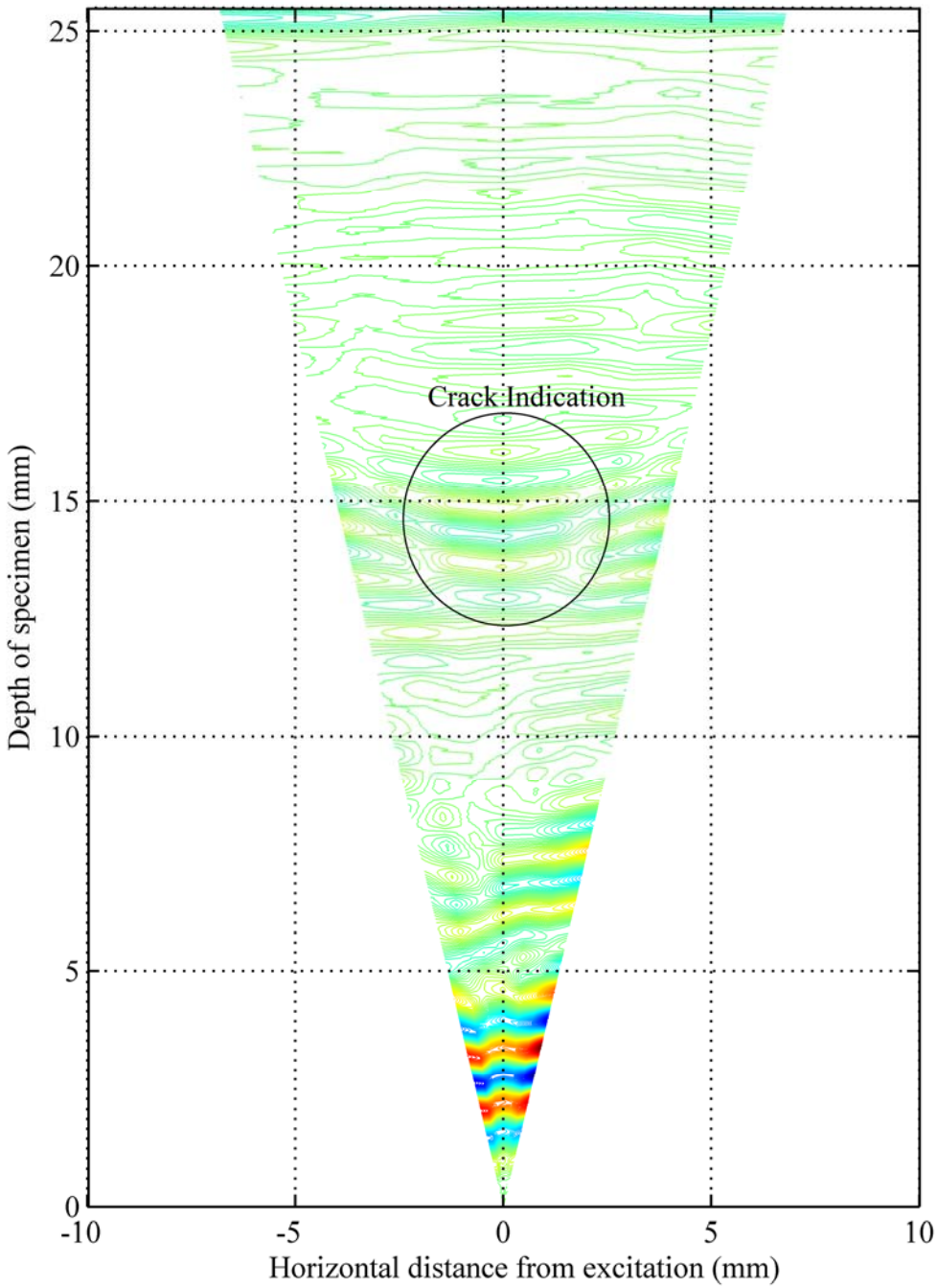

Figure 7.37. S-scan result of laser array—cracked region from –15° to 15°

The signal processing technique is developed using MATLAB for the laser array receiver. Based on the angle obtained from the time domain signal, the coordinate of each time domain signal is assigned in the 2D plane. The first lag signal, which contains a coupling delay and one-way wave propagation, is removed because it does not provide any crack information. The second lag signal contains a back-and-forth wave signal. To obtain the corrected distance in the figures, the propagation time is divided in half. Figures 7.36 and 7.37 show the results of the cracked and uncracked regions. The developed program requires input variables of A-scan matrix, wedge delay, wave speed, and depth of specimen.

7.7 Conclusions

The air-coupled 20-array ultrasonic source can generate an effective excitation frequency of an ultrasonic wave from 50 to 100 kHz. The higher frequencies cannot be achieved because of the attenuation by air. The generated ultrasonic waves successfully penetrate the aluminum sheet, the LDPE plate, and the concrete mortar using the through-transmission technique. A complete non-contact system is demonstrated in this research. The signal conditioner that is attached to the microphone sensor provides a maximum voltage gain of 100 (40 dB of power gain). The best results can be measured using a microphone with a voltage gain of 100. The LDV obtained less signal amplification than the microphone with the same gain setting. All received signals are filtered using a low pass and high pass filter using MATLAB software. It is difficult to generate surface waves or S-waves using an air-coupled 20-array ultrasonic source because of the placement of

the sensors. Because the ultrasonic wave is focused on a focal line, it is difficult to tilt the array, as this generates noise signal. Consequently, the array application is difficult to apply for the crack detection of railway axles.

The research shows the feasibility of an air-coupled concrete inspection, especially when one air-coupled ultrasonic sensor is used. One of the methods employed to determine a material property of concrete is the ultrasonic testing approach. The system can be a handy tool in obtaining the material properties, such as modulus of elasticity, as it does not require a coupling medium.

The one-side non-contact crack detection is demonstrated using the Rayleigh wave. The microphone sensor cannot detect the Rayleigh wave signal, but the LDV can. It successfully distinguishes between cracked and uncracked regions using the time-of-flight technique. The one-side non-contact ultrasonic application is beneficial when the application has limited accessibility, such as when inspecting a concrete wall.

The laser array experiment employs only two LDVs in this research. The major advantage of the developed application is that the placement of transmitter and receiver during scanning is flexible. After a linear scanning, the S-scan can be generated using multiple A-scan results. The developed algorithm will automatically calculate the angle between transmitter and receiver based on the thickness of specimen and the arrival time difference of two received signals. The laser array receiver could be the beginning of a laser-based ultrasonic phased array system.

CHAPTER VIII

CONCLUSIONS

The significance of this research is to reduce the risk of railway axle failures by using non-destructive crack detection techniques. Because fatigue loading is inevitable, axles must be inspected and replaced to reduce railway vehicle failures. Train failures do not occur often, but when they occur, the losses are enormous. Current inspection technologies are inefficient and costly. The way to reduce the cost of inspection is to use an automated detection system with minimal human involvement. This significantly reduces the labor cost of an inspection. Disassembling a train bogie also makes inspection expensive; inspection time can be saved by not disassembling train axles. An automated inspection system that would not require the disassembly of train components will be of great impact to the industry.

This research addresses two main topics: advanced ultrasonic techniques and pattern recognition algorithms. Some projects outside of railway axle research use air-coupled ultrasonic technology with successful results, but they still have many limitations, including the distance between transducers and the surface of the specimen or the penetration depth of a specimen. In addition, the reliability of the inspection system is also important for ultrasonic NDT. An ultrasonic phased array system has a much higher POD and will provide a much more rapid inspection when compared to conventional ultrasonic transducers. It can also overcome the limitations of access due to complex geometries. Pattern recognition is widely used in various fields of studies, such as speech recognition,

fingerprint identification, motion recognition, etc. SVM and the developed algorithm successfully distinguished between a cracked axle and an intact axle. Signal processing with a threshold classifier was developed in this research to provide a higher POD with minimum human involvement. The threshold classifier does not require a baseline and the computation time is fast. SVM classifies two classes well, but it takes longer computation time that threshold classifier. The algorithm will contribute to the field of inspection techniques and pattern recognition.

Two main railway axle journal inspection concepts have been developed in this research project: 1) automated detection system of a cracked axle journal using the ultrasonic phased array technique and 2) detection of a cracked axle journal using a chain scanner. The automated detection system is developed for the application of moving trains. However, surface preparation and the placement of robotic equipment underneath a train could cause issues. The second concept provides easy and fast inspection because the probe placement is very flexible. It will only take less than 2 minutes to inspect one axle, and the equipment is portable. No disassembly is required for either inspection concept, thus saving time and reducing cost.

Crack detection using surface waves proves that they can propagate along the complex geometry of the railway axle journal. Axle journal inspection using a surface wave without the disassembly of parts requires one-side inspection. It is recommended that pulse-echo mode or pitch-catch mode 3 be utilized for one-side axle journal inspection. The damage-index signal processing technique automates the detection

process. The inspection technique can be improved by replacing contact transducers with non-contact transducers for surface wave inspection.

Three different air-coupled experiments are demonstrated: 1) the line-source air-coupled ultrasonic array sensors in through-transmission mode, 2) the point-source air-coupled ultrasonic generation using Rayleigh waves, and 3) the laser array detector on a steel plate.

A complete air-coupled ultrasonic system is achieved with the air-coupled 20-array ultrasonic source and microphone sensor as receiver. The best results can be obtained with an excitation frequency range of 50 to 100 kHz. The higher frequencies cannot be achieved because of attenuation by air. The generated ultrasonic waves successfully penetrated the aluminum sheet, the LDPE plate, and the concrete mortar using the through-transmission technique. LDV is also used as a receiver to make a non-contact system. LDV obtained less signal amplification than the microphone sensor with the same gain setting. It is difficult to generate surface waves or S-waves using air-coupled 20-array ultrasonic source because of the placement of the sensors. Because the ultrasonic wave is focused on a focal line, it is difficult to tilt the array, as this generates noise signal. Consequently, the array application is difficult to apply for the crack detection of a railway axle.

A better air-coupled ultrasonic source is introduced by using only one air-coupled ultrasonic sensor for a concrete inspection. One of the methods employed to determine a material property of concrete is the ultrasonic testing approach. The system can be a handy tool in obtaining the material properties, such as modulus of elasticity, as it does not require a coupling medium.

The one-side non-contact crack detection is demonstrated using a Rayleigh wave. The microphone sensor cannot detect the Rayleigh wave signal, but the LDV can. It successfully distinguishes between cracked and uncracked regions using the time-of-flight technique. The one-side non-contact ultrasonic application is beneficial when the application has limited accessibility, such as when inspecting a concrete wall.

The laser array experiment employs only two LDVs in this research. The major advantage of the developed application is that the placement of transmitter and receiver during scanning is flexible. After linear scanning, the S-scan can be generated using multiple A-scan results. The developed algorithm will automatically calculate the angle between transmitter and receiver based on the thickness of specimen and the arrival time difference of two received signals.

A non-contact ultrasound does not require a coupling medium between the transducers and the specimen. It has been studied for a couple of decades, but its application is still a challenge because of a high impedance mismatch between air and the specimen. A complete air-coupled ultrasonic system is developed for various materials in this research. The complete air-coupled ultrasonic system will significantly contribute to the field of air-coupled ultrasonic testing.

REFERENCES

Association of American Railroads. (1984). *Manual of Standards and Recommended Practices – Section A, Part III.* Washington, DC: The Association of American Railroads.

Australian Rail Track Corporation Ltd. (2005). *Common Interface Requirements WOS 01.200.* Adelaide, SA: Australian Rail Track Corporation Ltd.

Baik, J., & Hurlebaus, S. (2013). *Structural health monitoring on cracked railway axle journals using ultrasonic phased array technique*. Paper presented at the Proceeding of Structural Health Monitoring, Stanford, CA

Balanis, C. A. (2005). *Antenna Theory – Analysis and Design (3rd ed.).* Hoboken, NJ: John Wiley & Sons, Inc.

Bass, H. E., Sutherland, L. C., & Zuckerwar, A. J. (1990). Atmospheric absorption of sound: Update. *Journal of Acoustical Society of America,* 88(4), 2019-2021. http://dx.doi.org/10.1121/1.400176

Bass, H. E., Sutherland, L. C., Zuckerwar, A. J., Blaxkstock, D. T., & Hester, D. M. (1995). Atmospheric absorption of sound: Further developments. *Journal of Acoustical Society of America,* 97(1), 680-683. http://dx.doi.org/10.1121/1.412989

Blomme, E., Bulcaen, D., & Declercq, F. (2002). Recent observations with air-coupled NDE in the frequency range of 650 kHz to 1.2 MHz. *Ultrasonics*, 40(1-8), 153-157. doi:10.1016/S0041-624X(02)00129-4

Blum, F. (2003). *A focused, two dimensional, air-coupled ultrasonic array for non-contact generation* (Master's thesis). University of Stuttgart, Stuttgart, Germany.

Blum, F., Jarzynski, J., & Jacobs, L. (2005). A focused two-dimensional air-coupled ultrasonic array for non-contact generation. *NDT&E International*, 38(8), 634-642. doi:10.1016/j.ndteint.2005.03.002

Cau, F., Fanni, A., Montisci, A., Testoni, P., & Usai, M. (2006). A signal-processing tool for non-destructive testing of inaccessible pipes. *Engineering Applications of Artificial Intelligence*, 19(7), 753-760. doi:10.1016/j.engappai.2006.05.005

Chakrapani, S. K., Dayal, V., Barnard, D. J., Eldal, A., & Krafka, R. (2012). Ultrasonic Rayleigh wave inspection of waviness in wind turbine blades: Experimental and finite element method. *American Institute of Physics Conference Proceedings*, 1430, 1911-1917. http://dx.doi.org/10.1063/1.4716444

Ciorau, P. (2004). *Contribution to detection and sizing linear defects by conventional and phased array ultrasonic techniques.* Paper presented at the 16th World Conference on Non-Destructive Testing, Montreal, Canada. Retrieved from http://www.ndt.net/article/wcndt2004/pdf/power_generation/233_ciorau.pdf

Coccia, S., Bartoli, I., Salamone, S., Phillips, R., Scalea, F., Fateh, M., & Carr, G. (2010). Noncontact ultrasonic guided wave detection of rail defects. *Transportation Research Circular E-C145: Light Rail-Growth and Renewal*, 1, 285-296. doi:10.3141/2117-10

Delrue, S., Abeele, K. V. D., Blomme, E., Deveugele, J., & Lust, P. (2010). Two-dimensional simulation of the single-sided air-coupled ultrasonic pitch-catch technique for non-destructive testing. *Ultrasonics*, 50(2), 188-196. doi:10.1016/j.ultras.2009.08.005.

Dhital, D., & Lee, J. R. (2012). A fully non-contact ultrasonic propagation imaging system for closed surface crack evaluation. *Experimental Mechanics*, 52(8), 1111-1122. doi:10.1007/s11340-011-9567-z

Djayaputra, F. (2010). *Determination of longitudinal stress in rails* (Master's thesis). Texas A&M University, College Station, TX.

Ealo, J. L., Camacho, J. J., & Fritsch, C. (2009). Airborne ultrasonic phased arrays using ferroelectrets: A new fabrication approach. *IEEE Transactions on Ultrasonics, Ferroelectrics, and Frequency Control*, 56(4), 848-858. doi:10.1109/TUFFC.2009.1108.

Federal Railroad Administration. (2012). Federal Railroad Administration Office of Safety Analysis. Retrieved from http://safetydata.fra.dot.gov/OfficeofSafety/default.aspx

Frederick, C., Porter, A., & Zimmerman, D. (2010). High-density polyethylene piping bitt-fusion joint examination using ultrasonic phased array. *Journal of Pressure Vessel Technology*, 132(5), 051501. doi:10.1115/1.4001212

Gaal, M., Doring, J., Brekow, G., & Kreutzbruck, M. (2009). *Detection of flaws with Lamb waves and air-coupled ultrasound*. Paper presented at the NDT in Progress, Prague, Czech Republic. Retrieved from http://www.ndt.net/article/Prague2009/ndtip/proceedings/Gaa_6.pdf

Garcia-Ares, E., Garcia-Alonso, J., Fernandez-Plaza, J., Buitrago-Carrillo, A., Crespo-Garcia, G., & Smith, B. (2006). *Equipment health monitoring – Automated cracked wheel and cracked axle detection*. Paper presented at the 11th Annual AAR Research Review, Pueblo, CO.

Ginzel, E., & Thompson, R. (2011). Errors resulting from curved phased array wedges. *NDT.net*. Retrieved from http://www.ndt.net/article/ndtnet/2011/22_Ginzel.pdf

Graff, K. F. (1991). *Wave Motion in Elastic Solids.* New York, NY: Dover Publications, Inc.

Green, R. (2004). Non-contact ultrasonic techniques. *Ultrasonics*, 42(1-9), 9-16. doi:10.1016/j.ultras.2004.01.101

Hansen, R. C. (1998). *Phased Array Antennas.* New York, NY: John Wiley & Sons, Inc.

Hansen, W., & Hintze, H. (2005). Ultrasonic testing of railway axles with the phased array technique – experiencing during operation. *Insight,* 47(6), 358-360. Retrieved from http://www.ndt.net/article/wcndt2004/pdf/railroad_inspection/266_hansen.pdf

Hilbers, U., Neuenschwander, J., Hasener, J., Sanabria, S., Niemz, P., & Thoemen, H. (2012). Observation of interference effects in air-coupled ultrasonic inspection of wood-based panels. *Wood Science Technology*, 46(5), 979-990. doi: 10.1007/s00226-011-0460-9

Hurlebaus, S. (2002). Laser ultrasonics for structural health monitoring. *Contribution to the 7th Laser-Vibrometer Seminar,* Polytec, Waldbronn, Germany, 1, 1-27.

Hurlebaus, S. (2005). *Smart Structures*. College Station, TX: Zachry Department of Civil Engineering, Texas A&M University.

Hurlebaus, S., & Jacobs, L.J. (2006). Dual-probe laser interferometer for structural health monitoring. *Journal of Acoustical Society of America*, 119(4), 1923-1925. http://dx.doi.org/10.1121/1.2170442

Jacques, F., Moreau, F., & Ginzel, E. (2003). Ultrasonic backscatter sizing using phased array developments in tip diffraction flaw sizing. *Insight*, 45(11), 724-728. http://dx.doi.org/10.1784/insi.45.11.724.52966

Jakevicius, L., & Demcenko, A. (2008). Ultrasonic attenuation dependence on air temperature in closed chambers. *Ultragarsas Journal,* 63(1), 18-22. Retrieved from http://www.ndt.net/article/ultragarsas/63-2008-no.1_03-jakevicius.pdf

Kazys, R., Demcenko, A., Zukauskas, E., & Mazeika, L. (2006). Air-coupled ultrasonic investigation of multi-layered composite materials. *Ultrasonics*, 44, 819-822. doi:10.1016/j.ultras.2006.05.112

Kundu, T. (2004). *Ultrasonic Nondestructive Evaluation: Engineering and Biological Material Characterization*. Boca Raton, FL: CRC Press.

Lanza di Scalea, F., Rizzo, P., Coccia, S., Bartoli, I., Fateh, M., Viola, E., & Pascale, G. (2005). Non-contact ultrasonic inspection of rails and signal processing for automatic defect detection and classification. *Insight*, 47(6), 346-353. http://dx.doi.org/10.1784/insi.47.6.346.66449

Liaptsis, D., Cooper, I., Boyle, K., & Nicholson, P. I. (2011). The application of phased array ultrasonic techniques for inspection of railway axles from their end face. *American Institute of Physics Conference Proceedings,* 1335, 1440-1447. http://dx.doi.org/10.1063/1.3592101

Marty, P. N. (2012). *Latest development in the UT inspection of train wheels and axles*. Paper presented at the 18th World Conference on Non-Destructive Testing, Durban, South Africa. Retrieved from http://www.ndt.net/article/wcndt2012/papers/572_wcndtfinal00571.pdf

Moles, M., Dube, N., Labbe, S., & Ginzel, E. (2005). Review of ultrasonic phased arrays for pressure vessel and pipeline weld inspections. *Journal of Pressure Vessel Technology*, 127(3), 351-356. doi:10.1115/1.1991881

Montero de Espinosa, F., Chavez, J. A., Yanez, Y., Salazar, J., Turo, A., Chinchurreta, F. J., & Garcia-Hernandez, M. (2004). *Air-coupled piezoelectric array transducers for NDT applications*. Paper presented at the 16th World Conference on Non-Destructive Testing, Montreal, Canada.

Morgan, R., Gonzales, K., Smith, E., & Smith, B. (2006). *Remotely detecting cracks in moving freight railcar axles*. Pueblo, CO: Transportation Technology Center, Inc. Retrieved from onlinepubs.trb.org/onlinepubs/archive/studies/idea/finalreports/safety/S-08_Final_Report.pdf

Nishino, H., Asano, T., Taniquchi, Y., Yoshida, K., & Ogawa, H. (2011). Precise measurement of pipe wall thickness in noncontact manner using a circumferential Lamb wave generated and detected by a pair of air-coupled transducers. *Japanese Journal of Applied Physics*, 50(7S), 1-7. doi:10.1143/JJAP.50.07HC10

Penny, C. (1976). *U.S. Patent No. 3,978,713.* Washington, DC: U.S. Patent and Trademark Office.

Solodov, I., Doring, D., & Busse, G. (2009). *Air-coupled Lamb and Rayleigh waves for remote NDE of defects and material elastic properties*. Paper presented at the 10th International Conference of the Slovenian Society for Non-Destructive Testing, Ljubljana, Slovenia. Retrieved from http://www.ndt.net/article/ndt-slovenia2009/PDF/P04.pdf

Stoessel, R. (2004). *Air-coupled ultrasound inspection as a new non-destructive testing tool for quality assurance* (Doctoral dissertation). University of Stuttgart, Stuttgart, Germany.

Stoessel, R., Krohn, N., Pfleiderer, K., & Busse, G. (2002). Air-coupled ultrasonic inspection of various materials. *Ultrasonics*, 40(1-8), 159-163.

Sukmana, D. D., & Ihara, I. (2005). Application of air-coupled ultrasound to noncontact surface roughness evaluation. *Journal of Physics: Conference Series*, 520(1), 1-4. doi:10.1088/1742-6596/520/1/012016

Terzic, J., Nagarajah, C.R., & Alamgir, M. (2010). Fluid level measurement in dynamic environments using a single ultrasonic sensor and Support Vector Machine (SVM). *Sensors and Actuators A: Physical*, 161(1-2), 278-287. doi:10.1016/j.sna.2010.05.005

Uchanin, V., Lutcenko, G., Dshaganjan, A., & Opanasenko, A. (2010). *The application of eddy current section in automated system for combined railway rolling stock axles inspection*. Paper presented at the 10th European Conference on Non-Destructive Testing, Moscow, Russia. Retrieved from http://www.ndt.net/article/ecndt2010/reports/1_02_19.pdf

Vapnik, V.N. (1995). *The Nature of Statistical Learning Theory (2nd ed.).* New York, NY: Springer-Verlag New York, Inc.

Williams, H. P. (1966). *Antenna Theory and Design (2nd ed.),* Kingsway, London, UK: Sir Isaac Pitman & Sons Ltd.

Wolff, M., & Tschope, C. (2009). Pattern recognition for sensor signals. *IEEE SENSORS 2009 Conference*, 2, 665-668. doi:10.1109/ICSENS.2009.5398338

Wooh, S., & Shi, Y. (1998). Influence of phased array element size on beam steering behavior. *Ultrasonics,* 36(6), 737-749. doi:10.1016/S0041-624X(97)00164-9

Zerbst, U., Madler, K., & Hintze, H. (2005). Fracture mechanics in railway application-an overview. *Engineering Fracture Mechanics*, 72(2), 163-194. doi:10.1016/j.engfracmech.2003.11.010

Zerbst, U., Vormwald, M., Andersch, C., Madler, K., & Pfuff, M. (2005). The development of a damage tolerance concept for railway components and its demonstration for a railway axle. *Engineering Fracture Mechanics*, 72(2), 209-239. doi:10.1016/j.engfracmech.2003.11.011

Zhu, J., & Popovics, S. (2005). Non-contact imaging for surface-opening cracks in concrete with air-coupled sensors. *Materials and Structures*, 38(9), 801-806. doi:10.1007/BF02481652

APPENDIX A

FRAME DESIGN AND CRACK CONFIGURATION

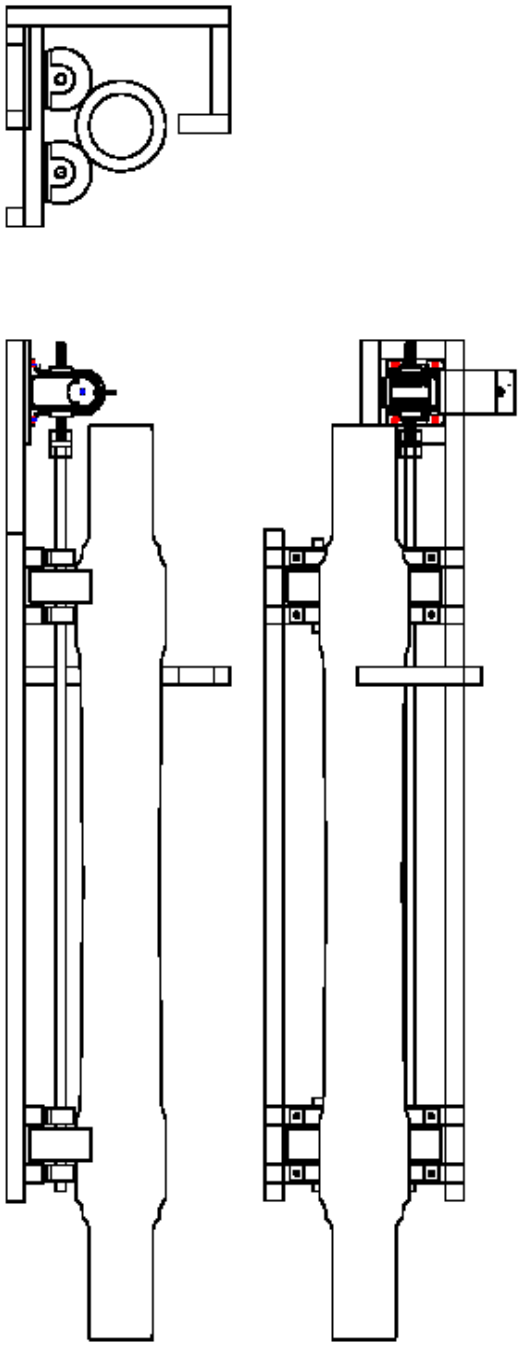

Figure A.1. Fixture drawing

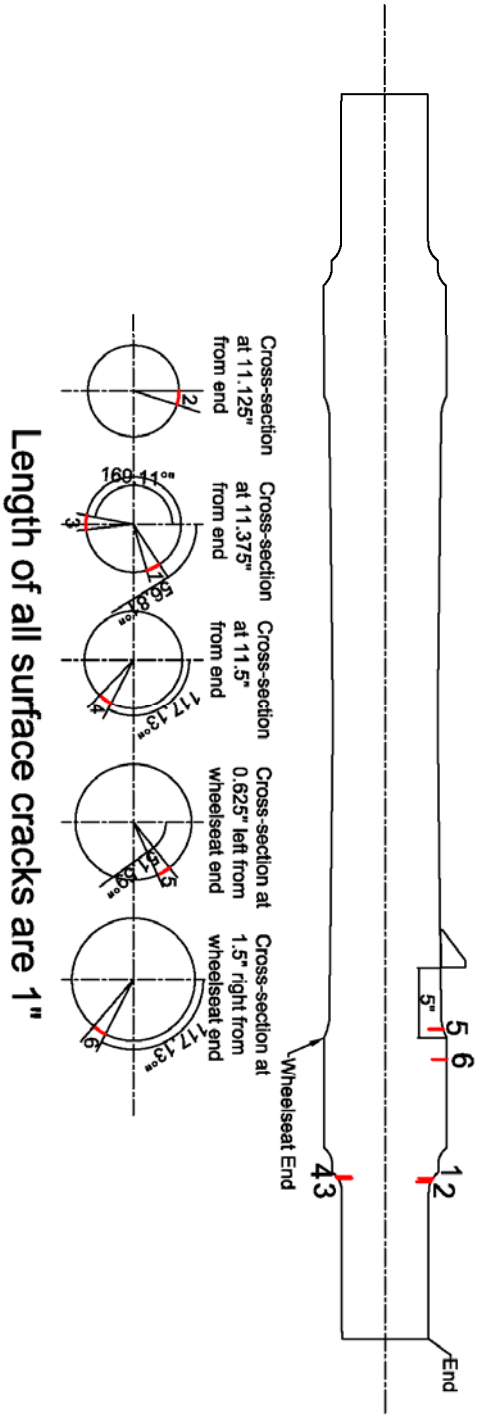

Figure A.2. Crack configuration on the axle specimen

APPENDIX B

EXPERIMENTAL PROCEDURE

Automated Detection System

- Place axle on automated detection frame.
- Adjust location of probe holder; fix holder at 5 in. from wheelseat region.
- Place probe to probe holder and connect hose to wedge.
- Turn on ultrasonic phased array system and enable C-scan mode with beam angle from 30 to 70°.
- Turn on water pump and transmission motor. Make sure that wedge and specimen are fully contacted with water.
- Adjust transmission motor speed using controller necessary. If axle moves in horizontal direction, motor needs to be stopped. Adjust alignment of roller so as not to move axle in horizontal direction.

Chain Scanner

- Buckle chain scanner on axle specimen.
- Place wedge and transducer to wedge holder of scanner.
- Connect hose to wedge.
- Adjust location of wedge and place it 5 in. from wheelseat region.
- Turn on ultrasonic phased array system and enable C-scan mode with beam angle from 30 to 70°.
- Enable scanner mode and adjust scan rate if necessary.
- Turn on water pump and make sure that wedge and specimen are fully contacted with water.
- Rotate chain scanner and monitor results screen of ultrasonic phased array system.
- Move chain scanner back and forth if there are any broken signals.

Crack Detection Using Surface Wave

- Adjust wedge angle to generate surface wave based on Snell's law (incident angle of 65° for the axle).
- Place transducers at desired locations (pulse-echo and pitch-catch modes), as shown in Figures 6.1, 6.3, 6.5, and 6.7.
- Apply coupling medium on wedge and axle.
- Adjust energy, damping, and pulse repetition frequency setting on pulser-receiver as necessary.

Air-coupled Ultrasonic Generation

- Acquire function generator, power amplifier, and DC power supply to generate air-coupled ultrasonic.
- Connect them to transmitting circuit, which is shown in Figure 7.3.
- Turn on function generator first and set to desired frequency, voltage, and burst.
- Turn on DC power supply and set it to 150 V.
- Turn on power amplifier and monitor front panel display of power amplifier. Forward power, Pf, and reverse power, Pr, have to be 0 W with a status indicator of 'OK.' If Pf or Pr is other than 0 W, power amplifier must be turned off. If it is not zero, there must be a short circuit and it will burn power supply.

* Trouble shooting

When the current overflows into the power amplifier, there are two possibilities: The first problem could be a bad connection to the power source or ground, as shown in Figure B.1. The second possible problem is the burned circuit. After using the air-coupled ultrasonic sensor for a long time period, the overflow of current on a power amplifier is frequently observed. In this case, the transmitting circuit needs to be replaced.

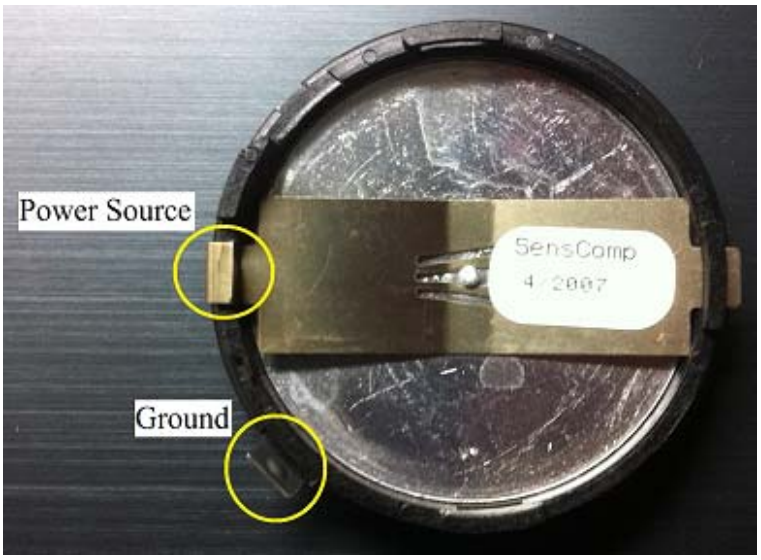

Figure B.1. Air-coupled ultrasonic transducer